Toward Understanding Astrophysical Phenomena

Thesis by
Jing Luan

In Partial Fulfillment of the Requirements
for the Degree of
Doctor of Philosophy

California Institute of Technology
Pasadena, California

(Defended May 22, 2015)

Acknowledgments

I am very grateful to my dear adviser, Peter Goldreich. Before working with him, my second through fourth years at graduate school were almost totally wasted by a project on common envelope. I was so desperate that my science dream may have to come to an end and regretted the three-year youth spent on a project leading to nowhere. Finally I decided to ask Peter for help. He had officially retired years ago, and in principle he did not need to bother at all. However, thanks to his strong feeling of responsibility for young scientists and his warm-hearted nature, I was accepted as his grad student at the entry of my fifth year. It was a pretty late beginning and neither of us had a clue what was ahead of us in the future, like whether I could graduate successfully and whether I could find a postdoc position after graduation. In spite of all these uncertainties and fears about the future, a new door opened to me, through which I see all kinds of different astronomical phenomenon and get to know how physical thinking leads to simple but sensible understanding of them. My way of research underwent a revolution, thanks to Peter's patient educations and great inspirations.

Peter not only guided me in science, but also guided me in life style. He kept urging me to do physical exercises. Now I have established a good habit of exercising almost every day, which benefits myself both physically and mentally. Another great thing I learned from Peter is 'giving is better than receiving'. I still remember how impressed I was by Peter's warm heart when he offered his gym pass ticket to a visitor at Caltech. Although this is only a small thing and everybody can afford such a ticket, not everyone acts like Peter who is always ready to reach out a helping hand. So does his wife, Susan Goldreich. I guess sharing a warm heart is one of the bonds that tie this couple together, and I wish them be happy and healthy forever!

Peter once said that working with students kept him active in science. I cannot agree more. No matter how smart one is, he/she needs other people's inspirations, which act like sparks that trigger the fire of creative ideas. Students, some of whom will be the next generation of scientists, ask stupid questions sometimes. It is wrong to omit the value of those stupid questions because they may supply another aspect of looking at the same problem, which may help to break the old way of thinking. My goal was once only to become a successful scientist and to do creative and valuable work that could last. But now, with the influences of Peter, I also want to become a good adviser to my future students, if I could become a faculty somewhere. I hope I could also become a resource of knowledge that could benefit other people. Moreover, I hope I could become a person who is always ready to give than to receive.

Words are not enough to express my thanks to Peter. He is not merely an academic adviser but also, and more importantly, a life adviser. The things I learn from him will benefit me for a life-long time!

I thank Yanbei Chen, who was my academic adviser during my first year. I thank all my committee members, including Peter Goldreich, Yanbei Chen, Tom Prince and Christian Ott, who accompany me to go through my difficult time and keep track of my progress every half year. I also than Frank Porter, who supported me while I switched adviser. I thank my parents and my best friend Simin Sun who are almost always there when I need them.

Chapter 1 is published in the Astrophysical Journal Letters, Volume 785, Issue 2, article id.

L26, 4 pp. I am the first author and my coauthor is Peter Goldreich. I thank Sarah Burke-Spolaor, Christian D. Ott and Yanbei Chen for valuable suggestions and comments. I am grateful to an anonymous referee whose advice alerted us to an error in a previous version of the paper corresponding to this chapter.

Chapter 2 is published in the Astrophysical Journal, Volume 790, Issue 1, article id. 82, 6 pp. (2014). I am the first author and my coauthor is Peter Goldreich. I thank Scott Ransom and Anne Archibald for educating us about how the masses and orbits of the pulsar triple system were derived. I appreciate that Scott Ransom pointed out that we used a wrong number for this system immediately after we posted the paper on arxiv. I am grateful to John Chambers both for making his code Mercury publicly available and for responding to our queries on how to use it. Thanks are also due to Christian Ott and Sterl Phinney for guidance regarding the possibility that the pulsar in J0337+1715 formed by accretion induced collapse of a WD. I also like to thank Anthony L. Prio for reminding us that the Q values in Piro (2011) are actually upper limits.

Chapter 3 and 4 will be submitted to journals soon. I am the first author, and my coauthor is Peter Goldreich.

Chapter 5 is published in Physical Review D, vol. 85, Issue 10, id. 102002. I am the first author, and my coauthors are Shaun Hooper, Linqing Wen and Yanbei Chen. I am grateful for inspiring discussions with Rana Adhikari, Kipp Cannon, Chad Hanna, Drew Keppel, Alan Weinstein, Patrick Brady, Shin Kee Chung, David Blair, Benoit Mours, Leo Singer, Peter Shawhan, and Nickolas Fotopoulos. This chapter has been supported in part by NSF Grants PHY-0601459, PHY-0653653, (LIGO) and CAREER Grant PHY-0956189 and the David and Barbara Groce start-up fund at Caltech, and by ARC Discovery Project and ARC Future Fellowship program.

Abstract

Fast radio bursts (FRBs), a novel type of radio pulse, whose physics is not yet understood at all. Only a handful of FRBs had been detected when we started this project. Taking account of the scant observations, we put physical constraints on FRBs. We excluded proposals of a galactic origin for their extraordinarily high dispersion measures (DM), in particular stellar coronas and HII regions. Therefore our work supports an extragalactic origin for FRBs. We show that the resolved scattering tail of FRB 110220 is unlikely to be due to propagation through the intergalactic plasma. Instead the scattering is probably caused by the interstellar medium in the FRB's host galaxy, and indicates that this burst sits in the central region of that galaxy. Pulse durations of order ms constrain source sizes of FRBs implying enormous brightness temperatures and thus coherent emission. Electric fields near FRBs at cosmological distances would be so strong that they could accelerate free electrons from rest to relativistic energies in a single wave period. When we worked on FRBs, it was unclear whether they were genuine astronomical signals as distinct from 'perytons', clearly terrestrial radio bursts, sharing some common properties with FRBs. Recently, in April 2015, astronomers discovered that perytons were emitted by microwave ovens. Radio chirps similar to FRBs were emitted when their doors opened while they were still heating. Evidence for the astronomical nature of FRBs has strengthened since our paper was published. Some bursts have been found to show linear and circular polarizations and Faraday rotation of the linear polarization has also been detected. I hope to resume working on FRBs in the near future. But after we completed our FRB paper, I decided to pause this project because of the lack of observational constraints.

The pulsar triple system, J0733+1715, has its orbital parameters fitted to high accuracy owing to the precise timing of the central ms pulsar. The two orbits are highly hierarchical, namely $P_{\rm orb,1} \ll P_{\rm orb,2}$, where 1 and 2 label the inner and outer white dwarf (WD) companions respectively. Moreover, their orbital planes almost coincide, providing a unique opportunity to study secular interaction associated purely with eccentricity beyond the solar system. Secular interaction only involves effect averaged over many orbits. Thus each companion can be represented by an elliptical wire with its mass distributed inversely proportional to its local orbital speed. Generally there exists a mutual torque, which vanishes only when their apsidal lines are parallel or anti-parallel. To maintain either mode, the eccentricity ratio, e_1/e_2, must be of the proper value, so that both apsidal lines precess together. For J0733+1715, $e_1 \ll e_2$ for the parallel mode, while $e_1 \gg e_2$ for the anti-parallel one. We show that the former precesses ~ 10 times slower than the latter. Currently the system is dominated by the parallel mode. Although only a little anti-parallel mode survives, both eccentricities especially e_1 oscillate on $\sim 10^3$y timescale. Detectable changes would occur within ~ 1y. We demonstrate that the anti-parallel mode gets damped $\sim 10^4$ times faster than its parallel brother by any dissipative process diminishing e_1. If it is the tidal damping in the inner WD, we proceed to estimate its tidal quantity parameter (Q) to be $\sim 10^6$, which was poorly constrained by observations. However, tidal damping may also happen during the preceding low-mass X-ray binary (LMXB) phase or hydrogen thermal nuclear flashes. But, in both cases, the inner companion fills its Roche lobe and probably suffers mass/angular momentum loss, which might cause e_1 to grow rather than decay.

Several pairs of solar system satellites occupy mean motion resonances (MMRs). We divide these into two groups according to their proximity to exact resonance. Proximity is measured by the existence of a separatrix in phase space. MMRs between Io-Europa, Europa-Ganymede and Enceladus-Dione are too distant from exact resonance for a separatrix to appear. A separatrix is present only in the phase spaces of the Mimas-Tethys and Titan-Hyperion MMRs and their resonant arguments are the only ones to exhibit substantial librations. When a separatrix is present, tidal damping of eccentricity or inclination excites overstable librations that can lead to passage through resonance on the damping timescale. However, after investigation, we conclude that the librations in the Mimas-Tethys and Titan-Hyperion MMRs are fossils and do not result from overstability.

Rubble piles are common in the solar system. Monolithic elements touch their neighbors in small localized areas. Voids occupy a significant fraction of the volume. In a fluid-free environment, heat cannot conduct through voids; only radiation can transfer energy across them. We model the effective thermal conductivity of a rubble pile and show that it is proportional the square root of the pressure, P, for $P \leq \epsilon_Y^3 \mu$ where ϵ_Y is the material's yield strain and μ its shear modulus. Our model provides an excellent fit to the depth dependence of the thermal conductivity in the top 140 cm of the lunar regolith. It also offers an explanation for the low thermal inertias of rocky asteroids and icy satellites. Lastly, we discuss how rubble piles slow down the cooling of small bodies such as asteroids.

Electromagnetic (EM) follow-up observations of gravitational wave (GW) events will help shed light on the nature of the sources, and more can be learned if the EM follow-ups can start as soon as the GW event becomes observable. In this paper, we propose a computationally efficient time-domain algorithm capable of detecting gravitational waves (GWs) from coalescing binaries of compact objects with nearly zero time delay. In case when the signal is strong enough, our algorithm also has the flexibility to trigger EM observation *before* the merger. The key to the efficiency of our algorithm arises from the use of chains of so-called Infinite Impulse Response (IIR) filters, which filter time-series data recursively. Computational cost is further reduced by a template interpolation technique that requires filtering to be done only for a much coarser template bank than otherwise required to sufficiently recover optimal signal-to-noise ratio. Towards future detectors with sensitivity extending to lower frequencies, our algorithm's computational cost is shown to increase rather insignificantly compared to the conventional time-domain correlation method. Moreover, at latencies of less than hundreds to thousands of seconds, this method is expected to be computationally more efficient than the straightforward frequency-domain method.

Contents

List of Figures

List of Tables

Chapter 1

Physical Constraints on Fast Radio Bursts

1.1 Introduction

FRBs are single, broad-band pulses with flux densities $S_\nu \sim$ Jy and durations $\Delta t \sim$ ms detected at $\nu \sim$ GHz (Lorimer et al., 2007; Thornton et al., 2013). They were discovered by de-dispersing data collected by the Parkes multi-beam radio telescope during pulsar searches. Thus far there are no reports of FRBs detected by other radio telescopes. The procedure followed in the detection of FRBs is similar to that which led to the discovery of rotating radio transients (RRATs, McLaughlin et al. (2006)) now firmly identified as sporadically active pulsars. Thornton et al. (2013) report the detection of four high-galactic-latitude ($> 40^\circ$) FRBs with DM of several hundred $\mathrm{pc\,cm^{-3}}$, well above the contribution expected from our Galaxy (Cordes & Lazio, 2002). It has become popular to attribute these large DMs to propagation through the intergalactic plasma indicating source distances $d \sim$ Gpc.

Currently, it is unclear whether FRBs herald the discovery of a new type of astronomical source or merely that of an unidentified source of noise. The strongest argument supporting the astronomical origin of FRBs is the precise degree to which arrival times of individual pulses follow the ν^{-2} law that characterizes the propagation of radio waves through a cold plasma. Some pulses detected in searches for FRBs are clearly terrestrial although their origin is unknown. These have been named Perytons. It is notable that the classification of the Lorimer burst (Lorimer et al., 2007) remains controversial, although if it is a FRB it would be the first and brightest of those detected. For the remainder of this paper, we cast aside our doubts and proceed as through FRBs are *bona-fide* astronomical signals. Interest in detecting additional FRBs with other radio telescopes is high (Lorimer et al., 2013; Trott et al., 2013)), so we expect their true nature to be revealed soon. In §1.2, we show that the DMs of FRBs cannot arise from propagation through a stellar corona or a galactic HII region. Then in §1.3, we argue that intergalactic electron density fluctuations are unlikely to provide the angular deflections deduced from the temporal scattering tail resolved in FRB 110220. §1.4 shows that the contribution of FRBs to the brightness of the radio sky is negligible. In §1.5, we discuss the high brightness temperatures of FRBs and assess the possibility that FRBs are signals beamed at Earth by advanced civilizations. §1.6 discusses the strength of the electric fields of FRBs in terms of their ability to accelerate free electrons to relativistic energies in one radio wave period. We summarize our results in §1.7 and briefly comment on possible emission mechanisms for FRBs.

1.2 Sources are Probably Extra-Galactic

In this section, we discuss two galactic candidates to produce DM for FRBs. One is a stellar corona, suggested by Loeb et al. (2014); the other is an HII region. We then demonstrate that neither can account for the large DM of FRBs. Thus, the sources of FRBs are probably extra-galactic.

1.2.1 Free-free absorption in stellar coronas

Loeb et al. (2014) proposed that FRBs originate from flares on main-sequence stars and that the DM arises from propagation through the stellar corona. This proposal has the attractive feature of greatly reducing the source luminosity with respect to that required for an unspecified extragalactic source. Nevertheless, free-free absorption limits a stellar corona's DM to be well below that of FRB's.

In the Rayleigh-Jeans limit, $h\nu \ll k_B T$, the free-free absorption coefficient including stimulated emission reads (Spitzer, 1978)

$$\alpha = \frac{4}{3}\left(\frac{2\pi}{3}\right)^{1/2} \frac{Z^2 e^6 n_e n_i \bar{g}_{\rm ff}}{c\, m_e^{3/2} \left(k_B T\right)^{3/2} \nu^2}\,, \tag{1.1}$$

$$\bar{g}_{\rm ff} = \frac{\sqrt{3}}{\pi}\left[\ln\left(\frac{(2k_B T)^{3/2}}{\pi e^2 m_e^{1/2}\nu}\right) - \frac{5\gamma}{2}\right]\,, \tag{1.2}$$

where $\bar{g}_{\rm ff}$ is the Gaunt factor and $\gamma = 0.577$ is Euler's constant. Other symbols are standard: m_e is the electron mass, e is the electron charge, and n_e and n_i are the number densities of electrons and ions. For cosmic abundances and in the temperature range of interest here, it suffices to evaluate α for a pure hydrogen plasma, i.e., $Z = 1$ and $n_e = n_i$.

For a homogenous medium, the optical depth for free-free absorption is $\tau \sim \alpha s \propto n_e^2 s$, where s is the path length along the line of sight through the medium. Since $\mathrm{DM} = n_e s$, we express n_e in terms of s and τ. Then $\tau \lesssim 1$ sets an upper limit on DM,

$$\mathrm{DM} \sim \frac{3^{3/4}(m_e k_B T)^{3/4}(cs)^{1/2}\nu}{2^{5/4}\pi^{1/4}e^3\bar{g}_{\rm ff}^{1/2}}\,. \tag{1.3}$$

For $k_B T \lesssim GMm_p/R$ the base of the corona would be in quasi-hydrostatic equilibrium. Since density drops rapidly with height in an isothermal atmosphere, we replace s in Eq. (1.3) by the scale height $2k_B T/(m_p g)$, and $k_B T$ by GMm_p/R to obtain

$$\mathrm{DM} \sim \frac{3^{3/4}c^{1/2}m_e^{3/4}(GMm_p)^{3/4}\nu}{2^{3/4}\pi^{1/4}e^3 R^{1/4}\bar{g}_{\rm ff}^{1/2}} \tag{1.4}$$

$$\sim 50\left(\frac{M}{M_\odot}\right)^{3/4}\left(\frac{R}{R_\odot}\right)^{-1/4} \mathrm{pc\,cm^{-3}} \tag{1.5}$$

which is much smaller than the DMs of FRBs.

A hotter corona could provide a larger DM. If free to expand, it would essentially be a stellar wind even close to the photosphere. For simplicity, the wind is taken to have constant velocity and constant temperature. These approximations are not entirely consistent because a supersonic isothermal wind would slowly accelerate as its density declined. This inconsistency leads us to overestimate dispersion measure relative to free-free absorption because the former and latter are proportional to density and density squared. At constant radial velocity, $n_e(r) \sim n_e(R)(R/r)^2$.

$$\mathrm{DM} \sim \int_R^\infty n_e dr \sim n_e(R)R\,. \tag{1.5}$$

From Eq. (1.2), $\alpha = Cn_e^2/(k_B T)^{3/2}$,

$$\tau \sim \int_R^\infty \alpha dr \sim \int_R^\infty \frac{Cn_e^2}{(k_B T)^{3/2}}dr \sim \frac{Cn_e(R)^2\, R}{3(k_B T)^{3/2}}\,. \tag{1.5}$$

The power carried by the wind would be[1]

$$P_w \sim 4\pi m_p n_e(R) R^2 v_{\rm th}^3 \sim \frac{2^6 \pi^{3/2} e^6 \bar{g}_{\rm ff} {\rm DM}^3}{3^{5/2} c m_e^{3/2} m_H^{1/2} \nu^2 \tau} \tag{1.6}$$

$$\gtrsim 40 L_\odot \left(\frac{\rm DM}{10^3\,{\rm pc\,cm^{-3}}}\right)^3 \left(\frac{\nu}{1\,{\rm GHz}}\right)^{-2}, \tag{1.7}$$

where we have expressed n_e and s in terms of DM and τ. The $\gtrsim$ on the second line follows from setting $\tau \lesssim 1$. Clearly a coronal wind cannot carry more energy than the luminosity of its star could provide. Thus even the lowest DM measured for the FRB's reported by Thornton et al. (2013), DM$\sim 553\,{\rm pc\,cm^{-3}}$, could not arise from propagation through a coronal wind from the flare stars discussed by Loeb et al. (2014).

A hotter corona might be confined by a strong magnetic field provided the magnetic stress is comparable to the gas pressure. Under this condition, the ratio of the electron cyclotron frequency to the plasma frequency would be

$$\frac{\omega_{ce}}{\omega_p} \approx \left(\frac{k_B T}{m_e c^2}\right)^{1/2} . \tag{1.7}$$

Then the dispersion relation for radio waves would depend on ω/ω_{ce} in addition to ω/ω_p which might cause the frequency dependence of the pulse arrival times to deviate by more than the limits set by observations of FRBs.

Numerical results given above are scaled with respect to parameters pertaining to the sun. Typical flare stars are lower main sequence dwarfs for which $R \propto M^{0.9}$ and $L \propto M^{3.4}$ (Demircan & Kahraman, 1991). Application of these relations only strengthens our conclusion that the DMs of FRBs cannot be attributed to passage of radio waves through coronas.

Before moving on, we offer a few additional comments about radio emission from flare stars. This topic has been discussed for more than half a century, starting with the paper "Radio Emission from Flare Stars" by Lovell (1963). To our knowledge, no bursts sharing the common properties of FRBs have been reported. Moreover, the most frequently studied radio flare stars are close by. For example, AD Leonis and YZ Canis Minoris are at distance of $\sim 5\,{\rm pc}$ and $\sim 6\,{\rm pc}$, respectively. These two stars figure prominently, and in most cases exclusively, in each of the papers on radio flares referenced in Loeb et al. (2014) and their strongest bursts barely reach the level of 1 Jy that is typical of FRBs. Dynamic spectra of radio bursts from AD Leonis observed with wide bandwidth and at high time resolution at Arecibo (Osten & Bastian, 2006, 2008) do not resemble those of FRBs. Pulses suffering dispersion induced time delays should only show negative frequency drifts. But the histogram of these bursts (Figure 4a in Osten & Bastian (2006)) exhibits both positive and negative frequency drifts and is symmetric about zero drift with half width at half maximum of $\sim 3\times10^{-4}\,s/{\rm MHz}$. Note that a DM $\sim 20\,{\rm pc\,cm^{-3}}$ produces a negative frequency drift rate of similar magnitude.

1.2.2 HII region

An HII region is another candidate to account for the DM of a galactic FRB. A lower limit on s is deducible from Eq. (1.3). With $T \sim 10^4\,{\rm K}$, $s \gtrsim 0.2\,{\rm pc}$. The angular size of such an HII region at 500 pc is $d\theta_{\rm HII} \sim 80\,{\rm arcsec}$. At 1.4 GHz, the 64 m, Parkes telescope's beam size is $d\theta \sim \lambda/D \sim 20\,{\rm cm}/64\,{\rm m} \sim 650\,{\rm arcsec}$. Thus the antenna temperature of such an HII region would be $T_A = T_{\rm HII} \times (d\theta_{\rm HII}/d\theta)^2 \sim 150\,{\rm K}$. The sensitivity of Parkes at 1.4 GHz for a 270 s integration time is 0.6 mK for 10σ detection of FRBs (cf. Parkes user guide). Thornton et al. would have recognized an HII region with these properties in the data they search for FRBs.

The bottom line from this section is that neither a stellar corona nor an HII region is a plausible candidate for the high DMs of FRBs'. Thus FRBs are likely to be extragalactic.

---

[1] In calculating the power needed to drive the wind, we neglect the heat that must be supplied in order to overcome the cooling effect of adiabatic expansion.

1.3 Temporal Scattering

We follow conventions developed in the investigation of angular and temporal scattering in the interstellar medium (Rickett, 1990) and adopt the Kolmogorov spectrum, $\delta n_e/n_e \sim (\ell/L)^{1/3}$, for electron density fluctuations on scale ℓ where $\ell_{\rm min} \leq \ell < L$. Moreover, we assume that this spectrum is associated with a turbulent cascade in which sonic velocity fluctuations are present at outer scale L.[2] Finally, the scattering is described by projecting the phase differences that accumulate along the line of sight between source and observer onto a thin screen located midway between them. For a source at distance d, we obtain

$$\Delta\phi \sim \frac{n_e e^2 d^{1/2} \ell^{5/6} \lambda}{\pi m_e c^2 L^{1/3}} \, . \tag{1.7}$$

We are concerned with strong scattering which requires $\Delta\phi > 1$. Then the scattering angle

$$\Delta\theta \sim \frac{\lambda}{\ell} \Delta\phi \propto \ell^{-1/6} \tag{1.7}$$

is dominated by the smallest scale for which $\Delta\phi \gtrsim 1$. For sufficiently small $\ell_{\rm min}$, this is the diffraction scale at which $\Delta\phi \sim 1$;

$$\ell_{\rm dif} \sim \left(\frac{\pi m_e c^2}{e^2 n_e \lambda}\right)^{6/5} \frac{L^{2/5}}{d^{3/5}} \, . \tag{1.7}$$

Otherwise it is $\ell_{\rm min}$. The temporal delay,

$$\Delta t_{sc} \sim \frac{d}{c} (\Delta\theta)^2 \tag{1.7}$$

is expressed as

$$\Delta t_{sc} \sim \begin{cases} \frac{d}{c}\left(\frac{\lambda}{\ell_{\rm dif}}\right)^2 \propto \lambda^{4.4} \, , \quad \ell_{\rm min} \leq \ell_{\rm dif} \, ; \\ \\ \frac{d}{c}\left(\frac{\Delta\phi\lambda}{\ell_{\rm min}}\right)^2 \propto \lambda^4 \, , \quad \ell_{\rm min} > \ell_{\rm dif} \, . \end{cases} \tag{1.7}$$

FRB 110220 exhibits a well-resolved exponential tail with $\Delta t_{sc} \sim 5.6 \pm 0.1\,{\rm ms}$ that has been attributed to plasma scattering (Thornton et al., 2013). Unfortunately, the data is not quite good enough to distinguish between the two cases given in Eq. (1.3) (Thornton et al., 2013). But both restrict the outer scale to be less than

$$\begin{aligned} L_{\rm max} \quad &\sim \quad \left(\frac{e^2 \ n_e}{\pi m_e c^2}\right)^3 \frac{\lambda^{11/2} \ d^{11/4}}{(c\Delta t_{sc})^{5/4}} \sim 10^{13} \left(\frac{d}{\rm Gpc}\right)^{11/4} \\ &\times \left(\frac{n_e}{10^{-7}\ {\rm cm^{-3}}}\right)^3 \left(\frac{\Delta t_{sc}}{\rm ms}\right)^{-5/4} \ {\rm cm} \, . \end{aligned} \tag{1.6}$$

$L_{\rm max}$ is an impossibly small outer scale for extragalactic turbulence.[3] Sonic velocity perturbations dissipate their bulk kinetic energy into heat on the timescale over which sound waves cross the outer scale. This would imply a doubling of the IGM temperature over several months since the cooling rate is comparable to the Hubble time.

Based on the argument given above, it seems unlikely that propagation through the diffuse IGM could make a measurable contribution to the scattering tail of a FRB. Indeed, an outer scale of order 10^{24} cm is required to reduce the turbulent heating rate to a level compatible with the cooling rate. With this value, $\Delta t_{sc} \lesssim 10^{-12}$ s for $d \sim$ Gpc. Previously, Macquart & Koay (2013) expressed doubt that propagation through the diffuse IGM could produce discernible scattering tails for FRBs.

---

[2] Conclusions reached in this section depend on the assumption that the electron density fluctuations arise from a turbulent cascade.

[3] In a clumpy IGM with volume filling factor f, $L_{\rm max}$ would be larger by $f^{-3/2}$.

However, they failed to recognize the incompatibility of a small $L_{\max}$ with regulation of the IGM's temperature.

1.4 Contribution to Radio Sky

Thornton et al. (2013) estimate a FRB event rate of $\sim 10^4\,\mathrm{sky}^{-1}\mathrm{day}^{-1} \sim 0.1\,\mathrm{s}^{-1}$. Given characteristic flux densities of a Jansky and durations of a few milliseconds, FRBs add about $10^{-9}\,\mathrm{K}$ to the radio background at 1.4 GHz.[4] This value is dwarfed by contributions of 2.7 K from the CMB and even by minor additions from the galactic halo, the galactic plane and extragalactic radio sources. According to Subrahmanyan & Cowsik (2013), these account for 0.79 K, 0.3 K and 0.14 K respectively at 1.4 GHz.

1.5 Brightness Temperature

FRBs are not angularly resolved, and thus their brightness temperatures (T_B) are unknown. However, the duration of a pulse, Δt, constrains the linear size of the source and thus its angular size at a fixed distance. Relativistic beaming is a complication. Radiation emitted from a spherical shell expanding with Lorentz factor Γ is beamed into a solid angle $\Delta\Omega \sim \Gamma^{-2}$. Arrival times of photons emitted simultaneously spread by $R/(c\Gamma^2)$ permitting a source size as large

$$R \lesssim c\Delta t\Gamma^2 \,. \tag{1.6}$$

Consequently, the brightness temperature in the observer's frame is

$$\begin{aligned} T_B &\simeq \frac{S_\nu d^2}{k_B\Gamma^2\nu^2\Delta t^2} \qquad (1.7)\\ &\sim \frac{10^{36}\,\mathrm{K}}{\Gamma^2}\left(\frac{S_\nu}{\mathrm{Jy}}\right)\left(\frac{d}{\mathrm{Gpc}}\right)^2\left(\frac{\nu}{\mathrm{GHz}}\right)^{-2}\left(\frac{\Delta t}{\mathrm{ms}}\right)^{-2} . \end{aligned}$$

Even at $d \sim$ kpc, $T_B \sim 10^{23}/\Gamma^2\,\mathrm{K}$. Incoherent broad-band radio emission from strong astronomical sources is usually synchrotron radiation. Upper limits on T_B are typically no larger than a few times $10^{13}\,\mathrm{K}$ (Kovalev et al., 2005). This is consistent with an upper limit on $T_B \sim 10^{12}\,\mathrm{K}$ in the source frame set by the Compton catastrophe (Frank et al., 1992) with somewhat higher values due to beaming in AGN jets.

Terrestrial communications at radio wavelengths invariably involve coherent sources. Could FRBs be signals beamed at us from advanced civilizations? Might negatively chirped ms pulses be transmitted to facilitate their detection? Advanced civilizations would know the power of de-dispersing radio signals to investigate pulsars. They would also be aware of planets in their neighborhoods and have identified those with atmospheres suitable for, or perhaps even modified by, biological life. After all, this information will be available to us before the end of this century.

How might advanced civilizations configure antennas to transmit narrow beams? Arrays of small telescopes are preferable to large filled apertures and also limit capital costs. With baseline, b, and transmitted power, P_T, the flux density of a broad-band signal received at distance d would be

$$S_\nu \sim \left(\frac{b}{cd}\right)^2 \nu P_T \,. \tag{1.6}$$

Recasting the above equation with S_ν scaled by Jy as appropriate for a FRB yields

$$P_T \sim 10^9 \left(\frac{b}{10^3\,\mathrm{km}}\right)^{-1}\left(\frac{d}{\mathrm{kpc}}\right)^2\left(\frac{\nu}{\mathrm{GHz}}\right)^{-1}\left(\frac{S_\nu}{\mathrm{Jy}}\right)\mathrm{watt}\,, \tag{1.6}$$

---

[4] Unless FRBs are extragalactic, this is merely their contribution to the radio background near our position in the Galaxy.

a modest power requirement even by current terrestrial standards.[5]

Accounting for a burst arrival rate at Earth $\sim 0.1\,\mathrm{s}^{-1}$ is the most challenging part of this exercise. With only a handful of detected FRBs, the fraction of planets hosting an advanced civilization might be quite modest. But then, the Earth must have been recognized as a particular object of interest to target. If this hypothesis has merit, the positions from which bursts arrive should eventually repeat. That would provide a lower limit to the number of our more advanced neighbors.

1.6 Strong Electric Fields

The flux of energy carried by an electromagnetic wave is $F = cE^2/4\pi$. Thus the electric field at the observer associated with a broad-band pulse of flux density S_ν is

$$E_o \sim \left(\frac{4\pi S_\nu \nu}{c}\right)^{1/2} \sim 10^{-12}\left(\frac{S_\nu}{\mathrm{Jy}}\right)^{1/2}\left(\frac{\nu}{\mathrm{GHz}}\right)^{1/2} \mathrm{esu}\,. \tag{1.6}$$

At separation r from a source at distance d, the electric field is larger, $E = (d/r)E_o$. For r smaller than

$$\begin{aligned} r_{\mathrm{rel}} &\sim \frac{eE_o d}{2\pi m_e c\nu} \\ &\sim 10^{13}\left(\frac{S_\nu}{\mathrm{Jy}}\right)^{1/2}\left(\frac{\nu}{\mathrm{GHz}}\right)^{-1/2}\left(\frac{d}{\mathrm{Gpc}}\right)\mathrm{cm}\,, \end{aligned} \tag{1.6}$$

the electric field is strong in the sense that it could accelerate an electron from rest up to relativistic energy on timescale comparable to $(2\pi\nu)^{-1}$. A free electron would maintain a position of nearly constant phase, in essence surfing on the wave (Gunn & Ostriker, 1969). For E given by Eq. (1.6) and $r \ll r_{\mathrm{rel}}$, the electron would reach a Lorentz factor

$$\gamma \sim \left(\frac{r_{\mathrm{rel}}}{r}\right)^{2/3}\,. \tag{1.6}$$

Acceleration of electrons in a thermal plasma by a strong broadband pulse would be more complicated. It is plausible that the electrons would drag the positive ions along with them to create an outgoing shock wave. Whether this might lead to the emission of coherent GHz radio waves is an open question that is best left for a separate investigation.

It is informative to compare the strength of the electric field near a cosmological FRB with that of giant pulses from the Crab pulsar. Sallmen et al. (1999) studied giant pulses in different frequency bands. At 0.6 GHz, $S_\nu \sim 7000$ Jy whereas at 1.4 GHz, $S_\nu \sim 3000$ Jy. Since the Crab is estimated to be at $d \sim 2.2\,\mathrm{kpc}$ (Manchester et al., 2005), the corresponding values of r_{rel} are a few times 10^9 cm in both bands. These values of r_{rel} are about 10 times larger than the radius of the Crab's light cylinder (Manchester et al., 2005), but much smaller than r_{rel} for FRB 110220.

1.7 Discussion & Conclusions

We discuss several properties of FRBs. We conclude that their high DMs cannot be attributed to a stellar corona or a galactic HII region. Thus, if astronomical, they are extra-galactic sources. We also argue that the propagation through the IGM is unlikely to lead to measurable scatter broadening of GHz pulses. Thus if scatter broadening is confirmed, it would suggest that the sources are located in dense regions of external galaxies and raise the possibility that a substantial fraction of their DMs are produced there.

---

[5] Scattering by plasma density fluctuations in the interstellar medium of typical paths would not increase the angular width of these beams.

Few sources at Gpc distances are plausible candidates for producing ms pulses with Jy flux densities. Neutron stars and stellar mass black holes have dynamical timescales of the right order and their gravitational binding energies are more than sufficient. How the release of binding energy might power a FRB is not clear. Gravitational waves can be released on ms timescales, but their coupling to GHz radio waves is likely to be much slower. Neutrinos carry away most of the binding energy, but only over several seconds (Bionta et al., 1987). The sudden release of magnetic energy, perhaps in a giant magnetar flare (Lyubarsky (2014)) or during the collapse of a magnetar into a BH (e.g., Falcke & Rezzolla (2013)) seems a better bet. An advantage of these proposals is that the initial energy is released in electromagnetic form. However, its rapid up-conversion to GHz frequencies poses a hurdle. Whether it can be overcome by the acceleration of dense plasma in strong EM fields is questionable. Moreover, it is doubtful whether these events occur with sufficient frequency to account for FRBs.

Chapter 2

Secular Interaction in Pulsar Triple System J0337+1715

2.1 Introduction

PSR J0337+1715 is a $M = 1.4M_\odot$ ms pulsar with two white dwarf (WD) companions. The inner and outer have masses $m_1 \simeq 0.2M_\odot$ and $m_2 \simeq 0.4M_\odot$, and move on nearly circular and coplanar orbits with periods of $P_1 \simeq 1.6\delta$ and $P_2 \simeq 327\delta$, and eccentricities $e_1 \simeq 6.9 \times 10^{-4}$ and $e_2 \simeq 3.5 \times 10^{-2}$. Exquisite timing of the pulsar's pulses enabled Ransom et al. (2014) to fit the system's parameters to striking accuracy. Because of the large disparity in orbital periods, mean motion resonances may be neglected. Thus secular interactions govern the system's long-term evolution.

Secular dynamics is an approximation in which each body is replaced by an elliptical wire spread along its orbit. Unless apsidal lines align, mutual torques give rise to angular momentum exchanges. Fractional energy exchanges are much slower than those of angular momentum, $|\dot{E}/E| \ll |\dot{J}/J|$, where E and J denote orbital energy and angular momentum. We ignore energy exchanges and take semi-major axes to be constants.

Conventional celestial mechanics was developed to study the solar system. It is optimized for systems with a massive central body and multiple much smaller ones. Two-body Keplerian orbits, each consisting of the central mass and one of its companions, comprise the zeroth order state. Perturbations due to gravitational interactions among the small bodies modify the Keplerian orbital elements. Because the WD masses are within an order of magnitude of the mass of the neutron star (NS), the standard procedure fails for the pulsar triple system under consideration here . A more appropriate procedure is to take the unperturbed system to consist of an inner and an outer binary with the former made up of the NS and the $0.2M_\odot$ WD and the latter by the $0.4M_\odot$ WD and the inner binary. Perturbations due to interactions between the binaries are small because their semi-major axes are so different (Ford et al., 2000; Rafikov, 2014).

Our paper is organized as follows. We develop a compact formalism for secular interactions in a hierarchical coplanar triple system in Section 2.2. Included are precession terms due to general relativity (GR) along with tidal and rotational distortions of the inner WD. Interactions of modes with convective eddies are considered in Section 2.3. Section 2.4 applies our model to J0337+1715. We predict that secular evolution will be detected in the near future and that the effects of general relativity (GR) will become apparent. In Section 2.5, we compare our secular formalism with results obtained by direct numerical integrations obtained using the program Mercury (Chambers, 1999). The agreement is good except that the numerical results yield short-term variations of the osculating eccentricities. We argue that these are deceptive. Section 2.6 summarizes our conclusions.

Although couched in different language, some material in our paper is closely related to that in Ford et al. (2000) and Rafikov (2014). The former provides a more general treatment of hierarchical triple systems than we do whereas the latter contains an analytic analysis of the same system that we are investigating. In areas of overlap, our results agree with those obtained in Rafikov (2014).

2.2 Secular Interaction in Co-planar Triple System

We use 1 and 2 to label the inner and outer binary orbits and/or WDs. We denote the vector from the NS to the inner WD by $\mathbf{r}_1$ and the one from the center of mass of the inner binary to the outer WD by $\mathbf{r}_2$. Manipulation of the inertial-frame equations of motion yields

$$\begin{aligned} \mu_1 \ddot{\mathbf{r}}_1 &= -\nabla_1 U\,, && (2.1)\\ \mu_2 \ddot{\mathbf{r}}_2 &= -\nabla_2 U\,, && (2.2) \end{aligned}$$

with potential

$$U = -\frac{GMm_1}{r_1} - \frac{GMm_2}{\left|\frac{m_1}{M+m_1}\mathbf{r}_1 + \mathbf{r}_2\right|} - \frac{Gm_1m_2}{\left|\frac{M}{M+m_1}\mathbf{r}_1 - \mathbf{r}_2\right|}\,. \tag{2.3}$$

Here ∇_j indicates gradient with respect to $\mathbf{r}_j$ $(j = 1, 2)$ and reduced masses are $\mu_1 \equiv Mm_1/(M+m_1)$ and $\mu_2 \equiv (M + m_1)m_2/(M + m_1 + m_2)$. We average U over the zeroth-order orbits described by $\mathbf{r}_1 = r_1(\cos\theta_1, \sin\theta_1, 0)$, $\mathbf{r}_2 = r_2(\cos\theta_2, \sin\theta_2, 0)$ and

$$\begin{aligned} r_1 &= \frac{a_1(1-e_1^2)}{1+e_1\cos(\theta_1-\varpi_1)}\,, && (2.4)\\ r_1^2\dot{\theta}_1 &= \left(G(M+m_1)a_1(1-e_1^2)\right)^{1/2}\,, && (2.5)\\ r_2 &= \frac{a_2(1-e_2^2)}{1+e_2\cos(\theta_2-\varpi_2)}\,, && (2.6)\\ r_2^2\dot{\theta}_2 &= \left(G(M+m_1+m_2)a_2(1-e_2^2)\right)^{1/2}\,, && (2.7) \end{aligned}$$

where a is semi-major axis, e is eccentricity, and ϖ is the longitude of pericenter. The mean motions are $n_1 \equiv (G(M + m_1)/a_1^3)^{1/2}$ and $n_2 \equiv (G(M + m_1 + m_2)/a_2^3)^{1/2}$. Retaining terms up to second order in eccentricity,[1] yields the secular potential

$$\begin{aligned} U_{\text{sec}} &= -\frac{3}{8}\alpha^2(e_1^2+e_2^2)\frac{GMm_1m_2}{a_2(M+m_1)} + \frac{15}{16}\alpha^3(e_1e_2)\\ &\quad\times\cos(\varpi_1-\varpi_2)\frac{GMm_1m_2(M-m_1)}{a_2(M+m_1)^2}\,, && (2.8) \end{aligned}$$

where $\alpha \equiv a_1/a_2$.

We verify that the inertial-frame total angular momentum is given by

$$\begin{aligned} \mathbf{J} &= \sum_{j=1}^{2}\mathbf{J}_j \equiv \sum_{j=1}^{2}\mu_j\mathbf{r}_j\times\dot{\mathbf{r}}_j\\ &= \hat{\mathbf{z}}\left(\sum_{j=1}^{2}J_{j,c}-\delta J_j\right)\,, && (2.9) \end{aligned}$$

where $\hat{\mathbf{z}} = (0, 0, 1)$. The circular part of angular momentum for each orbit, $J_{j,c} \equiv \mu_j a_j^2 n_j$, is conserved because a_j is constant. It is the angular momentum deficit, $\delta J_j \equiv J_{j,c}e_j^2/2$, that is exchanged under interactions. The total angular momentum deficit reads

$$\mathcal{J} = \sum_{j=1}^{2}\delta J_j = \mathcal{I}^\dagger\mathcal{I}\,, \tag{2.10}$$

where $\mathcal{I}$ is a two dimensional column vector with components $I_j \equiv (\mu_j n_j/2)^{1/2}a_j e_j \exp(i\varpi_j)$ and †

---

[1] The zeroth order term is constant, and the one of first order vanishes.

denotes Hermitian conjugate.

Secular evolution is governed by the equation of motion

$$\dot{\mathcal{I}} = i\mathbf{B}\mathcal{I}\,. \tag{2.11}$$

The Hamiltonian $\mathcal{H} \equiv U_{\rm sec}$ reads

$$\mathcal{H} \;=\; -\mathcal{I}^{\dagger}\mathbf{B}\mathcal{I}\,. \tag{2.12}$$

Conservation of both $\mathcal{H}$ and $\mathcal{J}$ follows immediately from equations (2.11) and (2.12). Elements of the symmetric 2×2 matrix

$$\mathbf{B} \equiv \begin{pmatrix} B_{11} & B_{12} \\ B_{12} & B_{22} \end{pmatrix} \tag{2.13}$$

read

$$B_{11} \;=\; \frac{3}{4} n_1 \alpha^3 \frac{m_2}{M+m_1}\,, \tag{2.14}$$

$$B_{22} \;=\; \frac{3}{4} n_1 \alpha^{7/2} \frac{M m_1 (M+m_1+m_2)^{1/2}}{(M+m_1)^{5/2}}\,, \tag{2.15}$$

$$\begin{aligned} B_{12} \;=\; & -\frac{15}{16} n_1 \alpha^{17/4} \frac{(M-m_1)(M m_1 m_2)^{1/2}}{(M+m_1)^{11/4}} \\ & \times (M+m_1+m_2)^{1/4}\,. \end{aligned} \tag{2.16}$$

Ford et al. (2000) previously studied secular theory for highly hierarchical triple systems. Our $\dot{e}$ and $\dot{\varpi}$ are derivable from their equations (46)-(52).

Substituting the trial solution, $\mathcal{I} \propto \exp(igt)$, into Eq. (2.11), we obtain two modes represented by the eigenvalues and normalized eigenvectors of $\mathbf{B}$. Mode p (parallel) has $\varpi_1 = \varpi_2$, and Mode a (anti-parallel) has $\varpi_1 = \varpi_2 + \pi$. In each mode, both pericenters precess at the same rate which is the corresponding eigenvalue,

$$g_p \;=\; \frac{1}{2}\left((B_{11}+B_{22}) - \Delta g\right)\,, \tag{2.17}$$

$$g_a \;=\; \frac{1}{2}\left((B_{11}+B_{22}) + \Delta g\right)\,. \tag{2.18}$$

The relative precession rate

$$\Delta g \equiv g_a - g_p = \sqrt{(B_{11}-B_{22})^2 + 4B_{12}^2}\,. \tag{2.19}$$

Components of the eigenvectors satisfy

$$\frac{I_{p,1}}{I_{p,2}} = -\frac{I_{a,2}}{I_{a,1}} = \frac{(-B_{11}+B_{22}+\Delta g)}{2|B_{12}|}\,. \tag{2.20}$$

The first minus sign in Eq. (2.20) appears because $\exp i(\varpi_1 - \varpi_2) = -1$ for Mode a. The general solution is a linear combination of the two modes,

$$\mathcal{I}(t) = c_p \hat{\mathcal{I}}_p \exp(i g_p t) + c_a \hat{\mathcal{I}}_a \exp(i g_a t)\,, \tag{2.21}$$

where $\hat{}$ signifies a normalized vector. Unless either c_p or c_a vanishes, e_1/e_2 and $\varpi_1 - \varpi_2$ oscillate at frequency Δg.

Since $\mathbf{B}$ is symmetric, $\hat{\mathcal{I}}_a^\dagger \hat{\mathcal{I}}_p = 0$. Contributions from $\hat{\mathcal{I}}_a$ and $\hat{\mathcal{I}}_p$ to $\mathcal{H}$ and $\mathcal{J}$ are thus separable,

$$\begin{aligned} \mathcal{H} &= \frac{1}{2} g_p |c_p|^2 + \frac{1}{2} g_a |c_a|^2 \equiv \mathcal{H}_p + \mathcal{H}_a \, , \\ \mathcal{J} &= \frac{1}{2}|c_p|^2 + \frac{1}{2}|c_a|^2 \equiv \mathcal{J}_p + \mathcal{J}_a \, . \end{aligned} \tag{2.22}$$

The ratios $\mathcal{H}_a/\mathcal{H}_p$ and $\mathcal{J}_a/\mathcal{J}_p$ are measures of the relative strengths of Modes a and p. We note that $|c_p|^2$ and $|c_a|^2$ are actions and thus might behave as adiabatic invariants under slow variations of the masses and orbits.

Given that $\alpha \ll 1$ and $B_{11} \gg B_{22} \gg B_{12}$, the following approximations apply:

$$g_p \sim B_{22} \ll g_a \sim B_{11} \, , \tag{2.23}$$

$$\Delta g \sim B_{11} - B_{22} \, . \tag{2.24}$$

Thus Mode p precesses a factor $g_p/g_a \sim \alpha^{1/2}(m_1/m_2)$ more slowly than Mode a. For the eigenvectors,

$$\frac{I_{p,1}}{I_{p,2}} = -\frac{I_{a,2}}{I_{a,1}} \sim \frac{|B_{12}|}{B_{11}} \sim \alpha^{5/4} \left(\frac{m_1}{m_2}\right)^{1/2} \, , \tag{2.25}$$

which yields

$$\frac{e_{p,1}}{e_{p,2}} \sim \alpha \, , \tag{2.26}$$

$$\frac{e_{a,1}}{e_{a,2}} \simeq \alpha^{-3/2} \frac{m_2}{m_1} \, . \tag{2.27}$$

2.2.1 Additional precession rates

General relativity (GR) and tidal and rotational distortions of the inner WD cause its pericenter to precess forward at rates (Wu & Goldreich, 2002),

$$\left.\frac{d\varpi_1}{dt}\right|_{GR} = 3 n_1 \frac{G(M+m_1)}{c^2 a_1} \, , \tag{2.28}$$

$$\left.\frac{d\varpi_1}{dt}\right|_{\rm tide} = \frac{15}{2} n_1 k_2 \frac{M}{m_1} \left(\frac{R_1}{a_1}\right)^5 \, , \tag{2.29}$$

$$\left.\frac{d\varpi_1}{dt}\right|_{J_2} = \frac{1}{2} n_1 k_2 \left(\frac{\Omega_1}{n_1}\right)^2 \frac{M}{m_1} \left(\frac{R_1}{a_1}\right)^5 \, . \tag{2.30}$$

The Love number $k_2 \simeq 0.29$ for an $n = 1.5$ polytrope (Chandrasekhar (1933)), which is a reasonable proxy for a WD. The WD's radius is denoted by R. We neglect these effects on the outer WD because $a_2 \gg a_1$ and all the above precession rates decline with distance from the NS. The pulsar is so dense that its tidal and rotational deformations are negligible. We denote the total additional precession rate of $\dot{\varpi}_1$ by Δ and add it to B_{11}. In so doing, we make the plausible assumption that inner WD's spin speed, Ω_1, is synchronized with its mean motion, n_1.

2.3 Mode Damping and Excitation

2.3.1 Damping

Dissipation associated with the tides raised in the WDs by the pulsar act to damp their orbital eccentricities. We define $\tau_j \equiv e_j/\dot{e}_j|_{\rm damp}$, which implies a complementary change rate for I_j, namely $\dot{I}_j|_{\rm damp} = -I_j/\tau_j$ which we account for by replacing B_{jj} by $B_{jj} + i/\tau_j$ in Eq. (2.13). Because τ's are much longer than the precession period, they introduce small corrections to $\mathbf{B}$. Thus we retain the old eigenvectors while expanding the eigenvalues to first order in the $1/\tau_j$. This procedure adds damping terms to g_p and g_a which read:

$$\begin{aligned}\gamma_p &= \frac{1}{2\tau_2}\left(1+\frac{B_{11}-B_{22}}{\Delta g}\right)+\frac{1}{2\tau_1}\left(1-\frac{B_{11}-B_{22}}{\Delta g}\right)\\ &\simeq \frac{1}{\tau_2}+\frac{m_1}{m_2}\frac{\alpha^{5/2}}{\tau_1} \qquad (2.31)\end{aligned}$$

and

$$\begin{aligned}\gamma_a &= \frac{1}{2\tau_1}\left(1+\frac{B_{11}-B_{22}}{\Delta g}\right)+\frac{1}{2\tau_2}\left(1-\frac{B_{11}-B_{22}}{\Delta g}\right)\\ &\simeq \frac{1}{\tau_1}+\frac{m_1}{m_2}\frac{\alpha^{5/2}}{\tau_2} \qquad (2.32)\end{aligned}$$

As a consequence of the orbital eccentricity ratios in modes p and a, dissipation in the inner WD selectively damps Mode a and that in the outer WD selectively damps Mode p.

2.3.2 Excitation

Phinney (1992) argues that the orbital eccentricity of a binary composed of a pulsar and a low-mass WD is set during the final stages of Roche lobe overflow (RLO) by the WD's progenitor.[2] Convection in the progenitor's extended envelope creates a fluctuating quadrupole that stochastically excites orbital eccentricity while turbulent viscosity simultaneously damps it. These competing processes drive the epicyclic energy, $E_{\rm ec} \equiv n\delta J$, toward equipartition with the kinetic energy of eddies whose lifetimes are closest to the orbit period. Equipartition is approached on the eccentricity damping timescale, τ_e, which is much shorter than the duration of RLO. Eccentricities established in this manner increase with orbit period as a consequence of the increase in eddy kinetic energy with eddy lifetime. Observational data offers support for Phinney's proposal (Tauris et al., 2012). In what follows, we apply the equipartition concept to the pulsar triple system. However, our focus is on the epicyclic energies of modes p and a rather than those of the binary orbits.

Modal epicyclic energies are defined by

$$\begin{aligned}E_{p,\rm ec} &\equiv n_1|I_{p,1}|^2+n_2|I_{p,2}|^2\\ &\equiv \frac{1}{2}\mu_1(n_1a_1e_{p,1})^2+\frac{1}{2}\mu_2(n_2a_2e_{p,2})^2 \qquad (2.33)\end{aligned}$$

and

$$\begin{aligned}E_{a,\rm ec} &\equiv n_1|I_{a,1}|^2+n_2|I_{a,2}|^2\\ &\equiv \frac{1}{2}\mu_1(n_1a_1e_{a,1})^2+\frac{1}{2}\mu_2(n_2a_2e_{a,2})^2\,. \qquad (2.34)\end{aligned}$$

These epicyclic energies are constants of motion under evolution governed by the Hamiltonian in equation (2.12). Epicyclic energies may also be defined for the inner and outer binary orbits. They vary on the secular timescale. Moreover, their sum also varies and only equals the sum of the modal epicyclic energies when the inner and outer binary apses are either parallel or anti-parallel, $\sin(\varpi_1-\varpi_2)=0$.

Tidal interactions during the LMXB stage that gave rise to the outer WD drove the epicyclic energy of Mode p toward equipartition with a single eddy. Based on estimates for the duration of Roche lobe overflow and the rate of eccentricity damping by tides, energy equipartition should have persisted until termination of the LMXB phase. During the outer LMXB phase, τ_1 is essentially infinite. Thus according to Eqs. (2.31) and (2.32), $\gamma_a \sim 10^{-4}\gamma_p$. It follows that the epicyclic energy of Mode a probably experienced little progress toward equipartition. The same story applied during

---

[2] During RLO, these systems are observed as low mass x-ray binaries (LMXRB)

the inner LMXB stage, except the roles of Mode p and Mode a were reversed. In this scenario, the order in which the inner and outer WDs formed is not crucial. In either case, the epicyclic energy in Mode p ends up much larger than that in Mode a because the energies of convective eddies whose lifetimes are closest to the orbital period are greater for larger orbital periods.

As mentioned previously, the modal angular momentum deficits, $\mathcal{J}_p$ and $\mathcal{J}_a$ are actions of the Hamiltonian given by equation (2.12). Thus they are invariants under slow changes of masses and semi-major axis provided these occur independently of the secular oscillation. For example, orbital evolution during the formation of the second WD would change the epicyclic energy of the mode which achieved equipartition during the birth of the first WD. If the angular momentum deficit of the mode remained invariant, its epicyclic energy would change in proportion to the change of its precession rate.

2.4 Secular Oscillation of J0337+1715

We adopt stellar masses, orbital periods, eccentricities and longitudes of pericenter from Table 1 in Ransom et al. (2014). The semi-major axes are obtained from $a_1 = (G(M+m_1)/n_1^2)^{1/3}$ and $a_2 = (G(M+m_1+m_2)/n_2^2)^{1/3}$. Inserting these parameters into the elements of matrix $\mathbf{B}$, we obtain

$$\mathbf{B} \simeq \begin{pmatrix} 2.34405 & -0.0119143 \\ -0.0119143 & 0.129615 \end{pmatrix} \times 10^{-10}\,\mathrm{s}^{-1}\,. \tag{2.35}$$

Here B_{11} includes Δ,

$$\begin{aligned} \Delta &\equiv \left.\frac{d\varpi_1}{dt}\right|_{\mathrm{GR}} + \left.\frac{d\varpi_1}{dt}\right|_{\mathrm{tide}} + \left.\frac{d\varpi_1}{dt}\right|_{\mathrm{J_2}} \\ &\simeq (6.77 + 0.0315 + 0.00210) \times 10^{-11}\,\mathrm{s}^{-1} \\ &\simeq 6.80 \times 10^{-11}\,\mathrm{s}^{-1}\,, \end{aligned} \tag{2.36}$$

which is dominated by GR and contributes $\simeq 30\%$ to B_{11}. Table (2.1) and Fig. (2.1) compare results obtained by either excluding or including Δ from which we make several observations:

1. According to rows 7 and 8, the system is currently dominated by Mode p, which is consistent with the equipartition scenario assumed in Section 2.3.

2. Row 4 shows that Δ induces a shorter secular oscillation period, as predicted by Eq. (2.24) since Δ enhances B_{11}. It also shrinks the oscillation amplitudes by an order of magnitude as exhibited by comparing Fig. (2.2) with the solid line in the upper panel of Fig. (2.1). Secular oscillations appear because the system's state is not pure Mode p, but also contains a small contribution from Mode a.

3. We see, from rows 9-12, that changes over a year exceed the measurement accuracies cited by Ransom et al. (2014). Especially, measurements of $e_1 \cos\varpi_1$ and $e_1 \sin\varpi_1$ can separate the cases with and without Δ. If an accurate determination of Δ were made, it would constrain k_2 of the inner WD (cf. Eqs. 2.28-2.29).

4. From private communications with Scott M. Ransom and Anne M. Archibald, we know that in fitting their timing data, orbit elements were assumed constant and GR was not taken into account. With additional data, both restrictions may be lifted. As described in the previous paragraph, the effects of GR should be apparent within a short time.

Table 2.1. Secular Oscillation

	Parameter	Without Δ	With Δ	Difference
1	g_p (10^{-11}Hz)	1.2952	1.2955	-2.8E-4
2	g_a (10^{-11}Hz)	16.6	23.4	-6.8
3	Δg (10^{-11}Hz)	15.3	22.1	-6.8
4	$2\pi/\Delta g$ (kyr)	1.298	0.899	0.40
5	$(e_1/e_2)_p$	0.0278	0.0193	8.5E-3
6	$(e_1/e_2)_a$	461.4	665.9	-204.6
7	$\mathcal{J}_a/\mathcal{J}_p/10^{-8}$	536.6	4.5	532.1
8	$E_{a,\text{ec}}/E_{p,ec}/10^{-6}$	64.9	1.01	63.9
9	$\delta(e_1 \cos \varpi_1)/10^{-8}$	114.0	-33.06	147.1
10	$\delta(e_1 \sin \varpi_1)/10^{-8}$	-1.620	-21.94	20.32
11	$\delta(e_2 \cos \varpi_2)/10^{-9}$	-1.44E4	-1.44E4	1.1E-3
12	$\delta(e_2 \sin \varpi_2)/10^{-9}$	-1.42E3	-1.42E3	-7.7E-3

Note. — Columns 3 and 4 show results without and with Δ included in B_{11}. Column 5 is calculated by subtracting Column 4 from Column 3. The expression Ex means 10^x in some of the numerical values. According to Ransom et al. (2014), the accuracies of measurements for $e_1 \cos \varpi_1$ and $e_1 \sin \varpi_1$ are 10^{-8}, and those for $e_2 \cos \varpi_2$ and $e_2 \sin \varpi_2$ are 10^{-9}. Rows 9 to 12 show their changes after 1y, in multiples of their corresponding accuracies. Although the secular oscillation occurs on a thousand-year timescale, changes over 1y already exceed measurement accuracies. Differences between predictions without and with Δ are also detectable in $\delta(e_1 \cos \varpi_1)$ and $\delta(e_1 \sin \varpi_1)$. These could help test GR and constrain the tidal Love number, k_2, of the inner WD.

2.5 Comparison with Numerical Integration

We ran Mercury (Chambers, 1999), a symplectic integrator for Newtonian orbital dynamics, to evolve the pulsar triple system over a secular period $\sim 10^3$y. Secular changes of e_1 were extracted from a 10 year average of the osculating orbital elements. As displayed in Fig. (2.2), the numerical and analytical results compare well; oscillation periods differ by $\simeq 0.6\%$ and oscillation amplitudes differ by $\simeq 2\%$. These differences are reduced by roughly half if the secular Hamiltonian is expanded to fourth order in both α and eccentricities. Inclusion of even higher order terms yields negligible improvement.

2.5.1 Osculating elements are deceptive

Classical perturbation theory is formulated in terms of osculating orbit elements. These are obtained by fitting a Keplerian ellipse to the instantaneous position and velocity of a perturbed orbit. Temporal variations of the elements describe how the perturbations evolve. Results of numerical integrations of N-body systems such as Mercury are often expressed in terms of oscillating elements. Osculating eccentricities obtained from short intervals of output from Mercury are displayed in figures 2.3 and 2.4.[3] Each varies over the corresponding orbit period.[4] These oscillations are deceptive. In the following paragraphs we explain how they arise. Our focus is on the inner binary orbit because the variation of its osculating eccentricity is more complex.

As a first step, consider a circular orbit in a potential consisting of a dominant monopole and an external axisymmetric quadrupole. We define $\beta \ll 1$ to be the ratio of the quadrupole to monopole potential evaluated at the orbit's radius, r_0. A simple exercise shows that the corresponding osculating elements $a_{osc} \approx (1+\beta)r_0$ and $e_{osc} \approx \beta$. Paradoxically, the osculating eccentricity does not vanish. Moreover, the true anomaly stays fixed at $f_{osc} = 0$ while the apse rotates with angular velocity $\dot{\varpi}_{osc} \approx n$.

---

[3] This is a purely Newtonian simulation. GR is not included.

[4] In this subsection, we neglect the small difference between orbit and epicyclic frequencies.

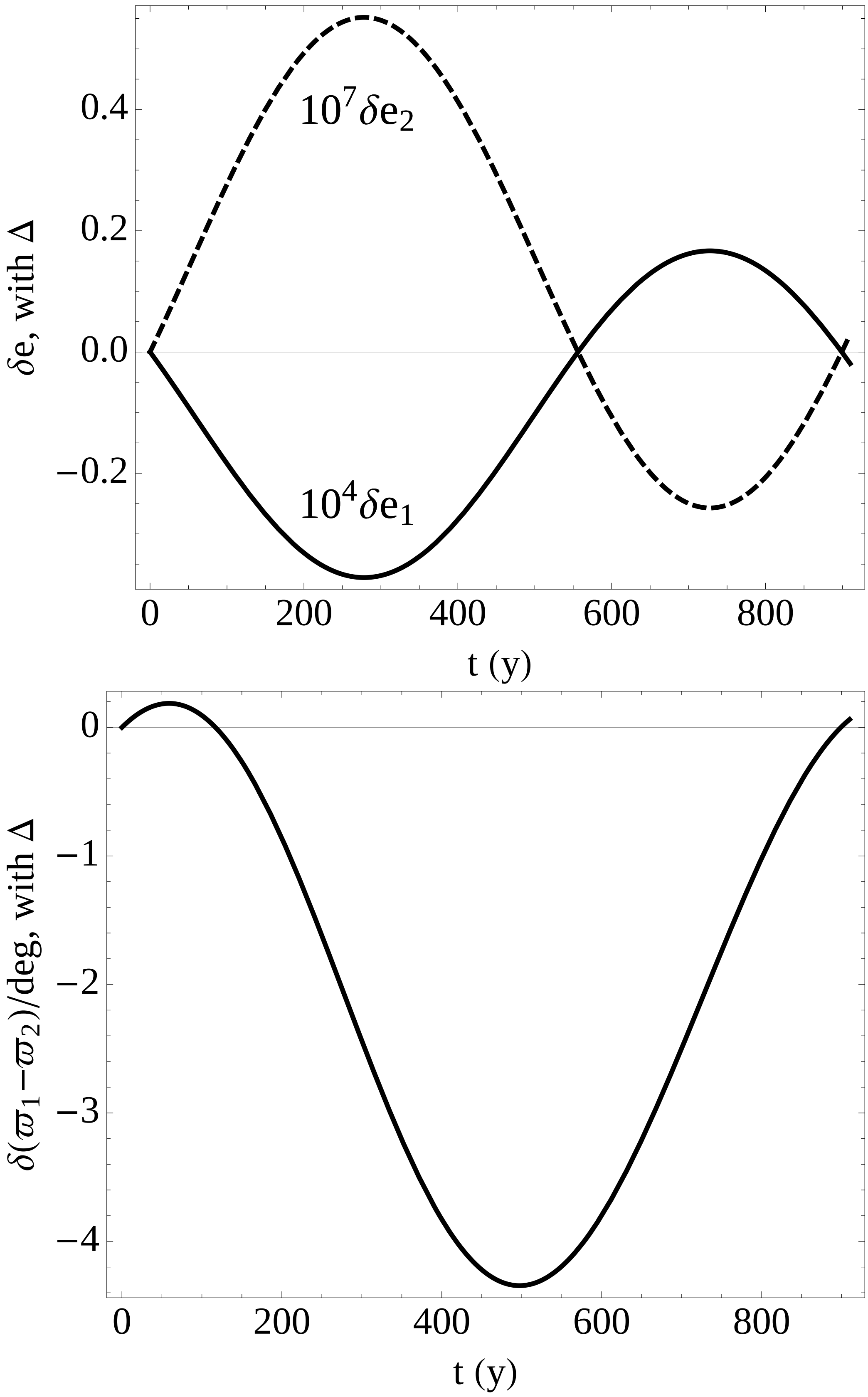

Figure 2.1 Upper panel: solid line: $10^4\delta e_1$; dashed line: $10^7\delta e_2$. Lower panel: solid line: $\delta(\varpi_1 - \varpi_2)$ in degrees.

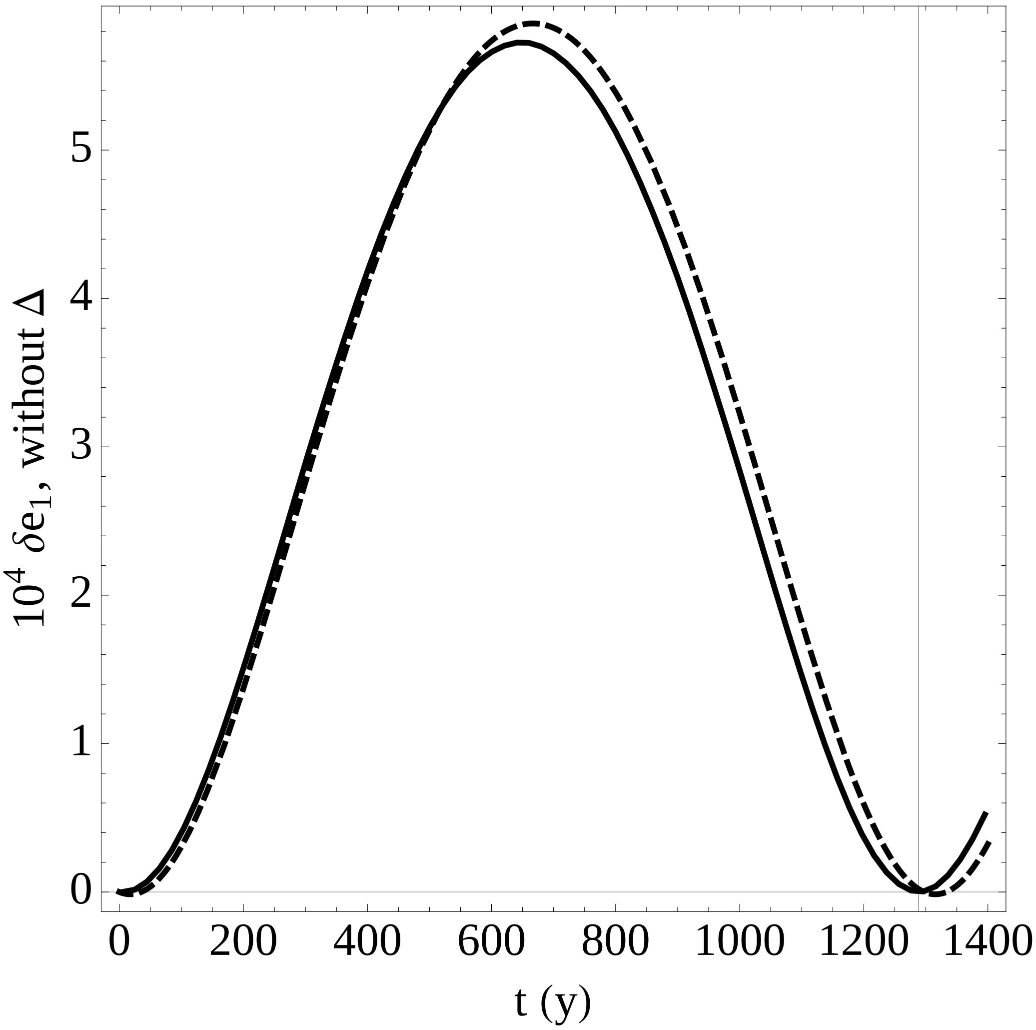

Figure 2.2 Comparison of the secular variations of e_1 over a precession cycle obtained from a numerical integration with Mercury (solid line) and the analytical model (dashed line) described in Section 2.2 with $\Delta = 0$. Oscillation periods are 1289y and 1297y respectively.

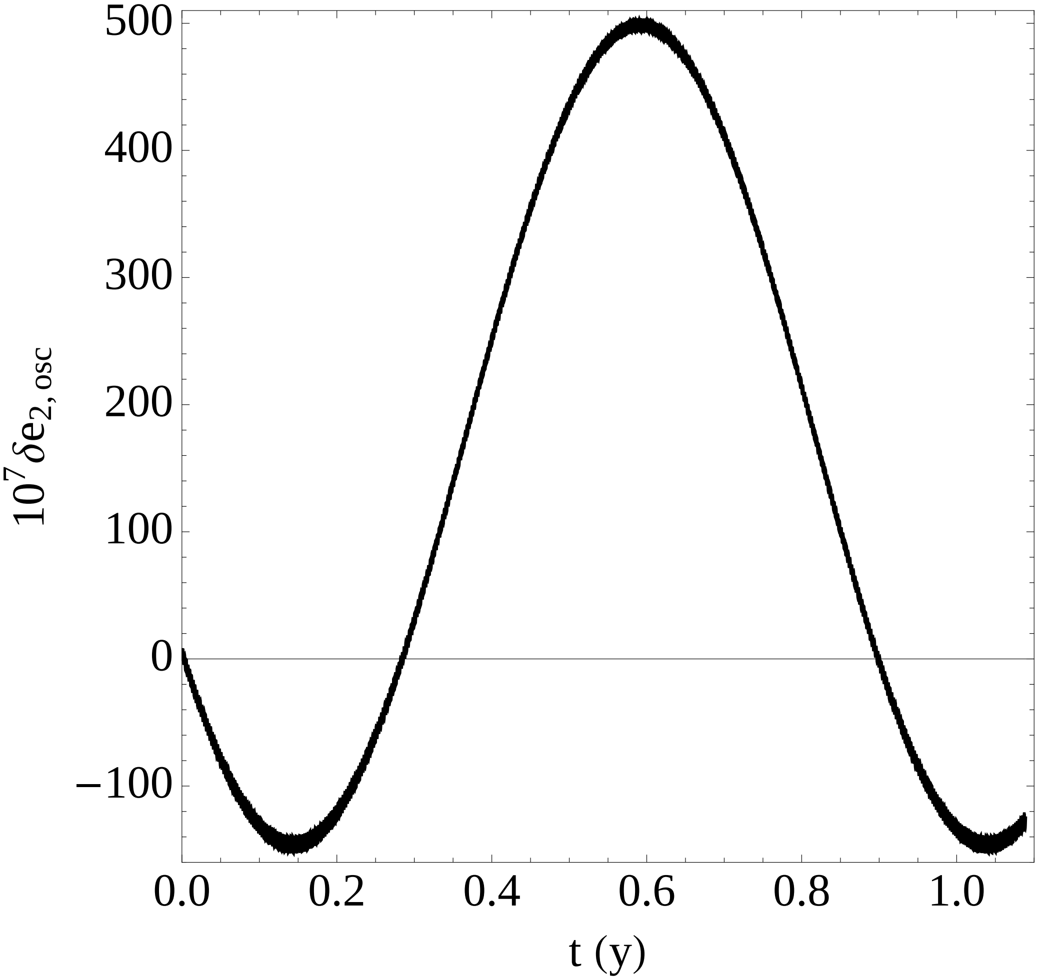

Figure 2.3 The variation of e_2 on the outer orbital period.

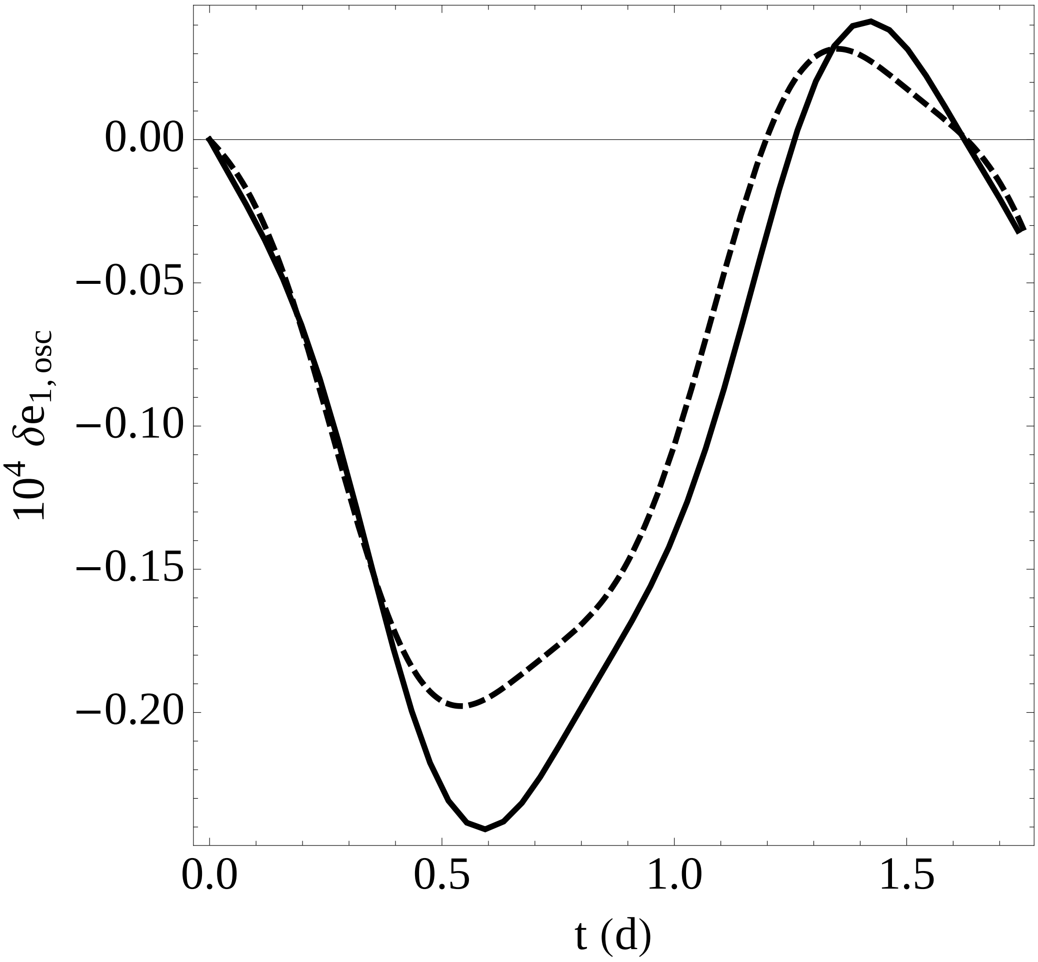

Figure 2.4 The variation of e_1 on the inner orbital period. Solid: δe_1 from the output from Mercury's simulation. Dashed: δe_1 from analytic solution for the inner orbit with the outer WD's quadruple potential.

Next we consider a less trivial example in which the orbit possesses a real eccentricity e. However, we maintain the assumption of an axisymmetric quadrupole. Here we obtain $e_{osc}^2 \approx e^2 + 2\beta e \cos(nt+\phi) + \beta^2$ along with the same $a_{osc} \approx (1+\beta)r_0$ as before. The value of ϕ is set as an initial condition. In the limit $\beta \ll e$, e_{osc} oscillates harmonically about e with amplitude β. Figure 2.3 displays an example of this behavior. Because $P_{\mathrm{orb},1} \ll P_{\mathrm{orb},2}$, the effects of the non-axisymmetric part of the quadruple potential almost average to zero.

Lastly, we keep all the quadrupole terms depending on r_1 in equation (2.3), which reduces to

$$U = -\frac{GMm_1}{r_1} - \frac{Gm_2\mu_1}{r_2}\left(\frac{r_1}{r_2}\right)^2 P_2(\cos\Delta\theta)\,, \tag{2.37}$$

$\Delta\theta = \cos^{-1}(\hat{\mathbf{r}}_1.\hat{\mathbf{r}}_2)$ circulates at frequency $\sim n_1$. Thus $P_2(\cos\Delta\theta) \sim (1 + 3\cos(2nt))/4$. As a consequence, the epicyclic motion possesses a forced oscillation at frequency $2n_1$ in addition to its free oscillation at frequency n_1. These two terms, together with the angle between the outer body's longitude and the inner body's apse, are responsible for the non-harmonic behavior illustrated by figure 2.4 which compares $e_{1,osc}$ derived analytically with the result obtained from Mercury.

2.6 Discussion and Conclusions

We study secular interactions in the pulsar triple system J0337+1715 utilizing a simplified version of a formalism for highly hierarchical triple systems developed by Ford et al. (2000). To second order in the orbital eccentricities, the secular evolution is described in terms of two orthogonal modes. In Mode p, the apses of the inner and outer binary orbit align whereas they are anti-aligned in Mode a. Mode a precesses more rapidly than Mode p. Eccentricities of the binary orbits oscillate at the secular frequency, the difference between the precession frequencies of Mode a and Mode p. The secular frequency corresponds to a long timescale $\sim 10^3$y. Nevertheless, secular changes are potentially detectable in the near future, thanks to the exquisite accuracy of measurements by Ransom et al. (2014). These should easily reveal the effects of GR on both the period and amplitude of the secular oscillation. Although more challenging, it might be possible to detect similar effects from the tidal and rotational deformations of the inner WD and thereby constrain its Love number. We generalize the beautiful theory of Phinney (1992) to apply to the excitation of eigenmodes. In this form it explains why the current system is dominated by Mode p with Mode a making only a minor contribution even to the eccentricity of the inner binary's orbit.

Tidal dissipation in the inner WD mainly damps Mode a. The mode's current amplitude, although small with respect to that of Mode p, is at the high end of what might be expected from the eccentricities of pulsar He-core WD binaries with orbital periods of order a few days. Thus it is unlikely that Mode a's tidal damping timescale is much shorter than ~ 500 My, the age we estimate from WD cooling models in Althaus et al. (2013). This enables us to place a lower limit on the effective tidal Q parameter for this particular WD during its lifetime of

$$Q \simeq ((1+k_2)^2 M^2 n_1 R_1^8 \tau)/(a_1^8 m_1^2) \gtrsim 10^6\,. \tag{2.38}$$

By comparison, Piro (2011) assumes that luminosities in the binary WD system J0651 are contributed by asynchronous tidal heating and thereby sets upper limits for Q of $\sim 7\times10^{10}$ for the He-core WD and $\sim 2\times10^7$ for the CO-core WD.

Chapter 3

Mean motion resonances involving solar system satellites

3.1 Introduction

An influential paper by Roy & Ovenden (1954) established that the number of mean motion resonances (MMRs) between pairs of solar system satellites exceeds that expected from a random distribution of mean motions. Subsequently, Goldreich (1965) proposed that MMRs form as the result of convergent outward migration of satellite orbits driven by tidal torques from their parent planets. He argued that this could account for the origin of the MMRs between the Saturnian satellites, Mimas-Tethys and Enceladus-Dione but not that between Titan-Hyperion.[1] He also suggested that MMRs between the Jovian satellites Io-Europa and Europa-Ganymede were tidal in origin.

Convergent migration does not guarantee the formation of a MMR so the probability of capture into resonance is an important quantity. Initial steps toward calculating it were taken by Allan (1969) and Sinclair (1972) who estimated a small, 0.04, capture probability for the MMR between Mimas-Tethys. Yoder (1979) developed a more accurate diagrammatic method and Henrard (1982) showed how capture probabilities were related to adiabatic invariants. Following Henrard (1982), Borderies & Goldreich (1984) derived simple expressions for capture probabilities.

It is natural to wonder how long a MMR, once formed, will last. Lin & Papaloizou (1979) noted that there exists an equilibrium state for some MMRs in which convergence toward exact resonance is halted by tidal damping of one or both of the resonant satellites' orbital eccentricities. In a more recent development, it was found that eccentricity damping may promote librational overstability leading to passage through resonance (Meyer & Wisdom, 2008; Goldreich & Schlichting, 2014). We apply the analytic criterion for overstability derived by Goldreich & Schlichting (2014) to classify MMRs between pairs of solar system satellites.

Our paper is structured as follows. Section 3.2 presents a physical picture of librational overstability. We divide satellite MMRs into two groups. Group I contains the pairs Io-Europa, Europa-Ganymede and Enceladus-Dione. Their resonant arguments exhibit small librations. We treat this group in section 3.3. Group II contains the remaining MMRs, Mimas-Tethys and Titan-Hyperion. Their resonant arguments show large librations. We analyze this group in section 3.4. Our final section 3.5 consists of two parts. The first compares resonant and tidal torques and speculates about how Lainey et al. (2012) might have erred in concluding that Mimas is migrating toward Saturn. The second part describes some vestiges of past MMRs. Particular attention is given to the orbital eccentricity of Mimas and the possibility that Mimas possesses an internal ocean. We relegate technical details to the appendix. These include a table 3.3 listing relevant parameters for satellites involved in MMRs and details regarding the resonant dynamics of MMRs that are not covered in the main text.

---

[1] Peale (1978) discusses the origin of Titan-Hyperion MMR.

3.2 Classification of MMRs

We begin by reviewing selected features of first order, eccentricity-type, MMRs following the description given in Goldreich & Schlichting (2014). At this point we are only concerned with Hamiltonian dynamics. Tidal effects will be introduced later. The reader may wish to consult standard references or Goldreich & Schlichting (2014) for additional details. Each resonance is characterized by a single critical argument $\phi = (j+1)\lambda' - j\lambda - \varpi$, where λ and ϖ denote mean longitude and longitude of pericenter, and a prime labels the outer body. We assume that the orbits of both satellites lie in the planet's equatorial plane. We can also neglect the orbital eccentricity of the outer satellite. For the moment it suffices to treat the inner satellite as a test particle. Although this is a special example, the physical concepts we emphasize apply more generally to both eccentricity-type and inclination-type MMRs.

As described above, the dynamical system has 2 degrees of freedom. Because the outer satellite moves on a circular orbit, the Jacobi constant of the inner satellite, $\mathcal{H} \equiv E - n'L$, is a constant of motion.[2] Denoting the Jacobi constant by $\mathcal{H}$ is deliberate. It is the Hamiltonian corresponding to conjugate coordinate and momentum, ϕ and e^2. Moreover, because λ and ϖ only appear in the combination $\lambda + \varpi$, $\lambda - \varpi$ is an ignorable coordinate. This implies the existence of a second constant of motion labelled k by Goldreich & Schlichting (2014). Expressions for k and $\mathcal{H}$ read:

$$k(\phi, e^2) \equiv \frac{3}{2} j^2 e^2 - \frac{\beta\mu'}{e}\cos\phi + \frac{\dot{\phi}}{n} \tag{3.1}$$

and

$$\mathcal{H}(\phi, e^2) \equiv k e^2 - \frac{3}{4} j^2 e^4 + 2\beta\mu' e\cos\phi \,. \tag{3.2}$$

In the above, β is a j-dependent constant of order unity and μ' is the ratio of the mass of the outer satellite to that of the planet.

At fixed k, the system is constrained to move along level curves of $\mathcal{H}$. At the maximum value of $\mathcal{H}$, denoted $\mathcal{H}_0$, $\phi = 0$. Corresponding to $\mathcal{H}_0$, there exists a nested set of periodic orbits for which conjunctions occur at periapse passage; $\varpi = \lambda'$ when $\lambda = \lambda'$. Orbital eccentricities, e_0, increase with proximity of n to the exact resonance value, $n_r = [(j+1)n - \dot{\varpi}_{\rm sec}]/j$, according to[3]

$$e_0 = \frac{\beta\mu'}{j(n - n_r)} \,. \tag{3.3}$$

Setting $\phi = 0$ in equation (3.1), we obtain a relation between e_0 and k. Comparing this relation with that given by equation (3.3), we observe that k increases with proximity to exact resonance although not at all linearly. The topology of the level curves of $\mathcal{H}$ undergoes a qualitative change across

$$k_{\rm crit} = \frac{3^{4/3}}{2} \left(j\beta\mu'\right)^{2/3} \,. \tag{3.4}$$

For $k < k_{\rm crit}$ there is one stable fixed point at $\phi = 0$ and $\mathcal{H} = \mathcal{H}_0$ whereas two additional fixed points, one stable and the other unstable, are present for $k > k_{\rm crit}$. Both additional fixed points are located at $\phi = \pi$, but $\mathcal{H}(\phi, e^2)$ has a local minimum at the former, which we denote by $\mathcal{H}_\pi$, and a saddle point at the latter.[4] A second set of nested periodic orbits corresponds to $\mathcal{H}_\pi$. These are pertinent to our investigation. They lie beyond exact resonance, $n < n_r$, and since $\phi = \pi$, conjunction coincides with apoapse passage. Thus for $k > k_{\rm crit}$, there is a door leading to escape from resonance. Librational overstability leading to passage through the inner separatrix is the way

---

[2] Here n' is the outer satellites mean motion and E and L are the orbital energy and angular momentum per unit mass of the inner satellite.

[3] $\dot{\varpi}_{\rm sec}$ is the contribution from secular terms to the rate of precession.

[4] For $k > k_{\rm crit}$, the additional fixed points bifurcate from the inflection point at $k = k_{\rm crit}$.

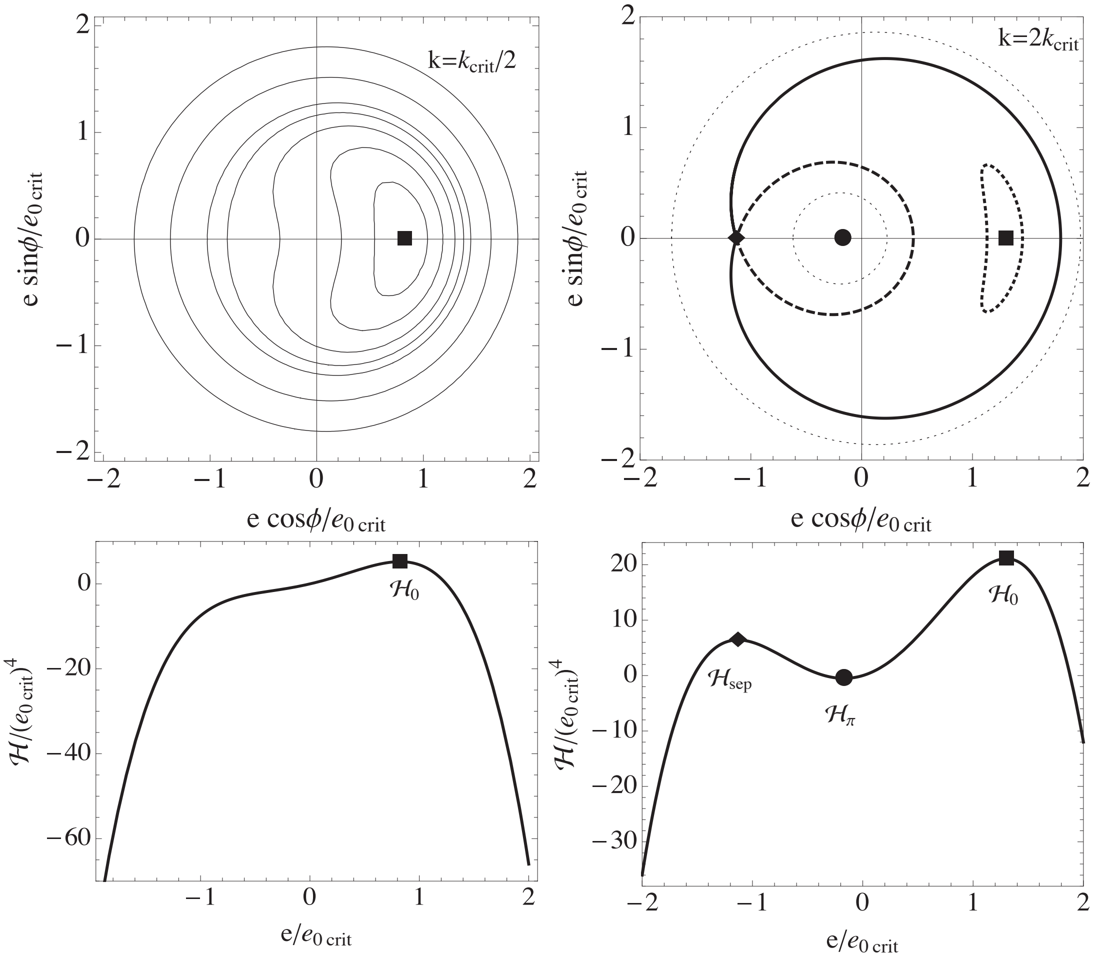

Figure 3.1 Contour plots of the Hamiltonian (top) and the corresponding cross section along the $\sin\phi = 0$ axis (bottom) for $k/k_{\rm crit} = 0.5$ (left) and $k/k_{\rm crit} = 2.0$ (right). Negative values on the bottom x-axes correspond to $\phi = \pi$. Stable fixed points are marked by a square at $\phi = 0, \mathcal{H}_0$ and a circle at $\phi = \pi, \mathcal{H}_\pi$. A diamond is attached to the unstable fixed point at the intersection of the inner (thick-dashed) and outer (thick-solid) branches of the separatrix.

to open it. Again, eccentricity increases with proximity to exact resonance;

$$e_\pi = \frac{\beta\mu'}{j(n_r - n)}\,. \tag{3.5}$$

3.2.1 Tidal evolution

We consider systems in which the planet's spin frequency $\omega > n$. Then tides the satellites raise in the planet produce positive torques that cause their orbits to expand.[5] We denote the tidal timescale for orbit expansion by $\tau_n \equiv -n/\dot{n}_{\rm T}$. From Peale (1999),

$$\tau_n = \frac{2}{9}\frac{M_p}{m}\left(\frac{a}{R_p}\right)^5 \frac{Q_p}{k_{2_p} n}\,, \tag{3.6}$$

---

[5] Here we no longer treat the inner satellite as a test particle.

where the subscript ‘p’ labels the planet. To ensure convergent migration, we further assume that $\tau_{n'} > \tau_n$.[6] We take the inner satellite's spin to be synchronous with its mean motion. Thus tides raised by the planet in the satellite dissipate energy at constant angular momentum. We denote the timescales for eccentricity damping by $\tau_e \equiv -e/\dot{e}_{\rm T}$.[7] Again from Peale (1999) we have,

$$\tau_e = \frac{2}{21}\frac{m}{M_p}\left(\frac{a}{R}\right)^5 \frac{Q}{k_2 n}\,. \tag{3.7}$$

It is important to bear in mind that τ_n and τ_e set the timescales for tidal evolution of n and e for an isolated satellite. Within a MMR, the resonant transfer of angular momentum and energy between satellites modifies these timescales.

Tides cause both k and $\mathcal{H}$ to evolve. Tidal evolution is slow in comparison to the periods characteristic of motions around the level curves of $\mathcal{H}$. The evolution of k and $\mathcal{H}$ are governed by

$$\frac{dk}{dt} = j\left(\frac{1}{\tau_n} - \frac{1}{\tau_{n'}} - 3(j+1)\frac{e^2}{\tau_e}\right)\,. \tag{3.8}$$

and

$$\frac{d\mathcal{H}}{dt} = \frac{dk}{dt}e^2 - 2k\frac{e^2}{\tau_e} + 3j^2\frac{e^4}{\tau_e} - \frac{2\beta\mu' e\cos\phi}{\tau_e}\,. \tag{3.9}$$

In practice, the slow tidal evolution of k and $\mathcal{H}$ is evaluated by averaging the right hand sides of equations (3.8) and (3.9) over a period of the motion around the level curves of $\mathcal{H}$ with k and $\mathcal{H}$ held fixed.

From equation (3.8), we see that $dk/dt = 0$ at $e = e_{\rm eq}$, where

$$e_{\rm eq}^2 = \frac{\tau_e(\tau_{n'} - \tau_n)}{3(j+1)\tau_n\tau_{n'}}\,. \tag{3.10}$$

Thus k increases almost linearly with time until it approaches $k_{\rm eq}$ where $e = e_{\rm eq}$. If $k_{\rm eq} \leq k_{\rm crit}$ the system cannot escape from MMR. On the other hand, if $k_{\rm eq} > k_{\rm crit}$, librational instability will ensue leading to passage through the inner branch of the separatrix and approach to the stable fixed point that lies within it (cf. Fig. 3.1). This transition signifies escape from the MMR and occurs on timescale τ_e.

Energy dissipated by damping orbital eccentricity is deposited as heat inside the inner satellite at a rate

$$P = \frac{m(nae)^2}{\tau_e}\,. \tag{3.11}$$

Substituting $e_{\rm eq}$ given by equation (3.10) into equation (3.11) sets a τ_e independent upper bound on the tidal heating rate;

$$P_{\rm max_2} = \frac{m(na)^2(\tau_{n'} - \tau_n)}{3(j+1)\tau_n\tau_{n'}}\,. \tag{3.12}$$

Evolution of $\mathcal{H}$ also deserves examination. From equation (3.9), it is obvious that convergent migration acts to increase $\mathcal{H}$ whereas eccentricity damping decreases it. A stronger result is that convergent migration drives $\mathcal{H}$ towards $\mathcal{H}_0$ even as it causes $\mathcal{H}_0$ to grow. This result may be derived by noting that, in the absence of eccentricity damping, the area within a level curve describing librations about $\mathcal{H}_0$ is an adiabatic invariant under convergent migration(Goldreich & Schlichting, 2014). Librations around $\mathcal{H}_0$ and $\mathcal{H}_\pi$ are analogous to anticyclones and cyclones in which Coriolis and pressure forces are in stable balance around pressure maxima and minima. Librational overstability promoted by eccentricity damping is analogous to the spreading and weakening of an anticyclone by friction.

We classify the MMRs of satellite pairs in the solar system into two groups, one with $k < k_{\rm crit}$

---

[6] This assumption is plausible because $\tau_n \propto m^{-1}n^{-13/3}$. Given the masses and orbits of solar system satellites involved in MMRs, it would be valid provided the tidal $Q's$ of Jupiter and Saturn are independent of tidal frequency.

[7] We neglect the effect that tides raised by the satellite in the planet have on e.

Table 3.1. Satellite pairs in MMR

	Argument	Satellites	k
1	$2\lambda' - \lambda - \varpi$	Io-Europa	$< k_{\rm crit}$
2	$2\lambda' - \lambda - \varpi'$	Io-Europa	$< k_{\rm crit}$
3	$2\lambda' - \lambda - \varpi$	Europa-Ganymede	$< k_{\rm crit}$
4	$4\lambda' - 2\lambda - \Omega - \Omega'$	Mimas-Tethys	$\gg k_{\rm crit}$
5	$2\lambda' - \lambda - \varpi$	Enceladus-Dione	$< k_{\rm crit}$
6	$4\lambda' - 3\lambda - \varpi'$	Titan-Hyperion	$> k_{\rm crit}$

Note. — The names of the satellites are ordered as 'inner satellite-outer satellite'. The concepts of k and $k_{\rm crit}$ are the same for all MMRs although their specific definitions vary. For the 1st, 3rd and 5th MMR, k and $k_{\rm crit}$ follow the formulas in Goldreich & Schlichting (2014). Expressions for k and $k_{\rm crit}$ appropriate to the 2nd, 4th and 6th MMR are provided in the appendix. The ϖ' in the arguments for the 2nd and 6th MMRs imply that the outer body's eccentricity is excited.

and the other with $k > k_{\rm crit}$ (Table 3.1). We emphasize the distinguishing features of the members in each group and investigate their origin.

3.3 Group I: $k < k_{\rm crit}$

All MMRs with $k < k_{\rm crit}$ are first order eccentricity-type and exhibit only small librations about $\mathcal{H} = \mathcal{H}_0$. The 1st, 2nd and 3rd entries in Table (3.1) involve pairs Jupiter's Galilean satellites. Each of these satellites is also a member of the Laplace 3-body resonance. The 2nd entry is special in that it is the outer body's eccentricity that is perturbed. The 4th entry is the only MMR in Saturn's satellite system for which $k < k_{\rm crit}$.

Ideally, Table (3.1) would have a 4th column displaying calculated values for $e_{\rm eq}$. Unfortunately, there are too many uncertain parameters to make calculating $e_{\rm eq}$ a useful exercise. Values of the tidal Love number, k_2, and the tidal quality factor, Q for both the planet and the perturbed satellite enter into equation (3.10) for $e_{\rm eq}$. Jupiter and Saturn are fluid bodies and reasonable estimates of their tidal Love numbers exist (Gavrilov & Zharkov, 1977). Reliable estimates for tidal Love numbers of solid satellites are also possible, but there is compelling evidence that, as a result of tidal heating, Io, Europa, and Enceladus have undergone limited internal melting.[8] Melting enhances k_2, but without knowing its extent, we cannot determine by how much. Our ability to estimate tidal Q's is poor. The mechanism responsible for tidal dissipation in Jupiter and Saturn remains a topic of active investigation (Ogilvie, 2014). In the past, estimates for the Q of Jupiter and Saturn were made by assuming that the satellites formed contemporaneously with their planet and that the MMRs resulted from tidal evolution (Goldreich, 1965; Goldreich & Soter, 1966). Recent astrometric analyses of the secular accelerations of Jupiter's Galilean satellites are consistent with these assumptions but those for Saturn's inner satellites imply that the satellites are younger than the planet (Lainey et al., 2009, 2012). Estimates of tidal Q for solid material are also fraught with uncertainty as relevant parameters such as composition, porosity, grain size and temperature are poorly constrained.

An upper bound to the current time-average rate of dissipation within Io, Europa and Ganymede is set by assuming the 2-body MMRs between Io-Europa and Europa-Ganymede have existed for t_{ss}, the entire age of the solar system (Goldreich & Mitchell, 2010)[9]

$$P_{\max_3} = \frac{2^{1/3} G M_J}{26 a_1 t_{\rm ss}} \left(m_2 + \frac{3}{2^{2/3}} m_3 \right) \approx 3 \times 10^{13}\,{\rm W}\,. \tag{3.13}$$

---

[8] Evidence comes from volcanoes on Io, magnetic induction by Europa, and geysers on Enceladus.

[9] Quantities pertaining to Io, Europa and Ganymede carry subscripts 1,2, and 3, respectively.

But infrared measurements made by the Galileo orbiter find Io's net luminosity to be closer to 10^{14} W (Veeder et al., 2012). This suggests that the tidal power dissipated in Io varies and thus its orbital eccentricity also does (Ojakangas & Stevenson, 1986).[10] How large might Io's eccentricity have been and could it ever have exceeded $e_{0\mathrm{crit}}$? Models by Ojakangas & Stevenson (1986) suggest not since the most extreme eccentricity they reach is $\approx 3e_{\mathrm{now}}$. According to Lainey et al. (2009), currently Io's semi-major axis is decreasing as might be expected if the satellite's orbital eccentricity were damping following an episode of higher than average tidal heating. Tides raised in synchronously spinning satellites convert orbital energy into heat at fixed angular momentum and hence cause a to decrease.

Next we examine the MMR between Enceladus and Dione. All the tidal heating occurs in Enceladus so we appeal to equations (3.11) and (3.12) for guidance. Infrared observations from the Cassini orbiter indicate that between $5-16\,\mathrm{GW}$ of power is being radiated from hot spots associated with long cracks in the south polar region of Enceladus (Spencer et al., 2013). Even the lower limit of this range is considerably greater than $P_{\mathrm{max}_2} = 1.2\,\mathrm{GW}$ derived from equation (3.12) with $Q_S = 18000$ from Meyer & Wisdom (2007). However, the lower bound of $Q_S = 18000$ is a fiction because its derivation involves a number of questionable assumptions, namely that Q_S is independent of time, tidal frequency, and tidal amplitude. Even more troubling is that it neglects the effects of Mimas's current and past MMRs with more massive outer satellites. Accounting for these decreases the lower bound on Q_S below 18000.[11] Finally, the biggest issue of all raised by Lainey et al. (2012) is whether Mimas is as old as Saturn.

3.3.1 Similarities and differences between Io and Enceladus

Io and Enceladus each exhibit unmistakable signatures of thermal activity. Moreover, currently the heat loss from each appears to exceed the maximum time averaged power attributable to the tidal torques acting on them, at least if the satellite is as old as its parent planet. Here we apply equation (3.11) to determine the value of τ_e required for tidal dissipation inside each satellite to equal its current power output. Then we compare that value to calculations of τ_e based on models for each satellite.

For Io to dissipate $10^5\,\mathrm{GW}$ with $e = 0.0041$ requires $\tau_e = 1.5\times 10^5\,\mathrm{y}$. A uniform density model with $\mu = 10^{11}\,\mathrm{dyne\,cm^{-2}}$ yields $\tau_e = 7\times 10^4\,Q_{\mathrm{Io}}\,\mathrm{y}$. Thus it is not a stretch to imagine that with e enhanced by a factor of 3, tidal dissipation in Io could match the satellite's current net luminosity.

For Enceladus to dissipate $5\,\mathrm{GW}$ with $e = 0.0047$ requires $\tau_e = 2.5\times 10^6\,\mathrm{y}$. Our models for Enceladus are all spherically symmetric and contain a rigid core with $\rho = 3\,\mathrm{g\,cm^{-3}}$. The core is encased in a layer of water with $\rho = 1\,\mathrm{g\,cm^{-3}}$ overlain by a shell of ice with $\rho = 0.93\,\mathrm{g\,cm^{-3}}$ and $\mu = 4\times 10^{10}\,\mathrm{dyne\,cm^{-2}}$. Absent an ocean, we calculate $\tau_e = 8.2\times 10^7 Q_{\mathrm{En}}\,\mathrm{y}$. So tidal dissipation in a solid model falls far short of matching Enceladus's current net luminosity. Models with thin ice shells overlying thick oceans can do better. For example, a model with an ice shell 30 km thick as estimated by Iess et al. (2014) yields $\tau_e = 1.2\times 10^6\,Q_{\mathrm{En}}\,\mathrm{y}$. An enhancement of e by a factor of 3 and a $Q_{\mathrm{En}} = 20$ would be a possible fit. Note however that the enhanced e would make $e > e_{0_{\mathrm{crit}}}$.

3.4 Group II: $k > k_{\mathrm{crit}}$

The Mimas-Tethys 4:2 II' MMR and the Titan-Hyperion 4:3 e' MMR are the only ones for which $k > k_{\mathrm{crit}}$. Unlike the MMRs with $k < k_{\mathrm{crit}}$, their resonant arguments exhibit large librations. Could this be a sign that they are experiencing librational overstability as described in section 3.2.1? Below we argue that these librations are merely fossils and do not arise from overstability. We bolster this claim by demonstrating that neither the inclination of Mimas nor the eccentricity of Hyperion has suffered significant damping during the lifetimes of their respective MMRs.

---

[10] Tidal heating rate is $\propto e^2/\tau_e$.

[11] Although it is not possible to reconstruct the history of Mimas's orbital expansion, by considering potential first-order MMRs we find that Q_S might be as low as 6000.

Table 3.2. Eccentricity Comparison

Satellites	$e_{\rm now}$	$e_{0\rm crit}$	$e_{0\rm crit}/e_{\rm now}$
Io-Europa (e)	0.0041	0.037	9.024
Io-Europa (e')	0.009	0.0238	2.532
Europa-Ganymede	0.009	0.0538	48.91
Enceladus-Dione	0.0047	0.0157	3.340

Note. — Comparison of the current and critical values of e. Io-Europa (e') signifies that this row shows the corresponding values for e'.

3.4.1 Mimas-Tethys

At present, Mimas and Tethys occupy a 4 : 2 mixed-inclination MMR. The leading resonant term in the disturbing function has coefficient $\propto II'\cos\phi$ with inclination I measured relative to the Saturn's equator plane. The resonant argument $\phi = 4\lambda' - 2\lambda - \Omega - \Omega'$ with Ω the longitude of the ascending node. Currently, ϕ is librating around zero with $\phi_{\rm max} \simeq 97°$ (Seidelmann, 1992). Lowest-order inclination MMRs are of 2nd order because inclinations enter the mutual distance between two satellites as $\cos(I - I') \sim 1 - (I)^2/2 - (I')^2/2 - II'$.

Tethys is significantly more massive than Mimas, $m/m' \simeq 0.06$, and their orbital inclinations are similar, $I \simeq 1.57°$ and $I' \simeq 1.11°$ (Seidelmann, 1992). In Appendix 3.5.3, we demonstrate that

$$\left(\frac{dI'^2}{dt}\right)_r \simeq \left(\frac{m}{m'}\right)\left(\frac{dI^2}{dt}\right)_r , \tag{3.14}$$

where 'r' denotes resonance. Thus it seems likely that Tethys's inclination originates from passage through some other MMR, e.g., Tethys-Dione 4:6 inclination-type MMR. A similar hypothesis has been investigated for the origin of the anomalously large inclination of the Uranian satellite Miranda (Malhotra & Dermott, 1990), Tittemore & Wisdom (1990).

The dynamics of the Mimas-Tethys mixed-inclination 4:2 MMR is entirely analogous to that of the eccentricity-type resonance discussed in 3.2. With the replacement of $e/e_{0_{\rm crit}}$ by $I/I_{0\rm crit}$ where $I_{0_{\rm crit}}$ = is defined in equation (3.36), Figure 3.1 applies equally well to this resonance. Moreover, since $k \gg k_{\rm crit}$, inclination damping excites overstable librations on timescale $\tau_I \equiv -I/\dot{I}_{\rm T}$, where $I_{\rm T}$ is the tidal damping rate of I.

It is imperative that we evaluate τ_I. To do so we need to understand the relation between three unit vectors, those along the spin of Mimas, $\hat{\mathbf{s}}$, the spin of Saturn, $\hat{\mathbf{S}}$, and the orbital angular momentum of Mimas, $\hat{\mathbf{L}}$. Tidal friction drives $\hat{\mathbf{s}}$ to a Cassini state on a timescale comparable to that over which it causes the satellite to spin synchronously with its mean motion (Colombo, 1966; Ward, 1975), a mere instant relative to the age of the solar system. In a Cassini state, the three unit vectors defined above lie in a plane. In addition to the orbital inclination, $I = \cos^{-1}\hat{\mathbf{L}}\cdot\hat{\mathbf{S}}$, the state is defined by the obliquity, the angle between the satellite's spin and its orbit normal, $\epsilon = \cos^{-1}\hat{\mathbf{s}}\cdot\hat{\mathbf{L}}$. For small values of I and ϵ, the ratio of these angles (Colombo, 1966)

$$\frac{\epsilon}{I} \approx -\frac{\dot{\Omega}}{\omega} . \tag{3.15}$$

In the above, $\dot{\Omega}$ is the rate of nodal precession on the planet's equator plane. It mainly arises from the planet's oblateness (Murray & Dermott, 1999),

$$\dot{\Omega} \approx \dot{\Omega}_{J_2} \approx -\frac{3}{2}J_{2,S}\left(\frac{R_S}{a}\right)^2 n , \tag{3.16}$$

where $J_{2,S} \simeq 0.016$ and $R_S \simeq 6 \times 10^4\,$km are Saturn's quadrupole coefficient and radius, and $n \simeq$

and $a \simeq 1.8 \times 10^5\,\mathrm{km}$ are Mimas's orbital mean motion and semi-major axis (Seidelmann, 1992). Also, ω is the rate that the spin axis of Mimas would precess about the orbit normal if the later maintained a fixed orientation in inertial space (Ward, 1975);

$$\omega \approx \frac{3}{2}\left(\frac{2C-B-A}{2C}\right)n\,, \tag{3.17}$$

where $C \geq B \geq A$ are the principal moments of inertia of Mimas. Mimas is tidally stretched along the axis joining it to Saturn and flattened by its spin. Its low mean density, $\bar{\rho} = 1.148\,\mathrm{g\,cm^{-3}}$ implies a small rocky core that contributes little to its mass and less to its polar moment of inertia. Thus in estimating its principal moments of inertial, it is reasonable to approximate Mimas by a body of uniform density. It is more questionable whether a body of its size has relaxed to near hydrostatic equilibrium. Making these two assumptions, it is a straightforward exercise to derive the relations

$$\frac{2C-B-A}{2C} = \frac{25}{8}\frac{M_S}{m}\left(\frac{R}{a}\right)^3 = 0.058\,, \tag{3.18}$$

and

$$\frac{B-A}{C} = \frac{15}{4}\frac{M_S}{m}\left(\frac{R}{a}\right)^3 = 0.069\,. \tag{3.19}$$

Substituting equations (3.18) and (3.19) into equation (3.15), we arrive at

$$\frac{\epsilon}{I} \simeq 0.029\,, \tag{3.20}$$

which implies $\epsilon \approx 0.045^\circ$ given $I = 1.57^\circ$ (Seidelmann, 1992). Thus it appears that the spin of Mimas is closely aligned with the normal to its orbit. Probably this explains why astrometry has been unable to determine the obliquity, ϵ, although it has revealed an amplitude of 0.84° for Mimas's physical libration from which $(B-A)/C \simeq 0.09$ has been determined (Tajeddine et al., 2014). As a sanity check we can compare this value with 0.069 predicted by equation (3.19). The agreement is satisfactory although we note that according to Tajeddine et al. (2014), the difference between a more accurate model calculation for $(B-A)/C$ and the value deduced from the physical libration hints that Mimas may have an ocean that comes within 30 km of its surface and reduces C by decoupling the interior from the external icy shell.

Next we consider tides raised on Mimas by Saturn. Absent dissipation, the tidal bulge would peak at the sub-Saturn point and the point diametrically opposite to it. Because Mimas has a finite obliquity, the tidal bulge oscillates across the equator at frequency n. Time varying strains dissipate energy and as a result damp orbital inclination on timescale τ_I where

$$\frac{1}{\tau_I} \approx \frac{21}{2}\left(\frac{\epsilon}{I}\right)^2\left(\frac{M_S}{m}\right)\left(\frac{R}{a}\right)^5\frac{k_2}{Q}n\,. \tag{3.21}$$

In the above, we have simply multiplied the standard expression for $1/\tau_e$ by the small quantity $(\epsilon/I)^2$. Thus it should come as no surprise that for any reasonable choice of parameters, τ_I exceeds 4.6 Gy, the age of the solar system. Consequently, although $k \gg k_{\mathrm{crit}}$, the libration of ϕ is not due to overstability. Sinclair (1972) attributes it to the evolution of the initial I following capture as Mimas evolved deeper into resonance. We agree. Sinclair also estimated a capture probability of $\approx 4\%$ for the whereas employing more modern methods (Borderies & Goldreich, 1984), we find 6% with capture taking place at $k \approx 20k_{\mathrm{crit}}$ when $I = 0.35^\circ$.

3.4.2 Titan-Hyperion

Titan and Hyperion are partners in a 4:3 eccentricity-type MMR with resonant argument $\phi = 4\lambda' - 3\lambda - \varpi'$. Thus it is Hyperion's orbital eccentricity that is affected by the resonance. Titan is the most massive of Saturn's satellites and Hyperion the least massive of the satellites included in

Table 3.1. Titan's semi-major axis is so large that tides do not currently play any role in driving the expansion of its orbit. Speculations about the origin of the Titan-Hyperion MMR are the best that have been offered so far (Peale, 1978). We have nothing better other than to suggest that the MMR formed as the result of convergent migration at the time the satellites were embedded in their natal disk. Tidal damping of Hyperion's orbital eccentricity is utterly negligible so currently the librations of the resonant angle, ϕ, are neither growing nor decaying. But if disk interactions were responsible for the formation of the resonance, eccentricity damping at that time might have driven overstable librations.

3.5 Discussion

3.5.1 Torque comparison

Lainey et al. (2012) analyze more than a century of astrometric data to determine the orbital evolution of Saturn's major satellites. They reach two surprising conclusions. The first is that Saturn's tidal Q is about an order of magnitude smaller than previously thought and that implies the inner satellites are younger than the planet. The second is that the orbit of Mimas is shrinking at a great rate. We are sympathetic to the first conclusion but find it difficult to believe that the second is correct. Below we speculate about how an otherwise impressive investigation might have slipped up on this particular point.

According to equation (3.26), the evolution of Mimas's mean motion should satisfy,

$$\frac{\dot{n}}{n} = -6 f_{62} n s s' \alpha \mu' \sin\phi - \frac{1}{\tau_n} \, . \tag{3.22}$$

where the first and second terms on the rhs arise from the resonant torque by Tethys and tidal torque from Saturn. The argument, ϕ, librates between -97° and 97° with period ≈ 74 years. At a time when $\phi = \pi/2$, the torque from Tethys exceeds that from Saturn by a factor $4.6 \times 10^8/Q_S \approx 2.7 \times 10^5$ where the value $Q_S = 1700$ obtained by Lainey et al. (2012) has been adopted to obtain the final expression. Over a time span $\gg 74\,\mathrm{y}$, the time-average $\dot{n}$ is positive and controlled by Saturn's tidal torque. However, the time span of the data in Lainey et al. (2012) is only slightly above a century. Thus the $\dot{n}/n$ they deduced, $(2.2 \pm 0.61) \times 10^{-16}\,\mathrm{s}^{-1}$, might have been corrupted by Tethys's torque.

Enceladus's mean motion is similarly affected by the torque from Dione. For this MMR, ϕ librates between -1.5° and 1.5° with a period of $\approx 11.5\,\mathrm{y}$;

$$\frac{\dot{n}}{n} = 3\beta\mu' e n \sin\phi - \frac{1}{\tau_n} + \frac{3e^2}{\tau_e} \, . \tag{3.23}$$

The effect of eccentricity damping on $\dot{n}/n$ is an extra complication. Neglecting this, we find the ratio of the maximum resonant torque from Dione to the tidal torque to be $1.2 \times 10^8/Q_S \approx 7.2 \times 10^4$ for $Q_S = 1700$. However, in this case the libration period is much shorter than the time spanned by the astrometric data in Lainey et al. (2012) so determination of $\dot{n}/n$ for Enceladus may not be adversely influenced by the torque from Dione.

3.5.2 Vestiges of MMRs Past

It is likely that the orbits of some satellites exhibit traces of their participation in extinct MMRs.

Mimas's orbital eccentricity, $e_M \approx 0.02$, is a prime examples (Seidelmann, 1992). It might result from the past participation by Mimas in a 3 : 1 MMR with Dione. For $k > k_{\mathrm{crit}}$, there is a door leading to passage through the MMR and librational instability due to eccentricity damping can open it. As already mentioned in section 3.4, the inclination of Tethys might have been excited by the Tethys-Dione 4:6 inclination-type MMR.

MMRs that excite eccentricity result in tidal heating that may cause internal melting. Thermal activity of Io and Europa are outstanding examples of tidal heating in current resonances. It is less

Table 3.3. Parameters

Satellite	$m\,(\mathrm{g})$	$R\,(\mathrm{km})$	$n\,(\mathrm{rad\,s^{-1}})$	$g\,(\mathrm{cm\,s^{-2}})$	$\rho\,(\mathrm{g\,cm^{-3}})$	$\tilde{\mu}$	Type
Mimas	3.7×10^{22}	198	7.7×10^{-5}	6.4	1.14	2700	Icy
Enceladus	1.1×10^{23}	252	5.3×10^{-5}	11.4	1.6	2000	Icy
Tethys	6.2×10^{23}	531	3.85×10^{-5}	14.7	0.984	500	Icy
Dione	1.1×10^{24}	561	2.65×10^{-5}	23.3	1.48	200	Icy
Titan	1.3×10^{26}	2576	4.56×10^{-6}	135.2	1.88	9	rocky/icy
Hyperion	5.6×10^{21}	135	3.42×10^{-6}	2	0.544	2.6×10^{4}	icy
Io	8.9×10^{25}	1822	4.1×10^{-5}	179.6	3.53	40	rocky
Europa	4.8×10^{25}	1561	2.0×10^{-5}	131.4	3.01	80	rocky
Ganymede	1.5×10^{26}	2634	1.0×10^{-5}	142.8	1.94	8	rocky/icy

Note. — To calculate $\tilde{\mu} \equiv 19\mu_r/(2\rho g R)$, we apply $\mu_r \simeq 4 \times 10^{10}\,\mathrm{dyn\,cm^{-2}}$ for icy satellite, $\mu_r \simeq 6 \times 10^{10}\,\mathrm{dyn\,cm^{-2}}$ for rocky/icy satellite, and $\mu_r \simeq 5 \times 10^{11}\,\mathrm{dyn\,cm^{-2}}$ for rocky satellite. For Saturn, we adopt $Q_S \simeq 10^4$, $M_S \simeq 5.7 \times 10^{29}\mathrm{g}$ and $R_S \simeq 6 \times 10^4\,\mathrm{km}$. For Jupiter, we adopt $Q_J \simeq 10^5$, $M_J \simeq 1.9 \times 10^{30}\mathrm{g}$, and $R_J \simeq 7 \times 10^4\,\mathrm{km}$. All parameters except $\tilde{\mu}$ and Q of the planets are taken from Seidelmann (1992). Jupiter's Q, Q_J, is usually believed to be $10^5 \sim 10^6$ (e.g., Greenberg et al. (2008), Wu (2005), and references therein). We adopt $Q_J \simeq 10^5$. Saturn's Q, Q_S, was believed to be beyond 10^4 (Meyer & Wisdom, 2007), but recent observations of Saturnian satellites' orbital evolutions indicate Q_S is only a few thousands (**?**). We adopt $Q_S \simeq 10^4$. The Love number of Saturn, $k_{2,S} \simeq 0.34$ (**?**), and Jupiter's Love number is $k_{2,J} \simeq 0.38$ (Gavrilov & Zharkov, 1977).

certain but plausible that Mimas has an internal ocean that reduces the apparent polar moment of inertia as deduced from the amplitude of its physical libration (Tajeddine et al., 2014). This could be a consequence of its involvement with the MMRs mentioned above as candidates for exciting its orbital eccentricity.

If the expansion rates for the orbits of Saturn's satellites determined by Lainey et al. (2012) are correct, the frequency at which satellites entered and escaped from MMRs must have been much greater than previously imagined. Maximum rates of tidal heating associated with eccentricity-type MMRs would also have been greatly enhanced. Thus more satellites are likely to possess internal oceans.

Consider the putative ocean of Mimas. Tajeddine et al. (2014) estimate that its surface lies below $d \approx 30\,\mathrm{km}$ of ice. Given the thermal diffusivity of ice, $\kappa \approx 0.01\,\mathrm{cm^2\,s^{-1}}$, an ocean of this depth would retreat after $\delta t \approx 3 \times 10^7\,\mathrm{y}$. We also estimate the timescale for eccentricity damping, $\tau_e \approx 50(Q/100)\,\mathrm{My}$, from a model of Mimas consisting of an ocean sandwiched between a core with $\rho = 3\,\mathrm{g\,cm^{-3}}$ and an ice shell of thickness 30 km chosen to match the mean density $\overline{\rho} = 1.145\,\mathrm{g\,cm^{-3}}$. Based on an assumed $Q_S = 18000$, Meyer & Wisdom (2008) calculate that Mimas escaped from the 3:1 resonance with Dione about 700 My ago. The much lower Q_S proposed by Lainey et al. (2012) is more compatible with the survival of an ocean in Mimas.

There is an alternate scenario for the unexpectedly large physical libration of Mimas that does not involve an internal ocean. It postulates that Mimas has a nonhydrostatic shape which enhances $(B - A)/C$ above its hydrostatic value (Tajeddine et al., 2014). We estimate $\tau_e \approx 1\,\mathrm{Gy}(Q/100)$ for a solid Mimas, a value consistent with the persistence of Mimas's orbital eccentricity even with the traditional value of Q_S.

Appendix

Satellite parameters

3.5.3 Mimas-Tethys MMR

Disturbing functions for the Mimas-Tethys 4:2 mixed II' MMR read

$$\mathcal{R} = f_{62}(na)^2 \alpha s s' \mu' \cos\phi\,, \tag{3.24}$$

$$\mathcal{R}' = f_{62}(n'a')^2 s s' \mu \cos\phi\,, \tag{3.25}$$

with $\phi = 4\lambda' - 2\lambda - \Omega - \Omega'$ the resonant argument and $f_{62} < 0$ a numerical coefficient (Murray & Dermott, 1999). Other symbols follow conventional definitions, λ is mean longitude, Ω is longitude of the ascending node, n is mean motion, a is semi-major axis, $s \equiv \sin(I/2)$ where I is inclination, $\mu \equiv m/M_p$ is the mass ratio between satellite and planet, and $\alpha \equiv a/a'$. Equations governing the evolution of the orbital elements take the form

$$\frac{\dot{n}}{n} = -6 f_{62} n s s' \alpha \mu' \sin\phi - \frac{1}{\tau_n} + \frac{p s^2}{\tau_I}\,, \tag{3.26}$$

$$\frac{ds^2}{dt} = -\frac{1}{2} f_{62} n s s' \alpha \mu' \sin\phi - \frac{s^2}{3\tau_n} - \frac{2s^2}{\tau_I}\,, \tag{3.27}$$

$$\dot{\Omega} = f_{62} n \frac{s'}{4s} \alpha \mu' \cos\phi + \dot{\Omega}_{J_2}\,, \tag{3.28}$$

$$\frac{\dot{n}'}{n'} = 12 f_{62} n' s s' \mu \sin\phi - \frac{1}{\tau_{n'}} + \frac{p s'^2}{\tau_{I'}}\,, \tag{3.29}$$

$$\frac{ds'^2}{dt} = -\frac{1}{2} f_{62} n' s s' \mu \sin\phi - \frac{s'^2}{3\tau_{n'}} - \frac{2s'^2}{\tau_{I'}}\,, \tag{3.30}$$

$$\dot{\Omega}' = f_{62} n' \frac{s}{4s'} \mu \cos\phi + \dot{\Omega}'_{J_2}\,, \tag{3.31}$$

$\dot{\Omega}_{J_2}$ separates the different 4:2 inclination-type resonances sufficiently so that only terms in the disturbing function with argument ϕ defined above need to be considered in treating the II' MMR. Terms involving τ_n and $\tau_{n'}$ are due to the tides raised in Saturn by its satellites, Mimas or Tethys. Those terms involving τ_I and $\tau_{I'}$ are due to inclination damping by tides the planet raises in the satellites. Inclination damping conserves the component of each satellite's orbital angular momentum parallel to Saturn's spin while decreasing its orbital energy. Therefore, $\cos I/n^{1/3}$ =constant which establishes that $p = 12$ in equations (3.26) and (3.29).

We use lower index 'Res' to label the change rate due to the mean motion resonance. For example, $(ds^2/dt)_{\rm Res}$ refers to the first term on the right hand side of equation (3.27). Notice that $(\dot{n}'/n')_{\rm Res}$, $(ds'^2/dt)_{\rm Res}$ and $(\dot{\Omega}')_{\rm Res}$ are all smaller than their corresponding rates for the inner satellite by a factor $\sim (m/m') \ll 1$. Resonance dynamics mainly affects the inner body, and therefore we neglect $(\dot{n}'/n')_{\rm Res}$, $(ds'^2/dt)_{\rm Res}$ and $(\dot{\Omega}')_{\rm Res}$. Considering only resonance terms, we find

$$12\left(\frac{ds^2}{dt}\right)_{\rm Res} - \left(\frac{\dot{n}}{n}\right)_{\rm Res} = 0\,, \tag{3.32}$$

which yields a constant of motion in resonance dynamics,[12]

$$k \equiv 12 s^2 + \frac{f_{62}\mu'}{2^{11/3}} \frac{s'}{s} \cos\phi + \frac{\dot{\phi}}{4n'}\,, \tag{3.33}$$

where we have set $n/n' = 2$ and $\alpha = 2^{-2/3}$. A second constant of motion is the Hamiltonian

$$\mathcal{H} \equiv k s^2 - 6 s^4 + \frac{f_{62}\mu'}{2^{8/3}} s s' \cos\phi\,, \tag{3.34}$$

from which the equations of motion follow as $(\dot{\phi})_{\rm Res}/(4n') = \partial\mathcal{H}/\partial(s^2)$ and $(ds^2/dt)_{\rm Res}/(4n') = -\partial\mathcal{H}/\partial\phi$. Resonant dynamics in the phase space consists of motion along level curves of $\mathcal{H}$ whose geometry is determined by k. A qualitative change in topology occurs across a value k we denote by $k_{\rm crit}$;

$$k_{\rm crit} = \frac{3^{4/3}}{2^{22/9}} (-f_{62} s' \mu')^{2/3}\,. \tag{3.35}$$

---

[12] This constant arises because $4\lambda' - 2\lambda + \Omega + \Omega'$ is an ignorable coordinate.

Corresponding to $k_{\rm crit}$,

$$I_{0_{\rm crit}} = \frac{(-f_{62} I' \mu')^{1/3}}{2^{14/9} 3^{1/3}} \, . \tag{3.36}$$

Currently, $k/k_{\rm crit} \approx 424$ and $I/I_{\rm crit} \approx 18$.

1. For $k < k_{\rm crit}$, there exists one fixed point where both $\partial\mathcal{H}/\partial(s^2)$ and $\partial\mathcal{H}/\partial\phi$ vanish. $\mathcal{H}$ is maximal at this fixed point which is labeled by a filled square in the upper panel of Figure (3.1).
2. For $k > k_{\rm crit}$, two additional fixed points are present. As illustrated in the lower panel of Figure (3.1), the new fixed points are represented by a circle at the local minimum of $\mathcal{H}$ and a diamond at a saddle point. Fixed points at the maximum and local minimum are stable whereas that at the saddle point is unstable. A separatrix emanates from the saddle point. It has an outer branch shown by a thick solid line and an inner branch marked by a thick dashed line. Level curves are of three types: Libration orbits as shown by the banana-shaped thick dotted loop around the maximum of $\mathcal{H}$; External circulation orbits as shown by the outermost thin dotted circle; Internal circulation orbits as depicted by the small thin dotted circle surrounding the relative minimum of $\mathcal{H}$.

3.5.4 First-order e' MMRs

Expressions for k and $k_{\rm crit}$ have been defined in the main text for all but two of the MMRS listed in Table 3.1. The exceptions in the Io-Europa MMR with $\phi = 2\lambda' - \lambda - \varpi'$ and the Titan-Hyperion with $\phi = 4\lambda' - 3\lambda - \varpi'$. These share the feature that the outer satellite's orbit is perturbed and the inner satellite is the perturber. We treat the perturbed satellite as a test particle, which is a good approximation as long as $m' \ll m$. This is valid for Titan-Hyperion, but not for Io-Europa. But our discussion of Io-Europa is mainly conceptual so it does not depend sensitively on the accuracy of the approximation.

For the MMR involving Io and Europa with argument $2\lambda' - \lambda - \varpi'$,

$$k \simeq 3e'^2 + \frac{\mu}{2e'} \left(f_{31} - \frac{1}{2\alpha^2} \right) \cos\phi + \frac{\dot\phi}{n} \, , \tag{3.37}$$

where $\alpha = a/a' = (n/n')^{-2/3} \simeq 2^{-2/3}$ and $f_{31} \simeq 1.7$. The critical k,

$$k_{\rm crit} = \frac{3^{4/3}}{4} \left(2f_{31} - \frac{1}{\alpha^2} \right)^{2/3} \mu^{2/3} \tag{3.38}$$

and

$$e'_{\rm crit} = (2/3)^{1/3} \mu^{1/3} \left(f_{31} - \frac{1}{2\alpha^2} \right)^{1/3} \, . \tag{3.39}$$

For the MMR involving Titan and Hyperion with argument $\phi = 4\lambda' - 3\lambda - \varpi'$,

$$k = 6e'^2 + \frac{f_{31}\mu}{4e'_{\rm crit}} \cos\phi + \frac{dot\phi}{3n} \, . \tag{3.40}$$

where $f_{31} \simeq 0.825$ and the critical k is

$$k_{\rm crit} = \frac{3^{4/3}}{2^{5/3}} (f_{31}\mu)^{2/3} \, . \tag{3.41}$$

Chapter 4

Thermal Conductivity of Rubble Piles

4.1 Introduction

Observational evidence for rubble piles is varied. Mean densities, $\overline{\rho}$, below $1\,\mathrm{g\,cm^{-3}}$ are typical of Saturn's icy satellites with radii smaller than 140 km (Dougherty et al., 2009), indicating porosity throughout their entire bodies. Lunar seismometers detected strong scattering in the upper 20 km of the Moon implying the presence of fractures and voids (Heiken et al., 1991). The sharp decline in the number of asteroids with spin periods below $\sim 3\,\mathrm{h}$ demonstrates both their low mean densities, $\overline{\rho} \leq 2\,\mathrm{g\,cm^{-3}}$, and weak cohesion (Waszczak et al., 2015). Thermal responses of asteroids and satellites to time variations of the incident solar flux yield thermal inertias approximately two orders of magnitude smaller than those of monolithic materials (Delbo' & Tanga, 2009; Howett et al., 2010). The lunar surface is covered by a layer of regolith whose density in the top 3 m ranges between 1 to $2\,\mathrm{g\,cm^{-3}}$(Heiken et al., 1991) and thus below that of rock, $\rho \approx 3\,\mathrm{g\,cm^{-3}}$.

Goldreich & Sari (2009) studied the elastic behavior of rubble piles. They pointed out that voids rather than cracks are the essential difference between rubble piles and monoliths. We focus on the thermal properties of rubble piles, which have broad applications. In the fluid free environment pertinent to asteroids and satellites lacking atmospheres, voids impede heat transfer.

Our paper is organized as follows. In Section 4.2, we evaluate the condition for a rubble pile to survive and show that it is consistent with indications from observations. We derive an order-of-magnitude expression for the effective conductivity, and compare it to measurements of the thermal conductivity of the lunar regolith in Section 4.3. Section 4.4 presents a model for the thermal inertia of a rubble pile and tests it against observationally determined values for the Moon and the icy Saturnian satellites. **We conclude with a short discussion in Section 4.5.**

4.2 Conditions For Existence Of Rubble Piles

Consider a typical monolithic element composing a rubble pile.[1] Its surface is generally coarse, i.e., covered by nubs spanning a wide range of radii of curvature (Johnson, 1987). Contacts between neighboring elements typically involve nubs with the smallest radii of curvature, $\hat{r}$, that can survive strains generated by the weight of the overlying material. Smaller nubs are crushed and flattened. Figure (4.1) illustrates the geometry.

Although each element participates in several contacts, it suffices to focus on just one. As shown in Figure (4.1), the nub is compressed by $\delta\hat{r}$ resulting in contact area $s^2 \sim \hat{r}\delta\hat{r}$. Near contact, the maximum strain, $\epsilon_Y \sim \delta\hat{r}/s$, and stress, $\sigma \sim \mu\epsilon_Y$, concentrate in a volume $\sim s^3$ where ϵ_Y and μ denote yield strain and shear modulus, respectively.

---

[1] This section applies and extends aspects of the Hertz (1882) theory of contact between elastic bodies.

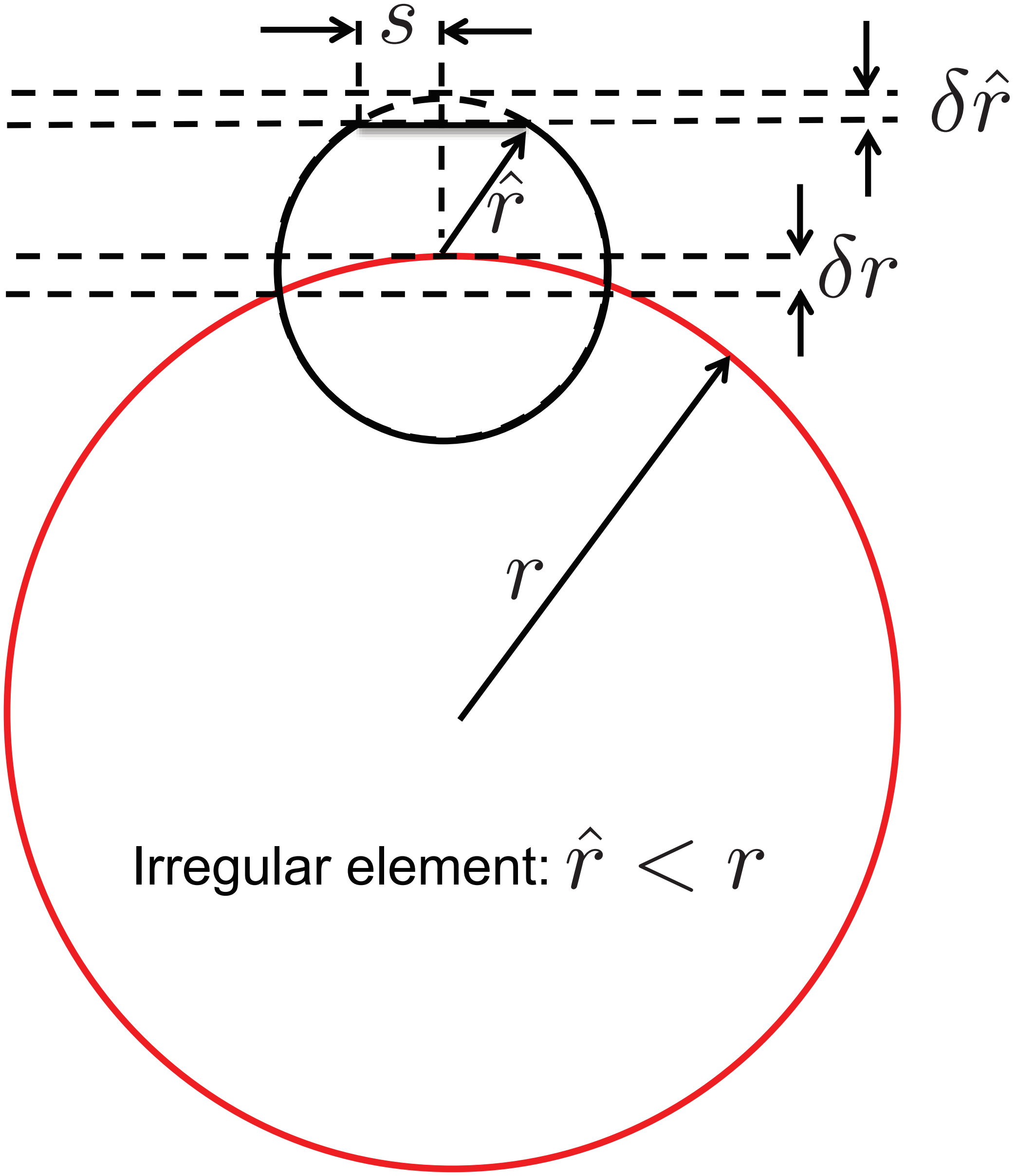

Figure 4.1 The geometry of a rough-surface element.

At average pressure P, each element must transmit force $\sim r^2 P$ across contact area $\sim s^2$. Combining the above relations, we obtain

$$\hat{r} \sim r\left(\frac{P}{\epsilon_Y^3 \mu}\right)^{1/2}, \tag{4.1}$$

$$s \sim r\left(\frac{P}{\epsilon_Y \mu}\right)^{1/2}, \tag{4.2}$$

$$\delta\hat{r} \sim r\left(\frac{\epsilon_Y P}{\mu}\right)^{1/2}, \tag{4.3}$$

which apply for both $\hat{r} < r$ and $\hat{r} > r$. At $P \sim \epsilon_Y^3 \mu$, $\hat{r} \sim r$. Above this pressure voids shrink leading the mean density to grow. At $P \sim \epsilon_Y \mu$, $s \sim r$, i.e., the strain reaches ϵ_Y throughout the element, voids close and the density approaches its monolithic value. We refer to $P < \epsilon_Y^3 \mu$ as the low-pressure regime and $\epsilon_Y^3 \mu < P < \epsilon_Y \mu$ as the high-pressure regime. Rubble piles do not exist at $P > \epsilon_Y \mu$.

The hydrostatic pressure at the center of a homogeneous sphere is $P_c = (2\pi/3) G \bar{\rho}^2 R^2$. Thus the low-pressure regime would apply throughout bodies with $R \leq R_*$;

$$R_* \sim \left(\frac{\mu \epsilon_Y^3}{G \bar{\rho}^2}\right)^{1/2} \sim 10 \left(\frac{\epsilon_Y}{0.01}\right)^{3/2} \text{km}, \tag{4.4}$$

whereas the limit of the high-pressure regime would be reached at the centers of bodies with $R_{\max}$;

$$R_{\max} \sim \left(\frac{\mu \epsilon_Y}{G \bar{\rho}^2}\right)^{1/2} \sim 10^3 \left(\frac{\epsilon_Y}{0.01}\right) \text{km}. \tag{4.5}$$

Values of R_* and $R_{\max}$ apply to bodies composed of either rock or ice; μ is about 10 times larger for rock than for ice, but ρ for ice is about 3 times smaller than that for rock.

Mean densities as small as half that of the monolithic density of their constituents would be restricted to $R < R_*$ although less substantial under-densities could persist up to $R = R_{\max}$. Rubble piles may exist in the upper layers of bodies larger than $R_{\max}$. Given surface gravity g, low-pressure and high-pressure regimes would extend to depths $d_* \approx \epsilon_Y^3 \mu/(\bar{\rho} g)$ and $d_{\max} \approx \epsilon_Y \mu/(\bar{\rho} g)$. Assuming $\epsilon_Y = 0.01$ and parameters appropriate to the Moon, $g \approx 160\,\text{cm}\,\text{s}^{-2}$, $\bar{\rho} \approx 3\,\text{g}\,\text{cm}^{-3}$, and $\mu \approx 5 \times 10^{11}\,\text{dyne}\,\text{cm}^{-2}$, we estimate $d_* \approx 10\,\text{m}$ and $d_{\max} \approx 100\,\text{km}$. Passive seismic experiments on the moon indicate that wave scattering is strongest in the upper 20 km (Heiken et al., 1991), presumably where fractures and voids are most abundant.

4.3 Effective Conductivity

4.3.1 Phonon Conductivity

Suppose the temperature drops by $\sim \Delta T$ across an element. In steady state, with uniform monolithic conductivity, k, and without heat sources or sinks, the temperature, T, satisfies $\nabla^2 T = 0$. Like the stress, the magnitude of the temperature gradient peaks in the vicinity of the contact. Away from the contact, the conductive flux and hence ∇T diminish roughly quadratically with distance implying $|\nabla T| \approx \Delta T/s$ within distance s from the contact (Batchelor & O'Brien, 1977). Thus the total conductive luminosity passing through the contact is $\sim k \Delta T s$, from which we deduce that the effective conductivity

$$k_{\text{con}} \sim k\frac{s}{r} \approx k\left(\frac{P}{\epsilon_Y \mu}\right)^{1/2}. \tag{4.6}$$

Equation (4.6) applies in both low and high pressure regimes.

In the low pressure limit, $P < \epsilon_Y^3\mu$, perfect elastic spheres would have

$$k_{\rm con} \approx k\left(\frac{P}{\mu}\right)^{1/3} > k\left(\frac{P}{\epsilon_Y\mu}\right)^{1/2}, \tag{4.7}$$

but measurements of $k_{\rm con}$ in granular media consisting of commercially manufactured spheres (Watson, 1964; Huetter et al., 2008) obtain results similar to those found using crushed materials of similar composition and size. Presumably, even the surfaces of carefully manufactured spheres possess a spectrum of small scale irregularities.

4.3.2 Photon Conductivity

Radiation contributes to the effective conductivity in three ways.

- In a fluid free environment and absent physical contacts, only radiation can transfer energy between elements. To assess the rate at which it does so, we consider the simple setup displayed in Figure 4.2 in which parallel monolithic slabs of thickness ℓ are separated by a vacuum gap of thickness d. We assume steady state conditions and slabs opaque to thermal radiation. For $0 < \delta T < \Delta T << T$, the flux, F satisfies

$$F = 4\sigma T^3\delta T\,, \tag{4.8}$$

$$F = \frac{k(\Delta T - \delta T)}{\ell}\,, \tag{4.9}$$

$$F = k_{\rm rad}\frac{\Delta T}{\ell + h}. \tag{4.10}$$

  These equations yield

$$\frac{k_{\rm rad}}{k} = \frac{4(\ell+h)\sigma T^3}{k + 4\ell\sigma T^3} \tag{4.11}$$

$$\frac{\delta T}{\Delta T} = \frac{k}{k + 4\ell\sigma T^3} \tag{4.12}$$

  In the limit most important to our investigation, $k \gg 4\ell\sigma T^3$, $k_{\rm rad} \approx 4(\ell{+}h)\sigma T^3$ and $\delta T \approx \Delta T$. In other words, each slab is nearly isothermal and the conductive flux passing through it is determined by the rate at which radiation transfers energy across the vacuum gap separating adjacent slabs. Moreover, for $h \to 0$, $k_{\rm rad} \to 4\ell\sigma T^3$.

- Next imagine cutting holes of radius $\sim \ell$ in random locations through each slab. Now some photons may travel a vertical distance $\sim (\ell + h)$ before striking a slab. This provides a direct radiative conductivity $\sim (\ell + h)\sigma T^3$.

- Radiation can also transport energy through elements composed of transparent materials but we neglect this effect because ice and rock are opaque to infrared radiation.

Combining the results of the first two items discussed above, we define the radiative conductivity

$$k_{\rm rad} = \frac{16\ell\sigma T^3}{3}\,, \tag{4.13}$$

where following standard convention, ℓ is the inverse opacity per unit volume. In practice we expect that $\ell \sim r$, the typical linear size of both elements and voids.

4.3.3 Application to the Lunar Regolith

Keihm et al. (1973)[2] determined the thermal conductivity of the lunar regolith from temperatures measured by thermocouples the Apollo 15 astronauts placed on the Moon's surface. Their results

---

[2] **These results may suffer from poor thermal linkage in the probe-borestem system as remarked by**

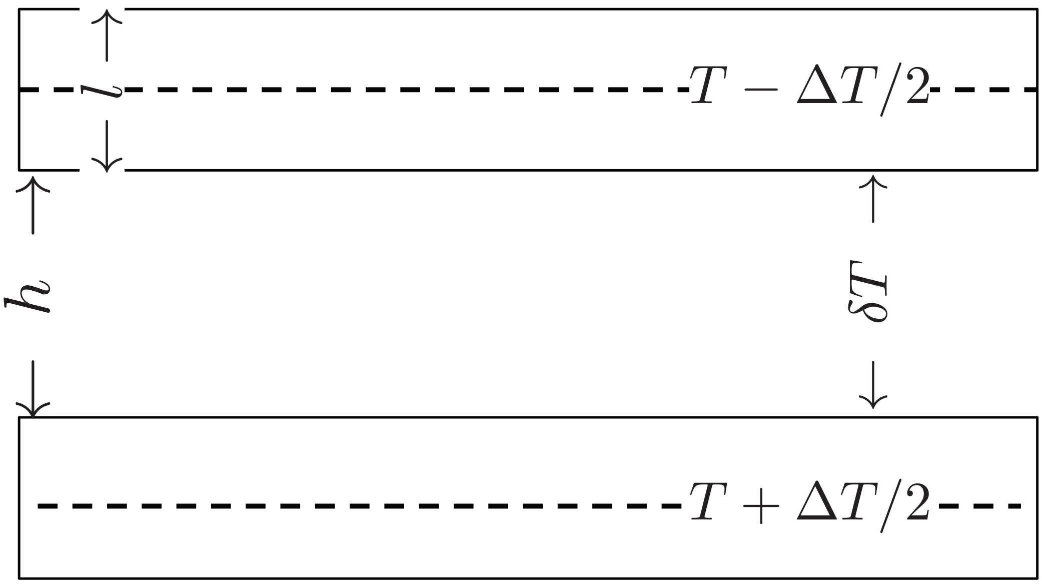

Figure 4.2 The central temperatures of the neighboring slabs differ by ΔT. Each slab has thickness ℓ and is separated from its neighbor by a vacuum of thickness d. the lower surface of the upper slab is a distance d above the upper surface of the lower slab, and the temperatures of these surfaces differ by δT.

are plotted as solid circles in Figure 4.3. The effective conductivity, $k_{\rm eff} = k_{\rm con} + k_{\rm rad}$, includes contributions from both phonon and photon diffusion. Because the latter is proportional to T^3, it is important to note that the values of $k_{\rm eff}$ are those appropriate for the mean temperature at each depth. Although temporal variations in surface temperature are large, spanning most of the range between $100 - 400\,{\rm K}$, those of the mean temperature are modest, rising from $\approx 200\,{\rm K}$ at the surface to $\approx 250\,{\rm K}$ at the maximum depth of 140 cm. Thus we neglect the latter and make a 2 parameter fit

to the data inspired by **contributions to $k_{\rm eff}$ from phonon and photon diffusion expressed by equations (4.7) and (4.13), respectively**. We find

$$k_{\rm eff} = \left[197\left(\frac{d}{\rm cm}\right)^{1/2} + 72\right] {\rm erg\,cm^{-1}\,s^{-1}\,K^{-1}}\ , \tag{4.14}$$

where d denotes depth below the surface. In choosing such a simple form, we are ignoring not only the depth dependence of the mean temperature but also potential variations with depth of grain size and composition. Equating the form of $k_{\rm con}$ from equation (4.6) to $197(d/\,{\rm cm})^{1/2}\,{\rm erg\,cm^{-1}\,s^{-1}\,K^{-1}}$, yields $\epsilon_Y \approx 5\times10^{-4}$ for $P \simeq \overline{\rho} g d$, with $\overline{\rho} \approx 1.5\,{\rm g\,cm^{-3}}$, $k \sim 2\times10^5\,{\rm erg\,cm^{-1}\,s^{-1}\,K^{-1}}$, $\mu \approx 5\times10^{11}\,{\rm dyne\,cm^{-2}}$, and $g \approx 160\,{\rm cm/s^2}$.[3] Setting $k_{\rm rad} = 72\,{\rm erg\,cm^{-1}\,s^{-1}\,K^{-1}}$ and appealing to equation (4.13), we obtain $\ell \approx 10^2\,(T/220\,{\rm K})^3\,\mu{\rm m}$ for the photon diffusion length. This length is several times smaller than the depth at which phonon and photon diffusion contribute equally to $k_{\rm eff}$. Another relevant comparison is with grain sizes at the Apollo 15 landing site. As reported by Papike et al. (1982), grains smaller and larger than $\approx 100\,\mu{\rm m}$ contribute similar amounts to the overall density of the regolith.

Langseth et al. (1976), in which k was estimated to be $30\% \sim 50\%$ smaller than that in Keihm et al. (1973).

[3] Given the order of magnitude nature of our analysis, the value of $\epsilon_Y \approx 5\times10^{-4}$ should be viewed as unremarkable. To fit the pressure dependence of the shear velocity in sand, Goldreich & Sari (2009) require $\epsilon_Y \simeq 0.17$.

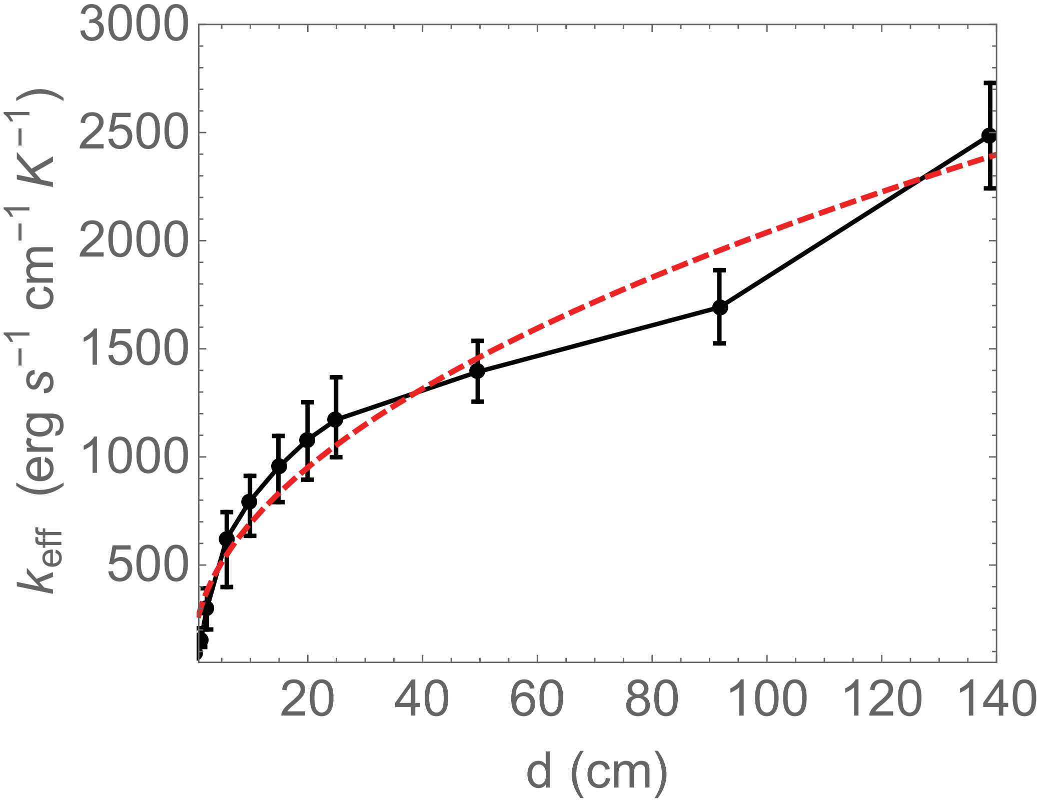

Figure 4.3 Filled circles with error bars are values of k_{eff} as a function of depth, d, at the Apollo landing site (Keihm et al., 1973). Our 2 parameter fit to the data given by Equation (4.14) is shown by the dashed red line. See main text for details.

4.4 Thermal Inertia

A body's thermal inertia is an important diagnostic of its surface. It is deduced from the amount by which variations of surface temperature, $T_{\rm s}$, lag those of the incident radiative flux. For monolithic material, thermal inertia is defined by

$$\Gamma_{\rm mon} \equiv (k\rho c_p)^{1/2} = \rho c_p \kappa^{1/2} \,, \tag{4.15}$$

where thermal diffusivity,

$$\kappa = \frac{k}{\rho c_p} \,, \tag{4.16}$$

with c_p denoting specific heat capacity.

Provided all vibrational degrees of freedom are classically excited, common monolithic insulators share the almost universal values of $\rho c_p \approx 2\times 10^7\,{\rm erg\,cm^{-3}\,K^{-1}}$ and $\kappa \approx 10^{-2}\,{\rm cm^2\,s^{-1}}$ (White, 2012). Each nucleus contributes $3k_B$ to the heat capacity and is surrounded by an electron cloud whose volume is insensitive to the screened nuclear charge. Taking each nucleus to occupy a cube with $2.75\mathring{A}$ sides yields $\rho c_p \approx 2\times 10^7\,{\rm erg\,cm^{-3}\,K^{-1}}$. Most of the thermal energy is stored in the shortest wavelength lattice vibrations and typically these propagate a few lattice spacings at speeds of a few ${\rm km\,s^{-1}}$ before being scattered. With mean free path $\lambda \approx 10\mathring{A}$ and propagation speed $v \sim 3\,{\rm km\,s^{-1}}$, $\kappa \approx \lambda v/3 \sim 0.01\,{\rm cm^2\,s^{-1}}$. Consequently,[4]

$$\Gamma_{\rm mon} \approx 2\times 10^6\,{\rm erg\,s^{-1/2}\,cm^{-2}\,K^{-1}} \,. \tag{4.17}$$

We motivate the definition of thermal inertia by means of a simple example. Consider the response of a body to the sudden imposition of a constant incident flux F at $t = 0$. In the interest of simplicity, we treat a monolithic body with k independent of both P and T and assume zero albedo. Surface temperature, $T_{\rm s}$, is determined by balancing the incident flux against the sum of the outward radiative flux and the inward conductive flux;

$$F = \sigma T_{\rm s}^4 + k\frac{dT}{dz} \sim \sigma T_{\rm s}^4 + \left(\frac{k\rho c_p}{t}\right)^{1/2} T_{\rm s} \,, \tag{4.18}$$

where we approximate dT/dz by $T_{\rm s}$ divided by the penetration depth, $(\kappa t)^{1/2}$, for thermal diffusion during time t. Initially most of the incident flux is conducted inward and

$$T_{\rm s} \sim \left(\frac{t}{\rho k c_p}\right)^{1/2} F \,. \tag{4.19}$$

At

$$t_{\rm lag} \sim \frac{k\rho c_p}{(\sigma T_{\rm s}^3)^2} = \left(\frac{\Gamma}{\sigma T_{\rm s}^3}\right)^2 \,, \tag{4.20}$$

the outward radiative and inward conductive fluxes are comparable. Thereafter, the radiative flux dominates and $T_{\rm s}$ asymptotically approaches $(F/\sigma)^{1/4}$.

Fitting variations of surface temperature in response to variations of incident solar flux requires a model for $k_{\rm eff}$. Ours includes depth dependence from $k_{\rm con}$ and temperature dependence from $k_{\rm rad}$. Here we consider limiting cases in which either the former or the latter dominates.

- Suppose phonon diffusion dominates heat transfer; $k_{\rm eff} \approx k_{\rm con}$.

  We evaluate $\Gamma_{\rm con} \approx (k_{\rm con}\overline{\rho} c_p)^{1/2}$ at the depth to which the thermal wave propagates in time

---

[4] We express thermal inertia in the cgs unit, ${\rm erg\,s^{-1/2}\,cm^{-2}\,K^{-1}}$, instead of the more convential mks unit ${\rm J\,s^{-1/2}\,m^{-2}\,K^{-1}} = 10^3\,{\rm erg\,s^{-1/2}\,cm^{-2}\,K^{-1}}$.

t, $d \approx (k_{\rm con} t/(\overline{\rho} c_p))^{1/2}$. This procedure yields

$$\Gamma_{\rm con} \approx \left(\frac{k^2 \overline{\rho}^2 c_p \, g \, t^{1/2}}{\epsilon_Y \mu}\right)^{1/3} , \tag{4.21}$$

for flux variations on timescale t.

- Next consider the opposite limit in which photon diffusion dominates; $k_{\rm eff} \approx k_{\rm rad}$. Here

$$\Gamma_{\rm rad} = \left(\frac{16 \ell \sigma T^3 \overline{\rho} c_p}{3}\right)^{1/2} , \tag{4.22}$$

which has no explicit dependence on t.

From observations during a lunar eclipse with umbral duration $t \sim 2\,$h, Muncey (1963) estimates $\Gamma \approx 2.8 \times 10^4 \,{\rm erg\,s^{-1/2}\,cm^{-2}\,K^{-1}}$. Linsky (1966) estimates $3.9 < \Gamma < 6.7 \times 10^4 \,{\rm erg\,s^{-1/2}\,cm^{-2}\,K^{-1}}$ from data obtained during a lunation, $t \approx 28\,$d. From Keihm et al. (1973) and our fit to $k_{\rm eff}$ in equation (4.14), it appears that both phonon and photon diffusion contribute significantly to Γ during a lunar eclipse but that the phonon contribution dominates during a lunation. Unfortunately, neither these old data nor our theory are precise enough to justify a more detailed analysis. Mid-infrared measurements made by the radiometer on the Lunar Reconnaissance Orbiter presents a comprehensive picture of the Moon's surface temperature over 4 lunations (Vasavada et al., 2012). It clearly warrants more careful modeling than we are currently capable of doing.

Microwave measurements from the Rosetta orbiter made prior to Philae's landing on comet 67P/Churyumov-Gerasimenko, were interpreted to imply a representative thermal inertia, Γ, in the range $(1-5) \times 10^4 \,{\rm erg\,s^{-1/2}\,cm^{-2}\,K^{-1}}$ for the overall surface (Gulkis et al., 2015). Shortly thereafter, diurnal temperature variations measured at the Philae landing site, Abydos, yielded an estimate of $\Gamma = (8.5 \pm 3.5) \times 10^4 \,{\rm erg\,s^{-1/2}\,cm^{-2}\,K^{-1}}$ for the local thermal inertia (Spohn et al., 2015) . These low values imply a porous surface. Lack of knowledge of the local regolith prevents the direct application of our formulae for Γ. However, in-situ measurements of the variation of the surface temperature over the comet's orbital period might separate contributions from phonon and photon conduction because we expect $\Gamma_{\rm con} \propto t^{1/6}$ and $\Gamma_{\rm rad}$ independent of t.

Thermal inertia is an essential component of the Yarkovsky effect which drives significant orbital migration of small asteroids (Bottke et al., 2006). This migration is responsible for the rate at which the semi-major axes of members of asteroid families separate. It also impacts the timescale for the delivery of meteorites from the asteroid belt to Earth. Phase lags expressed in radians of rotational phase, $\Delta\phi$, can be estimated by multiplying $t_{\rm lag}$ in equation (4.20) by the spin frequency of the asteroid;

$$\begin{aligned}\Delta\phi &\approx \frac{2\pi}{P_{\rm sp}} \left(\frac{\Gamma}{\sigma T^3}\right)^2 \sim 5 \times 10^4 \left(\frac{P_{sp}}{\rm h}\right)^{-1} \\ &\times \left(\frac{T}{200\,{\rm K}}\right)^{-6} \left(\frac{\Gamma}{\Gamma_{\rm mon}}\right)^2 . \end{aligned} \tag{4.23}$$

Phase lags given by equation (4.23) are relevant to the diurnal Yarkovsky effect. There is also a seasonal Yarkovsky effect which involves the phase lag expressed in terms of the orbital phase. In each case, migration rates are optimized for phase lags of order a radian (Bottke et al., 2006).

Howett et al. (2010) estimate thermal inertias for the Saturnian satellites Mimas, Enceladus, Tethys, Dione, Rhea and Iapetus from infrared data obtained by the Cassini orbiter. Each satellite has an outer ice shell and spins synchronously so incident solar flux variations occur on timescales of its orbital period, P_{orb}. Thermal inertias are plotted in Figure (4.4). They are low and show no obvious trend with orbit period. This suggests that heat transport by photon diffusion probably dominates that by phonon diffusion at the top of their regoliths; i.e., $\kappa_{\rm rad} > \kappa_{\rm con}$ even for Iapetus. Otherwise, it would be expected from equation (4.21) that the 10^3 fold increase of $g^2 P_{orb}$ in going from Mimas to Iapetus would lead to a noticeable, factor of ≈ 3, rise of Γ as indicated by the dashed line in Figure (4.4).[5]

The average Γ for Saturn's satellites is $1.3 \times 10^4\,\mathrm{erg\,s^{-1/2}\,cm^{-2}\,K^{-1}}$ as shown by the dotted blue line in Figure (4.4). With $\Gamma_{\mathrm{rad}} \approx 7.8 \times 10^4\,(T/100\,\mathrm{K})^{3/2}\,(\ell/\,\mathrm{cm})^{1/2}\,\mathrm{erg\,s^{-1/2}\,cm^{-2}\,K^{-1}}$, it follows that $\ell \approx 0.04(90\,\mathrm{K}/T)^3\,\mathrm{cm}$, an unremarkable value. But an upper limit of $\Gamma_{\mathrm{con}} \leq 1.3 \times 10^4\,\mathrm{erg\,s^{-1/2}\,cm^{-2}\,K^{-1}}$ for Iapetus is problematic. Substitution of $\rho \sim 0.93\,\mathrm{g\,cm^{-3}}$, $\mu \sim 4 \times 10^{10}\,\mathrm{dyne\,cm^{-2}}$, $c_p \sim 2 \times 10^7\,\mathrm{erg\,cm^{-3}\,K^{-1}}$, $k \sim 2 \times 10^5\,\mathrm{erg\,cm^{-1}\,s^{-1}\,K^{-1}}$, $g \approx 22.4\,\mathrm{cm\,s^{-2}}$, $\epsilon_Y = 0.01$ and $t = 79/(2\pi)\,\mathrm{d}$ into equation (4.21) yields $\Gamma_{\mathrm{con}} \approx 3.5 \times 10^4\,\mathrm{erg\,s^{-1/2}\,cm^{-2}\,K^{-1}}$. The astute reader will recognize that the substituted values are appropriate for water ice at 273 K. Moreover, although $\epsilon_Y = 0.01$ is a reasonable value for the yield strength of a single crystal of cold ice, it is a large one for polycrystalline ice (Hobbs, 1974; Schulson, 2001). Substituting parameters suitable for pure water ice at 90 K would not help; k would be larger and although c_p would be smaller, the product $k^2 c_p$ would be slightly larger. We have checked this statement for T down to 173 K and see no reason why it would not apply for T as low as 90 K. A significant reduction of ρ is more plausible; on Earth, accumulations of dry snow with water content below 30% are common. The weaker gravity on Iapetus would permit even lower densities than on Earth. Even at temperatures below 90 K, ice grains might bond to their neighbors.[6] Bonding could enable both low ρ and large ϵ_Y. According to Borderies et al. (1984), bonding is the most likely explanation for the paucity of sub-centimeter water ice particles in Saturn's rings.

4.5 Summary

Together, phonon and photon diffusion determine the thermal conductivity of a rubble pile.

Phonons transmit heat through contacts between neighboring elements. Conductivity due to phonon diffusion in granular materials is independent of the sizes of the individual elements. We consider irregularly shaped elements whose mutual contact areas in the low pressure regime, $P < \epsilon_Y^3 \mu$, are smaller than those for spheres. Consequently, they provide a lower phonon conductivity than spheres, but one that increases more rapidly with pressure, $\propto P^{1/2}$, rather than, $\propto P^{1/3}$ for spheres. At $P \approx \epsilon_Y^3 \mu$, phonon conductivities of irregular elements and spheres are equal. At still higher pressure, the contact areas of both spheres and irregularly shaped elements are governed by equation (4.2).

The effective conductivity in the top 140 cm of the lunar regolith as deduced from radiometer measurements of surface temperatures (Keihm et al., 1973) roughly agrees with our prediction $k_{\mathrm{eff}} \propto d^{1/2}$. But measurements of the annual temperature variation by probes analyzed by Langseth et al. (1976) indicate that k_{eff} is nearly constant at about 10^{-2} of the monolithic conductivity for $d \leq 250\,\mathrm{cm}$. This result has no simple explanation since contact areas should monotonically increase with increasing pressure.

Photons transmit heat across voids between elements. Photon diffusion contributes $k_{\mathrm{rad}} \propto \ell T^3$, where ℓ is the linear size of a typical element. A subtle argument in 4.3.2 shows that the element size is more important than the void size in determining the appropriate value of ℓ.

Thermal inertias of Saturnian satellites exhibit little dependence on $g^2 P_{orb}$ suggesting that photon diffusion may dominate k_{eff}. This is surprising both because their surface temperatures are low and the implied values of k_{eff} are smaller than one might expect from phonon diffusion alone.

---

[5] Here we assume that these satellites have similar regoliths.

[6] Bonding increases contact areas at fixed pressure and implies finite contact areas at zero pressure (Johnson, 1987).

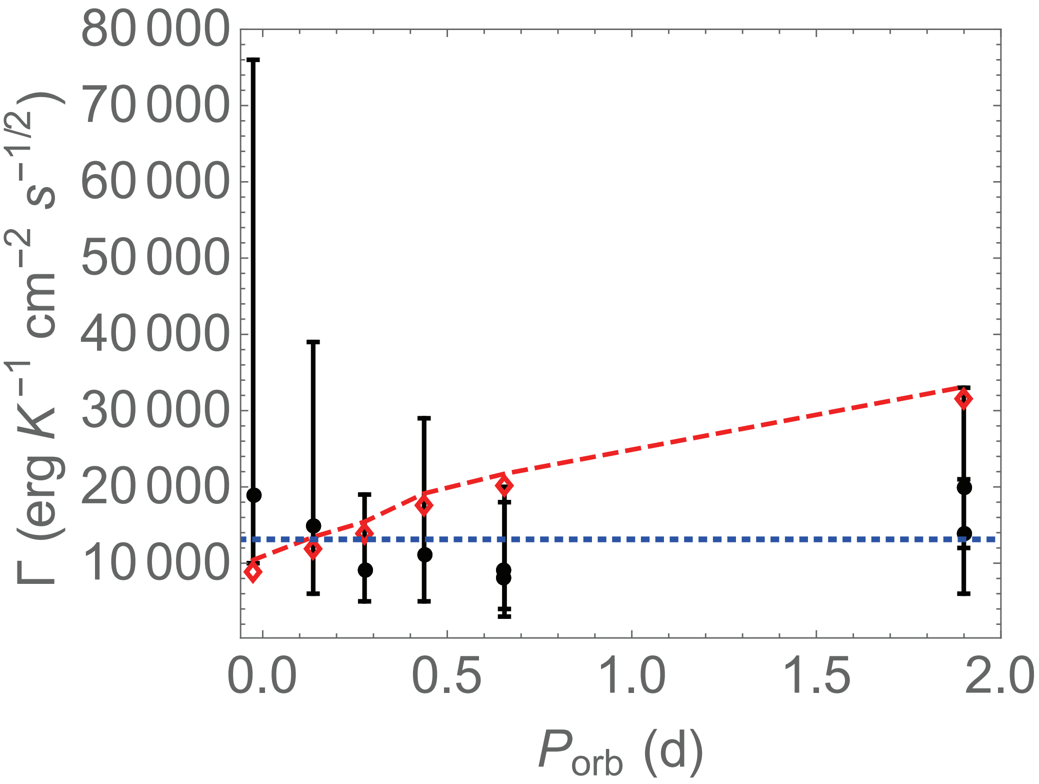

Figure 4.4 Comparison between data (Howett et al., 2010) in black and theoretical estimates based on the assumed dominance of either phonon diffusion (dashed red line) or photon diffusion (dotted blue line). The former is normalized to pass through the lowest value for Γ of Mimas. Its rise with increasing P_{orb} is attributable to the $\approx 10^3$-fold increase of $g^2 P_{\rm orb}$ from Mimas to Iapetus. The constant value of $\Gamma_{\rm rad} \approx 1.3 \times 10^4\,{\rm erg\,s^{-1/2}\,cm^{-2}\,K^{-1}}$ corresponds to setting $\ell \approx 0.04\,{\rm cm}$ for $T \approx 90\,{\rm K}$. See main text for more details.

Chapter 5

Towards Low-Latency Real-Time Detection of Gravitational Waves from Compact Binary Coalescences in the Era of Advanced Detectors

5.1 Introduction

Coalescences of neutron-star (NS) binaries are primary sources for ground-based gravitational-wave detectors. It has been estimated that Advanced LIGO may be able to detect 10 to 100 such events per year O'Shaughnessy et al. (2010). The mergers of neutron star binaries are also possible progenitors of short hard γ-ray bursts. Although these bursts are believed to be mostly beamed away from us, the prompt emission and afterglow they induce in X-ray, optical, infrared and radio frequency bands may well be less beamed, and therefore be visible to us Fox et al. (2005); Nakar (2007). If a statistically significant gravitational-wave *trigger* can be obtained before or right after such a coalescence, electromagnetic (especially optical) observatories can then be alerted to search for possible prompt and afterglow emissions — such follow-up observations are likely able to resolve whether these mergers are indeed the progenitors of short hard γ-ray bursts, and provide further knowledge about the nature of these events.

Currently, neutron star - neutron star coalescence signals are being searched for in gravitational-wave data using the matched filtering technique Finn (1992); Cutler & Flanagan (1994), which calculates the correlation of *data* with *theoretical templates* weighted by noise. In order to reduce the computational cost, current search pipelines use a frequency-domain method, which gathers a long stretch of time-series data containing $O(N)$ points (the duration of which should be longer than the longest possible signal), then uses a Fast-Fourier-Transform (FFT) algorithm to search for all possible signals that end within this stretch of data, with a cost of $O(N \log N)$, as opposed to the $O(N^2)$ required by a one-by-one search over merger time. Such a trick, although efficient, implies that we cannot start analyzing the data until the collection finishes.

Unless significant changes from current frequency-domain analysis method are made, the latency caused by data collection will compromise our ability to obtain a trigger with the shortest possible delay after the merger, and will totally prevent us from obtaining the trigger before the merger. At least two efforts are underway to suppress latencies for coalescence signals, the Multi-Band Template Analysis (MBTA) Buskulic et al. (2010) and the Low-Latency Online Inspiral Detector (LLOID) Cannon et al. (2011c). MBTA is a two-band frequency-domain search method while LLOID provides an infrastructure that accommodates either time or frequency domain searches. The time-domain aspect of the LLOID pipeline based on Finite-Impulse-Response (FIR) filters Rabiner & Gold (1975) is described in a parallel paper Cannon et al. (2011c). Note for a different search of

Detector	$f_{\rm min}$ (Hz)	duration (s)	$N_{\rm cyc}$	$\mathcal{N}_{0.98}$
iLIGO	40	25	1.6×10^3	1.7×10^3
aLIGO	10	1.0×10^3	1.6×10^4	6.6×10^3
ET	3	2.5×10^4	1.2×10^5	2.9×10^4

Table 5.1 Basic information for the detection of Newtonian GW signals by initial, Advanced LIGO and Einstein Telescope. The columns, from left to right list the names for present and future detectors, the minimum frequency of the detector, signal duration and number of wave cycles for a $(1.4{+}14)M_\odot$ NS-NS binary [see Sec. 5.3.1], as well as the number of templates required in order to achieve a match of 0.98 for binaries with individual mass of $1 - 3\,M_\odot$ [computed from the metric Eq. (5.57)].

short gravitational waves of unknown waveforms, a program has been set up to analyze available detector data in near real-time and seek for optical counterpart of candidate events Kanner et al. (2008).

In this paper, we propose a straightforward and efficient time-domain search algorithm, which allows zero and even negative latency (i.e., obtaining trigger before the merger if the signal-to-noise ratio (SNR) condition and other consistency conditions are met) in the most natural way. Admittedly, without the savings made available by FFT, the computational cost of a straightforward implementation using FIR filters can be formidable. In the correlation calculation, each template contains a large number of wave cycles, and there exists a large number of templates — and both these numbers increase dramatically with the lowering of the minimum frequency cutoff $f_{\rm min}$ (Table 5.1). This poses serious computational challenge for detecting GWs from compact object coalescence for future GW detectors.

We propose two techniques that can dramatically increase the computational efficiency for time-domain searches of GWs from coalescing binaries of compact objects in real-time, and make it feasible for future detectors with frequency cut-offs at as low as $f_{\rm min} = 3\,$Hz. The first technique uses the well-known Infinite Impulse Response, or IIR filters Rabiner & Gold (1975), which can be computed with much higher efficiency than FIR filters. We propose to filter the data using a bank of IIR filters, the sum of which approximates each individual binary coalescence waveform template. The second technique reduces the number of templates by an interpolation technique that applies to the proposed IIR filter method. In this approach, we first divide the bank of IIR filters associated with each template into sub-groups, and then reconstruct the filter outputs of a fine template bank by recombining the filter outputs from each of these sub-groups with appropriate complex coefficients and time delays. This is similar to the generic multi-band interpolation scheme used in MBTA and LLOID Buskulic et al. (2010); Cannon et al. (2010, 2011a).

Several conventions are used in this paper. The term *latency* refers generally to the delay from the time when a signal arrives at the detector to the time the data containing the signal actually starts to be analyzed. We specifically focus on the delay starting from the time when the data are ready to be analyzed. One example of the latency is the delay due to data accumulation before a Fast Fourier Transformation (FFT) can be performed. The term *real time* processing means that data points or data segments are processed (with outputs generated) at a rate that is equal to their input rate. Floating Point Operation is abbreviated as FLOP (plural FLOPs). FLOPS and *flops* are used interchangeably to stand for Floating Point Operations per Second. Throughout this paper, we follow the convention of counting each real addition and real multiplication equally as one FLOP.

This paper is structured as follows. In Section 5.2 , we briefly review the basics of matched filtering technique and introduce time-domain IIR filters. In Section 5.3, we use Newtonian-order templates as an example to construct IIR filters, characterize the error involved and calculate the computational cost for each individual template. In Section 5.4, we present an interpolation technique that allows us to use a significantly decreased number of templates for which filter chains must be implemented. In Section 5.5, we make a simple comparison between the computational cost of IIR filtering and the straightforward frequency-domain algorithm. In Section 5.6, we summarize our main conclusions.

5.2 Matched Filtering Technique

The optimal technique to extract a signal from noisy data when we have reliable theoretical predictions for the signal *waveform* is to use *matched filtering* Finn (1992); Cutler & Flanagan (1994). The output of the matched filtering technique is basically the correlation of data with expected waveforms weighted by noise. This can be realized in the frequency or time domain. We will give a brief overview of the matched filtering technique, and introduce its frequency-domain implementation and its time-domain approach using the FIR and IIR filters.

5.2.1 Frequency-domain implementation

5.2.1.1 Single template

Suppose the output of the interferometer h is a sum of noise n and, if exists, a signal s:

$$h = n + s \tag{5.1}$$

For the moment, let us assume that s is a single known *waveform.* In Eq. (5.1), we have intentionally left out the arguments of the functions h, n, and s, which reflects the point of view that each of them can be equivalently *represented* both in the time and frequency domain. More specifically, we use the following convention for Fourier transform, which relates $h(t)$ and $\tilde{h}(f)$ (we shall use tilde to emphasize a frequency-domain representation):

$$\tilde{h}(f) \equiv \int_{-\infty}^{\infty} dt e^{i2\pi f t} h(t). \tag{5.2}$$

The power spectral density of $n(t)$ is denoted by $S_h(f)$, which is defined by

$$E[\tilde{n}(f)\tilde{n}^*(f')] = \frac{1}{2}\delta(f - f')S_h(f). \tag{5.3}$$

Here we use one-sided spectral density, $E[\ ]$ denotes the expectation value over an ensemble of realizations of the noise and "$*$" denotes complex conjugation. $S_h(f) = S_h(|f|)$ as the noise in the time domain $n(t)$ is real.

In order to extract s from h, we perform *filtering*, which consists of taking the *inner product* between data h and *template* u, forming a *filter output* of y:

$$y = \langle h|u\rangle = \langle s|u\rangle + \langle n|u\rangle \tag{5.4}$$

Here we define inner product as

$$\begin{aligned} \langle a|b\rangle &\equiv 2\int_0^{\infty} df \frac{\tilde{a}^*(f)\tilde{b}(f) + \tilde{a}(f)\tilde{b}^*(f)}{S_h(f)} \\ &= 4\mathrm{Re}\left[\int_0^{\infty} \frac{\tilde{a}^*(f)\tilde{b}(f)}{S_h(f)}\right]. \end{aligned} \tag{5.5}$$

In y, we have a signal component $\langle s|u\rangle$ and a noise component $\langle n|u\rangle$ which fluctuates around zero. If s has a substantially high amplitude and if the template u is appropriate, the signal component $\langle s|u\rangle$ in y will raise to a high value that merely random fluctuation of $\langle n|u\rangle$ is very unlikely to account for. As a consequence, we can impose a threshold on y — an incidence with y higher than the threshold is viewed as a detection of a signal. The detection efficiency depends on the signal-to-noise ratio

(SNR) defined generally as

$$\rho = \frac{y(n=0) - E[y(s=0)]}{\sigma_{y(s=0)}}, \tag{5.6}$$

where $\sigma_{y(s=0)}$ is the standard deviation of the filter output when data contain noise only. Assuming zero-mean Gaussian noise, we have for Eq. (5.4)

$$\rho \equiv \frac{\langle s|u\rangle}{\sqrt{E[|\langle n|u\rangle|^2]}}, \tag{5.7}$$

Note that the SNR does not depend on the normalization of the template u, and it is conventional to require that $\langle u|u\rangle = 1$. In this case, the cross-correlation of a template with pure noise $\langle n|u\rangle$ is a random variable with zero mean and unity variance. It is easy to show that $E[\langle n|a\rangle\langle n|b\rangle] = \langle a|b\rangle$. So we have

$$\rho = \langle s|u\rangle. \tag{5.8}$$

According to the Cauchy-Schwarz inequality,

$$\rho = \frac{\langle s|u\rangle}{\sqrt{\langle s|s\rangle}}\sqrt{\langle s|s\rangle} \leq \sqrt{\langle s|s\rangle}, \tag{5.9}$$

where equal sign takes place when $u = \lambda s$ where λ is a constant, and normalization of u gives $\lambda = 1/\sqrt{\langle s|s\rangle}$. This means the *optimal* SNR is given by the modulus of the signal, $\langle s|s\rangle$, and the *reduction* of SNR due to imperfectness of template is given by the *match*, which is also equal to unity minus mismatch, ε:

$$\frac{\langle s|u\rangle}{\sqrt{\langle u|u\rangle\langle s|s\rangle}} \equiv 1 - \varepsilon. \tag{5.10}$$

5.2.1.2 Intrinsic and extrinsic parameters

In reality, templates are not necessarily placed along each parameter dimension. The maximization of SNR over certain parameters can be conducted analytically and therefore no templates are needed. These parameters are called *extrinsic parameters*, while those that still have to be searched over one by one are called *intrinsic parameters*.

As an example, for any generic waveform $u(t) = Au_0(t - t_c)e^{i\phi_c}$, where A is a real number, ϕ_c is the phase difference between $u(t_c)$ and $u_0(t_c)$, and t_c is its *ending time*. The ending time t_c is an extrinsic parameter, because as a series of templates $u_0(t - t_c)$ with a variety of t_c are applied to the data h, the SNR

$$\rho(t_c) = 4\,\mathrm{Re}\int_0^\infty \frac{\tilde{h}^*(f)\tilde{u}_0(f)}{S_h(|f|)}e^{i2\pi f t_c}df \tag{5.11}$$

can be computed for all t_c via a Fast Fourier Transform, which cost $O(N\log N)$ FLOPs in the discretized case where N is the number of data points in the time domain. This is much faster than computing the correlation for all possible ending times, one by one, which cost $O(N^2)$ operation counts — and in this way ending time t_c is converted into an extrinsic parameters. The method of Fourier transformation will be discussed in detail in subsection 5.5.2. This process dominates the computational cost for the matched filtering method. Further analytical optimization are known for the search of the constant phase ϕ_c. We assume the process is similar for all methods discussed in this paper and that its computational cost is negligible.

5.2.2 Time-domain approach: FIR and IIR method

For the time-domain filtering we need to obtain a time series of SNRs as a function of presumed signal arrival time t

$$\begin{aligned} \rho(t) &= 2\int_{-\infty}^{\infty} \frac{\tilde{h}^*(f)\tilde{u}(f)}{S_h(|f|)} e^{+i2\pi ft} df \\ &= \int_{-\infty}^{+\infty} w(t')u(t'-t)dt' \end{aligned} \tag{5.12}$$

with

$$w(t) \equiv 2\int_{-\infty}^{\infty} df \frac{\tilde{h}(f)}{S_h(f)} e^{-i2\pi ft}, \tag{5.13}$$

which can be thought of as "over-whitened data"; it is a real-valued function of time. Note that in order to generate the over-whitened data, we need to convolve $h(t)$ with the Inverse Fourier Transform of $1/S_h(f)$, which is a time-symmetric, oscillatory function that decays towards zero when t is much larger than the inverse of the interferometer's bandwidth ($\gtrsim 100\,\mathrm{Hz}$), which is about $\lesssim$ 10ms. This means the over-whitening process has an inherent latency not much larger than 10ms, which is negligible compared to the duration of the signal.

We now discretize the filtering algorithm. The discrete form of Eq (5.12) becomes,

$$\rho_k = \sum_{j=-\infty}^{k} w_j u_{j-k} \Delta t, \tag{5.14}$$

Here we assume $t_k = k\Delta t$, and that u only have support within $t \leq 0$. While in principle the waveform u_k could have an infinite support in time, $-\infty < k\Delta t < 0$. However, the waveform $u(t)$ is always assumed to begin only after its amplitude reaches sensitivity within the LIGO band. Hence we instead define the waveform to exist on the domain $-N\Delta t \leq t \leq 0$, and Eq (5.14) becomes,

$$\rho_k = \sum_{j=k-N}^{k} w_j u_{j-k} \Delta t, \tag{5.15}$$

This summation of the product of data and template at each step turns out to be the general form of Finite Impulse Response (FIR) filters. The term *finite* comes from the fact that the output ρ_k of the filter (its response) will become exactly zero after N time steps have passed since a single initial impulse in the data. For example, if we assume $w_0 = 1$, $w_k = 0$ for $k \neq 0$, then ρ_k will vanish for $k > N$. As seen from Eq. (5.15), each ρ_k costs N multiplications and N additions to calculate. This translates into a computational cost, in terms of FLOPs per unit time, of $\sim N/\Delta t$.

For certain types of waveforms, Infinite Impulse Response (IIR) filters can be used to dramatically reduce computational cost. The simplest IIR filter is a first-order recursive algorithm, in which the k-th output y_k is a linear combination of the $(k-1)$-th output, y_{k-1} and the k-th data, w_k:

$$y_k = e^{-(\gamma - i\Omega)\Delta t} y_{k-1} + w_k \Delta t, \tag{5.16}$$

where γ, Ω are real-valued constants with $\gamma > 0$ to ensure stable solutions. It can be shown that, e.g., by using tools of Z-transform Oppenheim & Schafer (1975), as long as w_k does not diverge towards $k \to -\infty$, then even if the recursion starts at a finite time step, after an initial transient of several times $1/\gamma$, the output of the filter achieves a steady state of

$$y_k = \sum_{j=-\infty}^{k} w_j e^{(\gamma - i\Omega)(j-k)\Delta t} \Delta t. \tag{5.17}$$

Note this is the discretized version of the continuous integration

$$y(t) = \int_{-\infty}^{\infty} w(t')e^{(\gamma-i\Omega)(t'-t)}\Theta(t-t')dt'. \tag{5.18}$$

Note first that Eq. (5.17) indeed gives an infinite impulse response, because for a data series containing only one impulse, $w_0 = 1$ and $w_k = 0$ $(k \neq 0)$, the output of the filter, even at very late time steps, never vanishes. More over, by comparing this with Eq. (5.12), the IIR filter can be viewed as a template of a damped sinusoid:

$$u(t) = e^{(\gamma+i\Omega)t}\Theta(-t), \tag{5.19}$$

where $\Theta(t)$ is the Heaviside function

$$\Theta(t) = \begin{cases} 0, & t \leq 0; \\ \\ 1, & t \geq 0. \end{cases} \tag{5.20}$$

The IIR filter described above requires only one complex multiplication and one summation per sampling time, which means the computational cost is $\sim 1/\Delta t$.

For a simple proof of concept on the computational efficiency of the IIR over the FIR filtering technique, we examine the case when we *do* need to filter for a damped sinusoid signal with frequency Ω and decay rate γ. The data to be filtered has a duration of at least on the order of $1/\gamma$. The Nyquist sampling theorem limits the sampling interval to be at most $\sim 1/\Omega$, meaning that the FIR template would have the number of data points several times larger than Ω/γ. Subsequently the computational cost of the FIR in FLOPs per unit time is larger than Ω^2/γ. An IIR filter, on the other hand, only has a cost of Ω, which means the cost of IIR filter is $\gamma/\Omega \sim 1/Q$ times that of FIR filter, where $Q \equiv \Omega/\gamma$ is the quality factor of the damped sinusoid. As a consequence, if we can convert our waveforms into a sum of a series of of high-Q damped sinusoids, IIR filters can be used over the FIR to dramatically reduce the computational cost.

5.3 Construction of IIR filters for an Individual Inspiral Waveform

The simple IIR filter discussed in the previous section has the special waveform of a decaying sinusoid [Cf. Eq. (5.19)]. In this section, we will show that a *chain* of IIR filters can be used to "piece together" the waveforms of compact binary coalescence. This is possible because these waveforms are basically sinusoids with slowly varying amplitude and frequency. For simplicity, in this paper, we will restrict ourselves to Newtonian Chirps.

5.3.1 The Newtonian chirp waveform

The Newtonian-chirp is the leading-order waveform from a compact coalescing binary. In the time domain it can be written as the real part of the complex expression (see, e.g., Cutler & Flanagan (1994), Sec. C),

$$u(t) \propto (t_c - t)^{-1/4} e^{-i2(5M_c)^{-5/8}(t_c-t)^{5/8}+i\phi_c} \equiv \mathcal{A}(t)e^{i\Phi(t)} \tag{5.21}$$

where we follow the convention of the Planck unit that sets gravitational constant $G = 1$ and the speed of light, $c = 1$, M_c is the *chirp mass* of the binary,

$$M_c = M\eta^{3/5} \tag{5.22}$$

which depends on the total mass of the binary M and $\eta \equiv m_1m_2/M^2$, the symmetric mass ratio. The signal finishes at the ending time t_c, and ϕ_c is the constant phase at the end time. Here we have ignored time-independent factors of proportionality in the amplitude, which do not affect template construction.

We have assigned real-valued functions $\mathcal{A}(t)$ and $\Phi(t)$ to denote the amplitude and phase of the waveform. Although the actual waveform is the real part of $u(t)$, we have intentionally kept its complex form, because the imaginary part of $u(t)$ represents the waveform of a binary with a phase shift of $\pi/2$ from the real part— therefore the real and imaginary parts together form a *basis* for the *linear space of signals of all phases*. This is a feature of all *adiabatic waveforms*, which satisfy

$$\dot{\mathcal{A}}/(\Omega\mathcal{A}) \ll 1, \quad \dot{\Omega}/\Omega^2 \ll 1. \tag{5.23}$$

In other words, the amplitude $\mathcal{A}(t)$ and angular frequency $\dot{\Phi}(t)$ both evolve at rates much slower than the instantaneous frequency $\dot{\Phi}$. This allows us to use the Stationary Phase Approximation (SPA) to compute the Fourier Transform of the waveform in Eq. (5.21),

$$\tilde{u}(f) \propto f^{-7/6} e^{i(Af^{-5/3}+2\pi f t_c+\phi_c-\pi/4)}, \quad f > 0\,, \tag{5.24}$$

where

$$A = \frac{3}{4}(8\pi M_c)^{-5/3} \tag{5.25}$$

is the intrinsic parameter we need to search for in the case of Newtonian chirp. Note that when we Fourier-transform the complex signal of Eq. (5.21), there is only positive-frequency component, with $\tilde{u}(f) = 0$ for $f < 0$. On the other hand, if we took the real part of the signal, we would have $\tilde{u}(-f) = \tilde{u}^*(f)$ for $f > 0$.

The duration of a coalescence GW signal can be well approximated as a function of chirp mass M_c (Eq. (5.22)) and the detector's minimum cut-off frequency $f_{\rm min}$,

$$T(M_c, f_{\rm min}) = \frac{647013}{(f_{\rm min}/{\rm Hz})^{8/3}(M_c/M_\odot)^{5/3}} \ {\rm s}. \tag{5.26}$$

One can see that for a fixed $f_{\rm min}$, the longest signal duration corresponds to the smallest chirp mass. The sample signal durations for the initial, advanced and future GW detectors of various $f_{\rm min}$ can be found in Table 5.1, column 3. It is shown that GWs from a canonical (1.4+1.4)$M_\odot$ NS-NS binary system will have a duration 40 times longer for advanced detectors, and possibly 10000 time longer for the future ET detector than that of the initial detector.

5.3.2 An IIR filter chain

The adiabatic condition in Eq. (5.23) also implies that the waveform can be divided into *constant-frequency intervals*: within each interval it can be approximated as a sinusoid with constant frequency, while neighboring intervals have slightly different frequencies. This further indicates that we can attempt to write the entire waveform into the sum of a series of damped sinusoids: the frequency of each sinusoid corresponds to a constant-frequency interval, the ending time of the sinusoid corresponds to the ending time of this constant-frequency interval, while the decay time should be comparable to the length of the constant-frequency interval. The amplitude of the decaying sinusoid can be set to be comparable to the amplitude of the original waveform during the corresponding constant-frequency interval.

Mathematically, our target is therefore to approximate the signal template $u(t)$ with the sum of a chain of IIR filters [Cf. Eq. (5.19)], which we denote by $U(t)$:

$$U(t) \equiv \sum_{l=1}^{M} B_l e^{(\gamma_l - i\Omega_l)(t-t_l)}\Theta(t_l - t). \tag{5.27}$$

Here the chain consists of M filters; for filter l ($1 \le l \le M$), B_l is the amplitude of the filter l, Ω_l and γ_l are the angular frequency and decay rate, and t_l is its ending time.

As a first step, let us determine the relevant portion of the signal that we need to approximate: this is bounded by the low frequency cut-off $f_{\rm min}$, below which the chirp only contributes negligible signal-to-noise ratio, as well as the high frequency cut-off $f_{\rm max}$. The minimum frequency $f_{\rm min}$ is normally determined by the seismic wall of the detector which is set to be 40 Hz for initial LIGO, 10 Hz for Advanced LIGO, and might extend to lower frequencies in future detectors, such as the Einstein Telescope (ET). The maximum frequency $f_{\rm max}$ is either determined by the end of the Newtonian chirp or the upper end of the detection band. In this paper we set $f_{\rm max} = 2000\,{\rm Hz}$.

Now suppose our Newtonian chirp has a particular value for the intrinsic parameter A, and $t_c = 0$, $\phi_c = 0$. Let us define $t_0 \equiv t_{\rm ini}$ as the time at which the instantaneous frequency of the waveform is equal to $f_{\rm min}$ (which means $|t_0| = -t_0$ is the duration of the Newtonian chirp from $f_{\rm ini}$ to coalescence), and incrementally define

$$t_l = t_{l-1} + T_l\,, \qquad \left|\frac{1}{2}\ddot{\Phi}(t_l)T_l^2\right| = \epsilon \ll 1\,, \quad l = 1, 2, \ldots \tag{5.28}$$

until we reach t_M, which corresponds to a frequency at or beyond $f_{\rm max}$. These intervals,

$$[t_0, t_1],\ [t_1, t_2],\ \ldots,\ [t_{M-1}, t_M] \tag{5.29}$$

will be the constant-frequency intervals described previously. The parameter ϵ should be substantially less than unity, so that the phase error caused by assuming a constant frequency is significantly less than one radian.

For $t \in [t_{l-1}, t_l]$, we expand $\Phi(t)$ at $t_* = t_l - \alpha T_l$ (where α is an ad hoc parameter to be adjusted later)

$$\Phi(t) \simeq \Phi(t_l^*) + \dot{\Phi}(t_l^*)(t - t_l^*) + \frac{1}{2}\ddot{\Phi}(t_l^*)(t - t_l)^2 \tag{5.30}$$

such that the first term is a constant phase, the second term gives a single angular frequency of $\dot{\Phi}(t_l^*)$, while the third term gives the error of a single-frequency approximation, which will be small if ϵ is small enough in Eq. (5.28). We will then use $\Omega_l \equiv -\dot{\Phi}(t_l^*)$ as the oscillation frequency of the IIR filter assigned for this constant-frequency interval, and prescribe a complex amplitude of

$$B_l \equiv \mathcal{A}(t_l^*)e^{i\Phi(t_l^*) - i\Omega_l(t_l - t_l^*)}\,. \tag{5.31}$$

These will assemble into

$$\begin{aligned} B_l e^{-i\Omega_l(t - t_l)} &= \mathcal{A}(t_l^*)e^{i\Phi(t_l^*) + i\dot{\Phi}(t_l^*)(t - t_l^*)} \\ &\approx \mathcal{A}(t)e^{i\Phi(t)}, \quad t_{l-1} \le t \le t_l\,. \end{aligned} \tag{5.32}$$

We must still add a Heaviside function and a damping component to modify (5.32) into a form realizable by an IIR filter. Since the validity of (5.32) is between t_{l-1} and t_l, it is natural to have the Heaviside function cut off values for $t > t_l$, and to have the damping component have a time constant comparable to T_l, which gradually cuts off the filter at $t \lesssim t_{l-1}$. Prescribing

$$\gamma_l = \zeta/T_l\,, \tag{5.33}$$

with ζ yet another ad hoc parameter, we write

$$\begin{aligned} &U_l(t; A, t_c = 0, \phi_c = 0) \\ \equiv\ &B_l e^{-i\Omega_l(t - t_l) - \gamma_l(t_l - t)}\Theta(t_l - t) \end{aligned} \tag{5.34}$$

which is our IIR filter for interval l, for chirps with parameters A, $t_c = 0$, $\phi = 0$. Summing over all U_l, we obtain an IIR chain that approximates the entire *complex* chirp signal:

$$U(t; A, t_c = 0, \phi_c = 0) = \sum_{l=1}^{M} U_l(t; A, t_c = 0, \phi_c = 0). \tag{5.35}$$

If the sum of the complex filter chain $U(t)$ indeed approximates the complex chirp signal $u(t)$ [Cf. Eq. (5.21)], then the real and imaginary parts of the output from the filter chain will be good approximations for filtering chirps with $\phi_c = 0$ and $\pi/2$, respectively.

For non-zero t_c, we will have to apply

$$U(t; A, t_c, \phi_c = 0) \equiv U(t - t_c; A, t_c = 0, \phi_c = 0) \tag{5.36}$$

Note that having Heaviside Function $\Theta(t - t_c - t_l)$ within U_l means we have to collect the IIR filter result of filter l at $t_l + t_c$. The fact that all t_l are negative means all results are obtained *before* the coalescence (which happens at t_c) and hence IIR filtering itself causes no latency — except for the small latency due to over-whitening, as stated previously (sec. 5.2.2)

5.3.3 Filtering for general signal phases and goodness of match

Since the construction of the IIR filter chain is of an ad hoc nature, we must test how well the resulting IIR filter chain U can approximate the original signal u. A natural candidate would be imposing that the match between the signal u and the template U

$$\rho_{\rm cplx} = \frac{|\langle u|U\rangle|}{\sqrt{\langle u|u\rangle\langle U|U\rangle}} \tag{5.37}$$

must be close to unity.

However, this needs to be connected to the signal-to-noise ratio achievable by IIR filtering. For doing so, we must first elaborate how to use the output of the complex IIR filtering to recover signals with arbitrary phases. If we write

$$u \equiv u_r + iu_i \tag{5.38}$$

with $u_{r,i}$ represent the real and imaginary parts of u in the time domain, and similarly,

$$U \equiv U_r + iU_i\,, \tag{5.39}$$

then the true signal of arbitrary phase is a linear combination of u_r and u_i written as $A_1u_r + A_2u_i$, and we should use a linear combination of the real and imaginary parts of U, namely $B_1U_r + B_2U_i$ as the search template. For any particular coefficients $A_{1,2}$, the optimal overlap is given by

$$\rho_{\rm IIR}(A_1, A_2) = \max_{B_{1,2}} \frac{\langle A_1u_r + A_2u_i|B_1U_r + B_2U_i\rangle}{\sqrt{\langle B_1U_r + B_2U_i|B_1U_r + B_2U_i\rangle}} \tag{5.40}$$

The worst-case scenario is given by a minimization over (A_1, A_2):

$$\rho_{\rm IIR}^{\rm worst} = \min_{A_1,A_2} \frac{\rho_{\rm IIR}(A_1, A_2)}{\sqrt{\langle A_1u_r + A_2u_i|A_1u_r + A_2u_i\rangle}}. \tag{5.41}$$

In fact, when the signal and the template are both highly adiabatic, it can be shown that $\rho_{\rm IIR}(A_1, A_2)$ is approximately independent of $A_{1,2}$, and that to a very good accuracy:

$$\rho_{\rm cplx} \approx \rho_{\rm IIR}^{\rm worst}. \tag{5.42}$$

Eq. (5.41) is therefore used to calculate the goodness of the match of the IIR filter chain.

5.3.4 Implementation for $(1.4 + 1.4)M_\odot$ binaries and initial LIGO

We first apply the prescription described in Sec. 5.3.2 to construct an IIR filter chain for $(1.4{+}1.4)M_\odot$ binaries for initial LIGO and use Eq. (5.41) to test their overlap with the true signals. We choose (by hand) $\alpha = 2.3$, $\epsilon = 0.269$ and $\zeta = 4$, an overlap of 0.99 is achieved with $N_{\rm IIR} = 200$ IIR filters.

We next estimate the computational cost required by such IIR filtering. We focus on the floating point operation count per unit time required to generate complex outputs from the sum of individual IIR filter outputs of Eq. (5.16). Here we assume the maximum sample rate for compact-binary

	Rate	S_k (s^{-1})	16	32	64	128	256	512	1024	2048	4096	8192	N_{tot}	Total Cost
	Type	f/Hz	2 – 4	4 – 8	8 – 16	16 – 32	32 – 64	64 – 128	128 – 256	256 – 512	512 – 1024	>1024		
iLIGO	FIR	$N_{\mathrm{FIR,k}}$					4547	3062	965	304	96	30	9004	20
		$\mathcal{C}_{\mathrm{FIR},k}$					4.7	6.3	4.0	2.5	1.6	1.0		
	IIR	$N_{\mathrm{IIR,k}}$					71	62	34	19	10	4	200	2.4
		$\mathcal{C}_{\mathrm{IIR}}$					0.22	0.38	0.42	0.47	0.49	0.39		
aLIGO	FIR	$N_{\mathrm{FIR,k}}$			45835	30868	9723	3062	965	304	96	30	90883	53
		$\mathcal{C}_{\mathrm{FIR},k}$			11.7	15.8	10.0	6.3	4.0	2.5	1.6	1.0		
	IIR	$N_{\mathrm{IIR,k}}$			220	198	111	62	34	19	10	4	658	3.0
		$\mathcal{C}_{\mathrm{IIR}}$			0.17	0.30	0.34	0.38	0.42	0.47	0.49	0.39		
$\mathrm{ET_B}$	FIR	$N_{\mathrm{FIR,k}}$	213010	311130	98000	30868	9723	3062	965	304	96	40	667198	120
		$\mathcal{C}_{\mathrm{FIR},k}$	13.6	39.8	25.1	15.8	10.0	6.3	4.0	2.5	1.6	1.0		
	IIR	$N_{\mathrm{IIR,k}}$	392	631	353	198	111	62	34	19	11	3	1814	3.3
		$\mathcal{C}_{\mathrm{IIR}}$	0.08	0.24	0.27	0.30	0.34	0.38	0.42	0.47	0.54	0.29		

Table 5.2 Break-down of number of filters and computational cost (over successive two-fold down-sampling channels) of multi-rate FIR and IIR filtering, of a single template for a (1.4+1.4) $M_\odot$ binary for initial, Advanced LIGO and the Einstein Telescope. See text in Sec. 5.3.4. Here computational costs for each type of filtering and for different sampling channels are calculated using Eqs. (5.44)–(5.47), with numerical values quoted in units of MFLOPS or 10^6 FLOPS. The minimum overlap is 0.99.

coalescence data analysis is 8192 Hz, with 2× down-sampling applied successively to provide channels with sample rates of 4096 Hz, 2048 Hz, ..., 256 Hz. The IIR filter bank is divided into 6 groups, each corresponding to a frequency band of 2^{k+5}–2^{k+6} Hz, for $k = 0, 1, ..., 5$. For filters in group k, we assume they are applied to the channel with sample rate of

$$S_k = 2^{k+8}\,\mathrm{Hz}\,. \tag{5.43}$$

In Table 5.2, we list the actual number of IIR filters required to achieve a minimum overlap of 0.99 at different frequency band with downsampling technique. For comparison, we list the corresponding numbers for the FIR method also applied with downsampling technique.

At each time step, each IIR filter needs to perform a total of 12 real-number multiplications and additions namely: 4 real-number multiplications plus 2 real-number additions for multiplying the current output by the complex recursive coefficient, 2 real-number multiplications for multiplying data (second term in Eq. (5.16)) with a complex normalization coefficient to yield proper SNR output, 2 real-number additions for combining the previous two products, while finally 2 real-number additions for adding the result of this filter into the total output.

If we ignore costs for down- and up-sampling, which are performed relatively rarely, the total computational cost for initial-LIGO filters in Table 5.2 is

$$\mathcal{C}_{\mathrm{IIR}} = \sum_{k=0}^{5} 12 S_k N_{\mathrm{IIR,k}} \simeq 2.4 \times 10^6 \mathrm{flops}. \tag{5.44}$$

On the other hand, if we carry out the same down sampling scheme for FIR filtering, the number of points in group 0 will be

$$N_{\mathrm{FIR,0}} = S_0 \cdot [t(64\,\mathrm{Hz}) - t_{\mathrm{ini}}] \tag{5.45}$$

where $t(64\,\mathrm{Hz})$ is the time at which the instantaneous frequency is 64 Hz. For $k = 1, 2, 3, \ldots 5$, we have

$$N_{\mathrm{FIR,k}} = S_k \cdot \left[t(2^{k+6}\,\mathrm{Hz}) - t(2^{k+5}\,\mathrm{Hz})\right] \tag{5.46}$$

At sample rate S_k, for each time step, we have to perform two real-valued correlations with array length $N_{\mathrm{FIR\,k}}$, which cost $4N_{\mathrm{FIR,k}}$ floating point operations. The total computational cost of FIR filtering is therefore

$$\mathcal{C}_{\mathrm{FIR}} = \sum_{k=0}^{5} 4 S_k N_{\mathrm{FIR,k}} \simeq 2.0 \times 10^7 \mathrm{flops}. \tag{5.47}$$

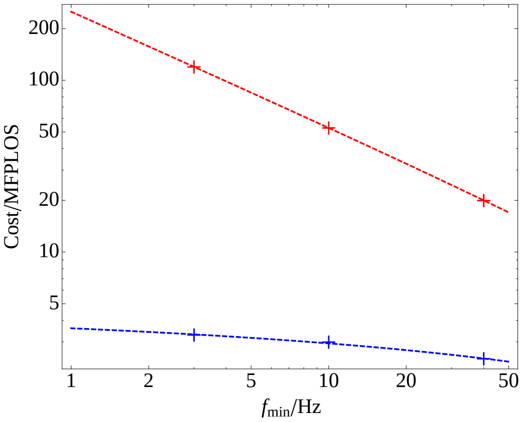

Figure 5.1 Theoretical (dashed curves) and numerical (labeled by "+"'s) scaling of the computational cost with $f_{\min}$ for the FIR (red color) and IIR (blue color) method for one template, fixing $f_{\max} =$ 2000 Hz. The theoretical scaling is based on Eqs. (5.49) and (5.51) (see Sec. 5.3.5.2), numerical values are taken from Table 5.2, column 15.

This is nearly 8 times the cost of the IIR filter method assuming downsampling technique applied to both filtering methods. The result of above cost estimation for the IIR and FIR filtering are also listed in Table 5.2. We will show in the next subsections that the improvement is much more significant for advanced detectors as they venture into lower frequencies.

5.3.5 Dependence on initial frequency and future detectors

As initial frequency $f_{\min}$ is lowered in future gravitational-wave detectors, we anticipate much longer signals (see Table 5.1), and therefore a possibly dramatic increase of computational cost. In this subsection, we will first obtain analytical scalings in IIR and FIR computational costs, assuming an idealized down-sampling scheme. We will then provide more realistic estimates of cost by constructing actual IIR filters and adopting the same successive 2× down-sampling strategy.

5.3.5.1 Analytical estimates

Ideally, the minimum sample rate is twice the instantaneous frequency of the signal, or $S = 2f$. For FIR filters, we have

$$N_{\mathrm{FIR}} \quad \geq \quad 2N_{\mathrm{cyc}} \sim \int_{t_{\mathrm{ini}}}^{t_c} \Omega dt = \int \frac{\Omega}{\dot{\Omega}} d\Omega \sim f_{\min}^{-5/3}\,. \tag{5.48}$$

Converting the summation Eq. (5.47) into integral, we obtain:

$$\mathcal{C}_{\mathrm{FIR}} \sim \int \Omega dN_{\mathrm{FIR}} \sim f_{\min}^{-2/3}. \tag{5.49}$$

For IIR filters, during a dephasing time of $T = \sqrt{2\epsilon/\dot{\Omega}}$, we use one filter $\Delta N_{\mathrm{IIR}} = 1$ and $\Delta\Omega = \dot{\Omega}T = \sqrt{2\epsilon\dot{\Omega}}$, which leads to

$$N_{\mathrm{IIR}} = \int d\Omega \frac{dN_{\mathrm{IIR}}}{d\Omega} = \int \frac{d\Omega}{\sqrt{2\epsilon\dot{\Omega}}} \sim f_{\min}^{-5/6}. \tag{5.50}$$

The computational cost of IIR filtering is

$$\mathcal{C}_{\rm IIR} \sim \int \Omega dN_{\rm IIR} \sim f_{\rm max}^{1/6} - f_{\rm min}^{1/6}. \tag{5.51}$$

Note that for IIR filtering, the positive power law means the computational cost scales predominantly with the higher cut-off frequency, instead of the lower cut-off frequency — we therefore expect the computational cost not to increase dramatically when $f_{\rm min}$ is lowered, if we already have $f_{\rm max} \gg f_{\rm min}$.

5.3.5.2 Numerical estimates

More detailed constructions for Advanced LIGO and Einstein Telescope (ET) have been carried out, following Sec. 5.3.4, assuming $f_{\rm min} = 10\,$Hz for Advanced LIGO and 3 Hz for ET. Assuming the same successive 2× down-sampling strategy, we evaluate the single template computational cost for $(1.4 + 1.4)M_\odot$ binaries for both FIR and IIR filtering. As it turns out, using the same $\epsilon = 0.269$, but $(\alpha, \zeta) = (2.5, 4.25)$ for Advanced LIGO and $(\alpha, \zeta) = (2.25, 4.5)$ for ET, will still give us match above 0.99.

The number of filters in each down-sampling band, as well as computational cost break-down for a single template are shown in the second and third tiers of Table 5.2, for Advanced LIGO and ET, respectively. We also compare our numerical values with scaling laws predicted in Eqs. (5.49) and (5.51), which are plotted in dashed curves in Fig. 5.1. [We determined the normalization of the theoretical formulas using numerical values of computational cost at $f_{\rm min} = 40\,$Hz.] The agreement is remarkable, especially considering that our successive 2-fold down-sampling is not continuous, and therefore rather non-ideal.

As we can see from Table 5.2 and Fig. 5.1, the IIR reduces computational cost from (multi-rate) FIR filtering by factor of 8 for initial LIGO. As we move to lower starting frequencies, the saving factor increases to 18 and 40, respectively. The single-template cost, even when we *extrapolate* $f_{\rm min}$ to the rather unlikely 1 Hz, stays at several MFLOPS.

5.4 Interpolation between IIR filters of Different Inspiral Waveforms

In order to search for all possible kinds of compact binary coalescence, we must match the signal with a *family of templates* parametrized continuously by the parameters of the binary, e.g., their masses. In practice, although maximization of match over certain parameters (e.g., orbital phase of the binary) can be done analytically, for the rest of the parameters, we must sample them discretely, and build a template bank — and match the signal with each member of the bank. The density of the discretization is usually determined by imposing that each member of the continuous family can be approximated well enough by at least one member of the bank, with mismatch less than a maximum tolerable value, $\varepsilon_{\rm max}$.

For advanced detectors, the number of templates can be as large as 10^5 Owen & Sathyaprakash (1999) posing a significant computational challenges. Interpolation strategies have therefore been conceived (e.g., Croce et al. (2000b,a); Mitra et al. (2005); Field et al. (2011)) to *reduce* the number of templates, based on the fact that signal-to-noise ratio is a continuous function of the parameters being searched over. More specifically, if we refer to the bank constructed by imposing the maximum tolerance of mismatch $\varepsilon_{\rm max}$ as the *fine bank*, then the hope is that even if match is *calculated* for a *coarse bank* in which parameters are less densely populated, the signal-to-noise ratio of the fine bank can still be *recovered by interpolation*, in such a way that the total cost of *computing* coarse-bank SNRs plus *interpolating* fine-bank SNRs is less than the cost of directly computing fine-bank SNRs.

Our interpolation method differs from previous work in that we divide each coarse-bank template into several sub-templates in frequency (thus time) domain, and recover fine-bank SNRs using SNRs from the sub-templates. This approach has been inspired by the SVD approach Cannon et al. (2010, 2011a) adopted by the LLOID Cannon et al. (2011c) and the 2-bank interpolation in MBTA Buskulic et al. (2010) methods. We will show that, although the division into sub-templates increases the cost of recombination, it allows a much coarser bank — and finally decreases the computational cost by a large factor.

5.4.1 Template banks in general

To develop a scheme to discretize the parameter space without losing detection efficiency, we must know how much the SNR is reduced by using a template whose parameter values differ from those of the signal. We define the mismatch between two normalized templates of different sets of parameters as

$$\varepsilon \equiv 1 - \langle u(\boldsymbol{\lambda}) | u(\boldsymbol{\lambda'}) \rangle. \tag{5.52}$$

The template u is specified by a parameter vector $\boldsymbol{\lambda}$. If $\boldsymbol{\lambda'}$ is near to $\boldsymbol{\lambda}$, we can Taylor expand ε at $\boldsymbol{\lambda}$ and have the approximation to second order of $\Delta\boldsymbol{\lambda} \equiv \boldsymbol{\lambda'} - \boldsymbol{\lambda}$ as

$$\varepsilon \simeq \frac{1}{2} \frac{\partial^2 \varepsilon}{\partial \lambda_i \partial \lambda_j} \bigg|_{\Delta\boldsymbol{\lambda}=0} \Delta\lambda_i \Delta\lambda_j, \tag{5.53}$$

from which we define a (positive definite) metric in the parameter space

$$\gamma_{ij} \equiv \frac{1}{2} \frac{\partial^2 \varepsilon}{\partial \lambda_i \partial \lambda_j} \bigg|_{\Delta\boldsymbol{\lambda}=0}. \tag{5.54}$$

Equations (5.53) and (5.54) indicates that mismatch between neighboring points in the parameter space can be viewed as distance measured by metric $\boldsymbol{\gamma}$.

Suppose we would like to place a template bank in a D-dimensional parameter space, with a mismatch no higher than ε, then the most straightforward strategy would be laying down a cubic grid with *proper side length dl* measured by the metric γ_{ij}, such that template placed at each grid point will be able to cover a cube whose vertices are centers of neighboring cubes. This means we have

$$D(dl/2)^2 = \varepsilon\,. \tag{5.55}$$

The volume spanned by each cube (according to metric γ_{ij}) is therefore

$$\Delta V = dl^D = (2\sqrt{\varepsilon/D})^D. \tag{5.56}$$

The total number of templates in the bank would be the total volume of the parameter space divided by the volume of each cell, or

$$\mathcal{N} = \frac{V_{\rm tot}}{\Delta V} = \frac{\int d^D\boldsymbol{\lambda} \sqrt{det\|\gamma_{ij}\|}}{(2\sqrt{\varepsilon/D})^D} \tag{5.57}$$

5.4.2 Newtonian chirps

Through the Stationary-Phase Approximation Sathyaprakash & Dhurandhar (1991), the Fourier Transform of a Newtonian Chirp can be written as

$$\tilde{u}(f; A, t_c, \phi_c) \propto f^{-7/6} e^{i(Af^{-5/3} + 2\pi f t_c + \phi_c)},\ f > 0\,, \tag{5.58}$$

and $\tilde{u}(f) = \tilde{u}^*(-f)$ for $f < 0$. The mismatch between two neighboring templates with parameters $(A,\, t_c,\, \phi_0)$ and $(A + \Delta A,\, t_c + \Delta t_c,\, \phi_c + \Delta\phi_0)$ can be written as

$$\varepsilon(\Delta A, \Delta t_c, \Delta\phi_0) = 1 - \frac{\displaystyle\int_{f_{\min}}^{f_{\max}} \frac{f^{-7/3}\cos\Delta\Phi}{S_h(f)} df}{\displaystyle\int_{f_{\min}}^{f_{\max}} \frac{f^{-7/3}}{S_h(f)} df} \tag{5.59}$$

where

$$\Delta\Phi = f^{-5/3}\Delta A + 2\pi f \Delta t_c + \Delta\phi_c \tag{5.60}$$

Expanding Eq. (5.59) up to second order in $\Delta\Phi$, we obtain by comparing with Eqs. (5.53) and (5.54) the metric

$$\|\gamma_{ij}\| = \begin{bmatrix} I(-\frac{17}{3}) & I(-3) & I(-4) \\ * & I(-\frac{1}{3}) & I(-\frac{4}{3}) \\ * & * & I(-\frac{7}{3}) \end{bmatrix}, \tag{5.61}$$

where "$*$" indicates terms obtainable by symmetry, and

$$I(\beta) = \frac{1}{2}\left[\int_{f_{\min}}^{f_{\max}} df \frac{f^{\beta}}{S_h(f)}\right] \Bigg/ \left[\int_{f_{\min}}^{f_{\max}} df \frac{f^{-7/3}}{S_h(f)}\right], \tag{5.62}$$

and we have used $i = 1, 2, 3$ to label ΔA, $2\pi\Delta t_c$ and $\Delta\phi_c$, respectively. Note the metric depends on the frequency division and noise spectral density only.

Here among the three parameters, search over ϕ_c is done analytically, as discussed in Sec. 5.3.3, while search over t_c is carried out systematically at the sample rate — the only parameter left to discretize is A. Therefore, A is an intrinsic parameter as described previously. The correct way to place templates along intrinsic parameter directions is to "project out" the intrinsic parameters, as discussed, e.g., by Owen and Sathyaprakash Owen & Sathyaprakash (1999).

In our case, the projected metric along direction A is one dimensional given by

$$g_{11} = \gamma_{11} - \frac{\gamma_{13}^2\gamma_{22} - 2\gamma_{12}\gamma_{13}\gamma_{23} + \gamma_{12}^2\gamma_{33}}{\gamma_{22}\gamma_{33} - \gamma_{23}^2} \tag{5.63}$$

which depends on $f_{\min}$, $f_{\max}$ and the noise curve S_h through $I(\beta)$. Following Eq. (5.57), the number of templates required to achieve a mismatch ε is then

$$\mathcal{N} = \frac{\sqrt{g_{11}}(A_{\max} - A_{\min})}{2\sqrt{\varepsilon}}, \tag{5.64}$$

where $A_{\min}$ and $A_{\max}$ are the minimum and maximum values of A. Here we can be more specific about template placement along the A direction. Given any A, which is associated with a member of the template bank, and suppose its mismatch with a neighboring template with $A \pm \Delta A$ is $\varepsilon_{\max}$, or

$$g_{11}(\Delta A)^2 = \varepsilon_{\max} \tag{5.65}$$

then neighboring templates should be placed at $A \pm 2\Delta A$, therefore we have

$$\mathcal{N} = \frac{A_{\max} - A_{\min}}{2\Delta A} \tag{5.66}$$

which recovers Eq. (5.64).

Here we give the noise spectral density we use for initial LIGO, Advanced LIGO, and Einstein Telescope ($\mathrm{ET_B}$). For the initial LIGO Abbott et al. (2009), we have $x = f/(150\,\mathrm{Hz})$ and

$$S_h(f) = 9 \cdot 10^{-46}\left[(4.49x)^{-56} + 0.16x^{-4.52} + 0.52 + 0.32x^2\right]. \tag{5.67}$$

For Advanced LIGO LIGO Scientific Collaboration (2009), we have $x = f/(215\,\mathrm{Hz})$ and

$$S_h(f) = 10^{-49}\left[x^{-4.14} - 5x^{-2} + 111\frac{1 - x^2 + \frac{1}{2}x^4}{1 + \frac{1}{2}x^2}\right]. \tag{5.68}$$

Note this is different from what is used in Cannon et al. (2011c). As a result, two methods are dealing with different number of templates for the same parameter space. This should be taken into account when we compare the computational cost of the two methods. For the Einstein Telescope The ET Science Team (2011), we have $x = f/(100\,\mathrm{Hz})$ and

$$\begin{aligned}\sqrt{S_h(f)} = 10^{-25} \quad \Big(& \quad 2.39\times 10^{-27}x^{-15.64} + 0.349x^{-2.145} \\ + & \quad 1.76x^{-0.12} + 0.409x^{1.10}\Big).\end{aligned} \tag{5.69}$$

Applying Eqs. (5.64) and (5.65) to these three detectors, we can show that the number of templates increase by a factor of 3.9 when we upgrade from initial to Advanced LIGO, and another factor of 4.4 when we upgrade from Advanced LIGO to the Einstein Telescope. These numbers are listed in Table 5.1, column 5.

5.4.3 Subtemplates

5.4.3.1 General discussion

Now suppose we divide our entire signal frequency interval, $(f_{\min}, f_{\max})$ into M segments of

$$[f_0, f_1],\ [f_1, f_2],\ \dots\ , [f_{M-1}, f_M], \tag{5.70}$$

with $f_0 = f_{\min}$ and $f_n = f_{\max}$. (When we later apply this to IIR filter chains, M will be much less than the total number of filters, N.) For any template u, we define sub-template u_J, $J = 1, \dots M$, to have the same value as template u within the frequency interval $[f_{J-1}, f_J]$ but have zero values elsewhere,

$$\tilde{u}_J(f) = \begin{cases} \tilde{u}(f), & f_{J-1} \le f \le f_J, \\ 0, & \text{otherwise.} \end{cases} \tag{5.71}$$

Now let us consider two neighboring templates, u and v, their J^{th}-*sub-innerproduct* can be naturally defined as an integral over frequency segment J:

$$\langle u|v\rangle_J \equiv \langle u_J|v_J\rangle = 4\mathrm{Re}\left[\int_{f_{J-1}}^{f_J} df \frac{\tilde{u}^*(f)\tilde{v}(f)}{S_h(f)}\right]. \tag{5.72}$$

This sub-innerproduct can also be regarded as the contribution to the full inner product $\langle u|v\rangle$ from segment J [Cf. Eq. (5.5)], and

$$\langle u|v\rangle = \sum_{J=1}^{M}\langle u|v\rangle_J \tag{5.73}$$

We denote u and $u + \Delta u$ as neighboring templates, and we also define their J^{th}-*sub-mismatch* specific to interval J, in the intrinsic parameter space, as

$$\varepsilon_J \equiv 1 - \frac{\langle u|u+\Delta u\rangle_J}{\sqrt{\langle u|u\rangle_J\langle u+\Delta u|u+\Delta u\rangle_J}}, \tag{5.74}$$

which is equal to the “ordinary” mismatch between u_J and $u_J + \Delta u_J$ as defined in Eq. (5.52). Up to second order in Δu, we can show that the total mismatch and the J^{th}-sub-mismatch are

$$\varepsilon = \frac{1}{2}\frac{\langle \Delta u|\Delta u\rangle}{\langle u|u\rangle} \tag{5.75}$$

$$\varepsilon_J = \frac{1}{2}\frac{\langle \Delta u|\Delta u\rangle_J}{\langle u|u\rangle_J} \tag{5.76}$$

Using Eq. (5.73), we can show that

$$\varepsilon = \sum_{J=1}^{M} \varepsilon_J \frac{\langle u|u\rangle_J}{\langle u|u\rangle}. \tag{5.77}$$

Since

$$\sum_{J=1}^{M} \frac{\langle u|u\rangle_J}{\langle u|u\rangle} = 1, \tag{5.78}$$

the overall mismatch is therefore a weighted average of the sub-mismatches. This means to achieve an overall mismatch of ε, we only need to make sure the sub-mismatches ε_J average to ε. This has dramatic implications in the sense that it allows the overall mismatch to be maintained by (1) dividing the frequency band into several frequency intervals with non-uniform sub-mismatches, (2) reducing the size of frequency intervals to allow larger step size for intrinsic parameters. These lay the foundation for our template interpolation method.

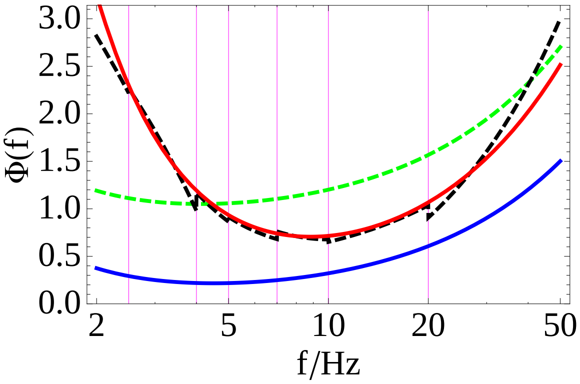

Figure 5.2 Illustration of the phase function $\Phi(f)$ vs frequency for the presumed parameter A (blue solid line) and its neighboring parameter $A+\Delta A$ (red line), the linear shift of the blue line to match the red line (green dashed line), and a piecewise approximation (black dashed line) of the red line by shifting segments from the blue line. It shows that with smaller frequency intervals, it is easier to match phases arising from different intrinsic parameters.

To qualitatively understand the reason that the grid size for intrinsic parameter placement can be enlarged when we restrict ourselves to smaller frequency intervals, we first note that in the frequency domain, it is the phase that we need to match, while the amplitude as a function of frequency is the same for all parameters. We note that the phase of $\tilde{u}(f)$, which we denote by $\Phi(f)$, is determined by A, as well as t_c and ϕ_c (Eq. (5.58)). In Fig. 5.2, we plot the phase $\Phi(f)$ for a particular set of parameters (A, t_c, ϕ_c) in blue and also for a neighboring set of parameters $(A+\Delta A, t_c, \phi_c)$ in red. If we were to use the template with parameter A to search for a signal with parameter $A+\Delta A$, we could shift ϕ_c and t_c used in the search, which corresponds to shifting the blue curve by a linear function in frequency. The green dashed line illustrates a reasonably optimal attempt — yet the difference between the green curve and the red curve cannot be reconciled very well due to the fact that linear functions do not correct for curvature. However, if we divide the frequency range into several intervals, and allow different values of Δt_c and $\Delta\phi_c$ to be applied to each interval, then sub-templates with A can achieve rather low sub-mismatches with signal with $A+\Delta A$. This corresponds to the fact that a curve can be better approximated by straight lines when divided into smaller intervals.

5.4.3.2 Newtonian chirp in the frequency domain

Let us now focus on a particular frequency segment J, with $f_{J-1} \le f \le f_J$, and work out the relation between ΔA and ε_J, as $\Delta\phi_c$ and Δt_c are allowed to readjust their values (to be different from other segments). This simply requires us to repeat the procedure in Sec. 5.4.2 for each segment: with ΔA, Δt_c and $\Delta\phi_c$, we have the J^{th}-sub-mismatch of

$$\varepsilon_J = \left[\begin{array}{ccc} \Delta A & 2\pi\Delta t_c & \Delta\phi_c \end{array}\right] \boldsymbol{\gamma}^J \left[\begin{array}{c} \Delta A \\ 2\pi\Delta t_c \\ \Delta\phi_c \end{array}\right] \tag{5.79}$$

with

$$\boldsymbol{\gamma}^J \equiv \left[\begin{array}{ccc} I_J(-\frac{17}{3}) & I_J(-3) & I_j(-4) \\ * & I_J(-\frac{1}{3}) & I_j(-\frac{4}{3}) \\ * & * & I_J(-\frac{7}{3}) \end{array}\right]. \tag{5.80}$$

and

$$I_J(\beta) \equiv \frac{1}{2}\left[\int_{f_{J-1}}^{f_J} \frac{df\, f^{\beta}}{S_h(f)}\right] \Big/ \left[\int_{f_{J-1}}^{f_J} \frac{df\ f^{-7/3}}{S_h(f)}\right]. \tag{5.81}$$

Note that the above are identical to Eqs. (5.59)–(5.61), except with integrations restricted to the interval of $[f_{J-1}, f_J]$.

The next step is similar to the "projection" process described by Owen and Sathyaprakash, but restricted to interval J. With Eq. (5.79), we ask the following question: if we are allowed to freely re-adjust individually the values of Δt_c and $\Delta\phi_c$ for interval J of the template (i.e., the J^{th}-subtemplate), what would be the J^{th}-sub-mismatch achievable for ΔA, and what should the corresponding $\Delta\phi_c$ and Δt_c be.

The answer to the question is readily obtainable by a maximization of the mismatch ε over Δt_c and $\Delta\phi_c$, fixing ΔA. This results in adjustments of

$$\left[\begin{array}{c} 2\pi\Delta t_c^J \\ \Delta\phi_c^J \end{array}\right] = -\left[\begin{array}{cc} \gamma_{22}^J & \gamma_{23}^J \\ \gamma_{32}^J & \gamma_{33}^J \end{array}\right]^{-1} \left[\begin{array}{c} \gamma_{12}^J \\ \gamma_{13}^J \end{array}\right] \Delta A \tag{5.82}$$

which result in the J^{th} sub-mismatch of

$$\varepsilon_J = g_{11}^J (\Delta A)^2\,, \tag{5.83}$$

with

$$g_{11}^J \equiv \gamma_{11}^J - \frac{[\gamma_{13}^J]^2\gamma_{22}^J - 2\gamma_{12}^J\gamma_{13}^J\gamma_{23}^J + [\gamma_{12}^J]^2\gamma_{33}^J}{\gamma_{22}^J\gamma_{33}^J - [\gamma_{23}^J]^2}. \tag{5.84}$$

Following Eq. (5.77), we have the total mismatch

$$\varepsilon = g_{11}^{\mathrm{eff}} (\Delta A)^2\,, \tag{5.85}$$

where

$$g_{11}^{\mathrm{eff}} = \sum_J \frac{g_{11}^J \langle u|u\rangle_J}{\langle u|u\rangle} \tag{5.86}$$

is an *effective metric coefficient* for any division of the frequency band. More specifically, g_{11}^{eff} describes the mismatch achievable by individually adjusting $\Delta\phi_c^J$ and Δt_c^J, for each interval of the division. It can be shown that in general a finer division of frequency intervals always gives a smaller

g_{11}^{eff}. As a consequence, if we define

$$\Delta A_{\mathrm{cb}} = \sqrt{\frac{\varepsilon_{\mathrm{max}}}{g_{11}^{\mathrm{eff}}}}\,, \tag{5.87}$$

with the subscript "cb" indicating coarse bank, then ΔA_{cb} will be greater than ΔA given by Eq. (5.65) where g_{11} is evaluated using the full frequency band. In order to make a distinction, we shall rewrite that same equation as

$$\Delta A_{\mathrm{fb}} = \sqrt{\frac{\varepsilon_{\mathrm{max}}}{g_{11}}}\,, \tag{5.88}$$

but adding a subscript "fb" to indicate the fine bank. In order to maximize ΔA_{cb} for a maximum mismatch $\varepsilon_{\mathrm{max}}$, we should simply minimize g_{11}^{eff} globally, over all possible frequency division schemes. Because a template at A in the fine bank covers $(A - \Delta A_{\mathrm{fb}}, A + \Delta A_{\mathrm{fb}})$, the ratio of the number of templates in the coarse bank to that of the fine bank is,

$$\frac{\mathcal{N}_{\mathrm{cb}}}{\mathcal{N}_{\mathrm{fb}}} = \sqrt{\frac{g_{11}^{\mathrm{eff}}}{g_{11}}} \tag{5.89}$$

In summary, given a required maximum mismatch $\varepsilon_{\mathrm{max}}$ with a particular frequency subdivision, by adjusting $\Delta\phi_c^J$ and Δt_c^J individually, a single template at A can cover the region $(A - \Delta A_{\mathrm{cb}}, A + \Delta A_{\mathrm{cb}})$. For a signal with $|\Delta A| \le \Delta A_{\mathrm{cb}}$, the J^{th}-sub-template for parameter $A + \Delta A$ can be constructed by adjusting Δt_c^J and $\Delta\phi_c^J$ of the sub-template of template A using Eq. (5.82). The interpolated template of parameter $A + \Delta A$ is therefore the sum of the constructed sub-templates from a coarse-bank template A

$$\begin{aligned}
&\tilde{u}(f; A + \Delta A, t_c, \phi_c) \\
&= \sum_{J=1}^{M} \tilde{u}_j(f; A, t_c + \Delta t_c^J(\Delta A), \phi_c + \Delta\phi_c^J(\Delta A)) \\
&= \sum_{J=1}^{M} \tilde{u}_j(f; A, t_c, \phi_c) e^{i2\pi f \Delta t_c^J(\Delta A) + i\Delta\phi_c^J(\Delta A)}.
\end{aligned} \tag{5.90}$$

It is straightforward to establish the following properties of the effective metric: (i) g_{11}^{eff} always becomes smaller when we insert one or more dividing frequencies into an existing division of $[f_{\mathrm{min}}, f_{\mathrm{max}}]$, (ii) if we continue to decrease the maximum size of intervals, we can decrease g_{11}^{eff} indefinitely [in fact, for small intervals, g_{11}^J scales as $(\Delta f)^5$, which means g_{11}^{eff} should scale as $(\Delta f)^4$, and hence ΔA scales as $(\Delta f)^{-2}$]. Furthermore, for template families with *more than one parameter*, it is straightforward to generalize our result to

$$g_{ab}^{\mathrm{eff}} = \sum_J \frac{g_{ab}^J \langle u|u\rangle_J}{\langle u|u\rangle} \tag{5.91}$$

with the number of templates in the coarse bank given by

$$\frac{\mathcal{N}_{\mathrm{cb}}}{\mathcal{N}_{\mathrm{fb}}} = \sqrt{\frac{\det\|g_{ab}^{\mathrm{eff}}\|}{\det\|g_{ab}\|}} \tag{5.92}$$

5.4.4 Application to IIR filtering technique

In this section, we will apply the formalism developed in the previous subsection and discuss how we can implement IIR filter chains only for a much coarser bank of templates — while still obtaining SNRs for the entire fine template bank. Discussions made in the previous sections, although strictly

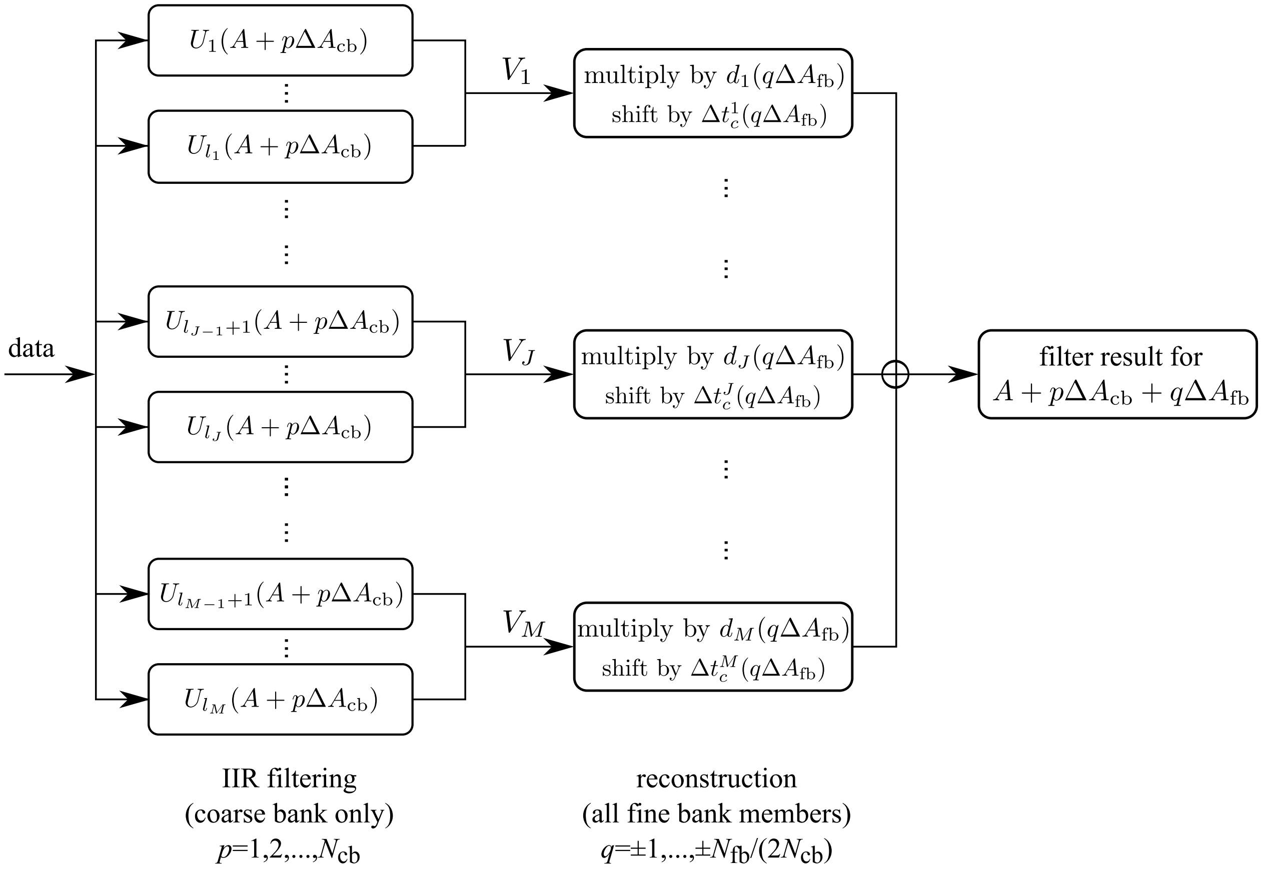

Figure 5.3 Schematic diagram of the IIR filtering process for a template with parameter $A+p\Delta A_{\mathrm{cb}}+q\Delta A_{\mathrm{fb}}$. The first part is the IIR filtering for a member of the coarse bank, $A+p\Delta A_{\mathrm{cb}}$, which produces a range of filter outputs, labeled by $U_1 \ldots U_{l_M}$. These are grouped into M groups of summed IIR results $V_1, \ldots, V_M$. The result for $A+p\Delta_{\mathrm{cb}}+q\Delta A_{\mathrm{fb}}$ is obtained by combining these V_J's after each one is multiplied by $d_J(q\Delta A_{\mathrm{fb}})$ and shifted by $\Delta t_c^J(q\Delta A_{\mathrm{fb}})$. The entire data analysis process still computes N_{fb} filter results, by including N_{cb} possible p's and $N_{\mathrm{fb}}/N_{\mathrm{cb}}$ possible q's for each p. [In the special case of $q=0$, the V_J's are directly summed without having to go through multiplications and time shifts.] The downsampling or upsampling process is not shown.

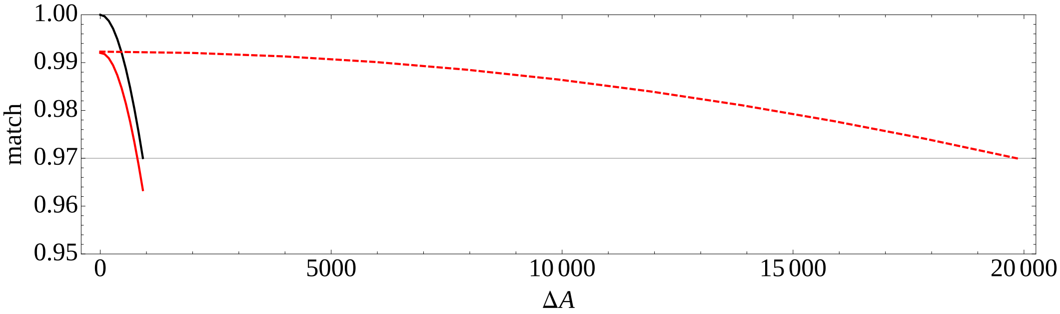

Figure 5.4 Matches achievable with a Newtonian-Chirp signal at $A+\Delta A$, by various templates built for A, using initial LIGO noise spectral density for a (1.4+1.4)$M_\odot$ NS-NS binary. Black solid curves corresponds to the result for a Newtonian-Chirp template, therefore the match is equal to unity at $\Delta A = 0$. Red solid curve corresponds to that using IIR filters, while red dashed curve corresponds to the interpolated match that can be recovered by using 6 filter subgroups.

speaking only apply to sharp divisions in the signal frequency band, still qualitatively apply to IIR filters that work in time-domain. The trick is to replace *frequency intervals* in the previous section by *groups of IIR filters*. This approach will work as long as we include enough number of filters in each "group", so that overlaps between different groups are relatively unimportant. We note that, as is the case for the construction of IIR filter chains, the construction of the interpolation scheme by itself does not justify its efficiency — a separate test of achievable match will be carried out explicitly after the interpolation scheme is constructed.

To be more specific, we re-group the entire chain of N IIR filters into m sub-groups, with group J including those whose oscillation frequency lies within the frequency interval J defined in Sec. 5.4.3. In other words, group J of IIR filters can be written as

$$\begin{aligned} & V_J(t; A, t_c, \phi_c) \\ = & \sum_{\frac{\Omega_l}{2\pi}\in[f_{J-1},f_J]} U_l(t; A, t_c, \phi_c) \\ \equiv & \sum_{l=l_{J-1}+1}^{l_J} U_l(t; A, t_c, \phi_c), \quad J = 1, \ldots, M\,, \end{aligned} \tag{5.93}$$

where we have $l_0 = 0$. We will treat V_J as corresponding to the $\tilde{u}_J(f; A, t_c, \phi_c)$ of Sec. 5.4.3. As a consequence, from Eqs. (5.82) and (5.90), signal $u(t; A+\Delta A, t_c, \phi_c)$ can be interpolated by the IIR filters constructed for $u(t; A, t_c, \phi_c)$

$$\begin{aligned} & u(t; A+\Delta A, t_c, \phi_c) \\ \simeq & \sum_{J=1}^{M} V_J(t; A, t_c + \Delta t_c^J, \phi_c + \Delta\phi_c^J) \\ = & \sum_{J=1}^{M} e^{i\Delta\phi_c^J} V_J(t; A, t_c + \Delta t_c^J, \phi_c)\,. \end{aligned} \tag{5.94}$$

Here Δt_c^J and $\Delta\phi_c^J$ should be computed from ΔA using Eq. (5.82).

In practice we can easily generalize the coefficients in front of V_J to further reduce the overall mismatch, by using a slightly more general reconstruction formula:

$$u(t; A+\Delta A, t_c, \phi_c) \simeq \sum_{J=1}^{m} d_J V_J(t; A, t_c + \Delta t_c^J, \phi_c), \tag{5.95}$$

	S_k (s^{-1})	16	32	64	128	256	512	1024	2048	4096	8192	Cost Total
	f/Hz	2 – 4	4 – 8	8 – 16	16 – 32	32 – 64	64 – 128	128 – 256	256 – 512	512 – 1024	1024 –	
iLIGO	$N_{\mathrm{group},k}$					1	2	1	1		1	0.10
	$\{f_J\} \cap (f_{k-1}, f_k]$					52.9	71.0, 97.3	141	244		2000	
	$\mathcal{C}_{\mathrm{recomb},k}$					0.002	0.008	0.008	0.016		0.066	
aLIGO	$N_{\mathrm{group},k}$			1	3	2	2	1			1	0.090
	$\{f_J\} \cap (f_{k-1}, f_k]$			12.9	16.8, 22.1 29.6	40.1, 55.2	78.5, 122	228			2000	
	$\mathcal{C}_{\mathrm{recomb},k}$			0.0005	0.003	0.004	0.008	0.008			0.066	
ET$_{\mathrm{B}}$	$N_{\mathrm{group},k}$		2	2	2	1	1	1			1	0.083
	$\{f_J\} \cap (f_{k-1}, f_k]$		5.1, 6.9	9.3,12.8	17.8, 25.3	37.4	60.3	122			2000	
	$\mathcal{C}_{\mathrm{recomb},k}$		0.0005	0.001	0.002	0.002	0.012	0.008			0.066	

Table 5.3 Break-down of recombination cost required for obtaining one fine-bank template using the interpolation method, for initial, Advanced LIGO and the Einstein Telescope — assuming a successive two-fold down-sampling and ignoring the cost of down- and up-sampling. The IIR filter information is listed in Table 5.2. For each down-sampling channel, we list the number of filter groups, as well as each of their upper-bound frequency (i.e., f_J for group J), and the computational cost as computed by Eq. (5.99). Computational cost here is measured by MFLOPS, or 10^6 FLOPS.

where d_J are complex coefficients that depend on ΔA, given by

$$d_J = \sum_K T^{-1}_{JK} \langle V_K(A, t_c, \phi_c) | u(A + \Delta A, t_c, \phi_c) \rangle \tag{5.96}$$

with the matrix $\mathbf{T}$ given by

$$T_{JK} = \langle V_J(A, t_c, \phi_c) | V_K(A, t_c, \phi_c) \rangle \tag{5.97}$$

5.4.5 Full computational cost

Fig. 5.3 illustrates the procedure of obtaining the outputs from IIR filter chain for fine-bank coverage by interpolating coarse-bank filter outputs described previously. Upon obtaining outputs from subgroups of IIR filters for the *coarse bank*, we need to reconstruct outputs for all members of the *fine bank*. We hereby estimate the cost for reconstruction. Let's assume that a member of the fine bank that is *not* a member for the coarse bank is ΔA away from a coarse-bank template A. For this ΔA, we need to go through each group J of filters, take the total output of this group (which corresponds to filtering by V_J), multiply it by the complex number d_J (6 floating-point operations) and shift in time by Δt_c^J, and then add it to the sum (2 floating-point operations). The output eventually yields the SNR corresponding to the member of the fine bank. Note that both d_J and Δt_c^J are functions of ΔA, but they do not need to be recalculated for each time step.

Assuming our frequency division is made in a way such that each filter group has the same sample rate (S_J for group J), then the total recombination cost is

$$\mathcal{C}_{\mathrm{recom}} = \sum_J 8 S_J \, . \tag{5.98}$$

In language of Sec. 5.3.4, if we assume there are $N_{\mathrm{group},k}$ IIR filter groups for each down-sampling channel, then the recombination cost can also be written as

$$\mathcal{C}_{\mathrm{recom}} = \sum_k 8 S_k N_{\mathrm{group},k} \, . \tag{5.99}$$

As a consequence, assuming that $\Delta A_{\rm cb} = R\Delta A_{\rm fb}$, we have a total cost of

$$\begin{aligned}\mathcal{C}_{\rm total} &= \mathcal{N}_{\rm fb}\left[\frac{\mathcal{C}_{\rm IIR}}{R} + \left(1-\frac{1}{R}\right)C_{\rm recom}\right] \\ &\approx \mathcal{N}_{\rm fb}\sum_k\left[\frac{12N_{{\rm IIR},k}}{R} + 8N_{{\rm group},k}\right]S_k\,, \qquad (5.100)\end{aligned}$$

with the approximation valid when $R \gg 1$. In this case, we can have a good estimate of the computational cost of IIR filtering with interpolation. For a coarse bank with density $1/R$ the fine bank, filtering cost naturally decreases to $1/R$ of the cost of conventional IIR filtering without interpolation. The cost of recombination can be estimated with a simple rule: for each sample rate, the cost of recombination is about $2/(3\bar{n}_k)$ times that of conventional IIR filtering, where

$$\bar{n}_k \equiv \frac{N_{{\rm IIR},k}}{N_{{\rm group},k}} \qquad (5.101)$$

is the average number of IIR filters in groups at the k-th sample rate. As a consequence, the total cost of the IIR filtering with interpolation scheme including recombination can be lowered significantly if we achieve a balance of $R \gg 1$ and $\bar{n} \gg 1$. Note larger R means larger coarse-bank grid size ΔA_{cb} for a fixed ΔA_{fb}. This is achieved by introducing finer frequency intervals. On the other hand, finer frequency intervals means more IIR groups $N_{\rm group}$ or smaller $\bar{n}$ within each down-sampling channel.

The computational cost for performing down- or up-sampling is implementation-dependent (see discussions in Cannon et al. (2011c)). They are not included in our calculation for simplicity. We only need to perform data downsampling once for all templates, so the cost should be negligible compared to the total cost. The upsampling process is needed at least for each coarse-bank template, but only for filter group outputs. Note the number of filter groups is much smaller than the total number of the IIR filters. Depending on the type of upsampling filters, the upsampling cost can be negligible compared to the total cost, but can also be in similar orders as the recombination cost. This requires further investigation.

5.4.6 Implementation for initial, Advanced LIGO and Einstein Telescope

We first investigate the case of initial LIGO to demonstrate the feasibility of our interpolation method. Taking into account the fact that even the optimal match between IIR filter and the real signal is not unity, we need to place the fine-bank IIR template a little denser than that from theoretical waveform. Theoretically for the Newtonian waveform, we have $\Delta A_{\rm fb} = 923$ (in units of $s^{-5/3}$) to have a minimum match of 0.97 for templates based on the signal waveform. For the IIR filter bank, we need a smaller spacing of $\Delta A_{\rm fb}^{\rm IIR} = 800\ s^{-5/3}$ in order for the bank to achieve the same match between an IIR template and the signal at $A + \Delta A_{\rm fb}^{\rm IIR}$. Fig. 5.4 shows numerically calculated match as a function of template spacing ΔA for templates from the signal waveform (black solid line) and for the IIR filters (red solid line) for the case of (1.4+1.4) $M_\odot$ binary. Note that the numbers of fine-bank templates here are slightly different from those given in Table 5.1, as we use slightly different overlap and also we use numerically evaluated matches here, instead of ones computed analytically assuming high match (in Sec. 5.4.2).

To test the coarse-bank template placement, for simplicity, we restrict ourselves with the case of subdividing the frequency band into a total of six segments (or equivalently, six IIR filter groups in the time domain). According to the idealized theoretical calculations in frequency domain (Sec. 5.4.3.2), the optimal frequency subdivision predicts $\Delta A_{\rm cb}/\Delta A_{\rm fb} \approx 26$ for a minimum match of 0.97. This calculation has assumed high match, and divides signals into parts that are strictly localized within separate frequency bands. On the other hand, the numerical result using interpolation method on the IIR filter groups in the time domain (as prescribed in Sec. 5.4.4) reveals that we can relax the coarse-bank spacing up to $\Delta A_{\rm cb}^{\rm IIR} = 19845\ {\rm s}^{-5/3}$ (dashed curve in Fig. 5.4), meaning

$$\frac{\Delta A_{\rm cb}^{\rm IIR}}{\Delta A_{\rm fb}^{\rm IIR}} \approx 25. \tag{5.102}$$

This is in very good agreement with the idealized prediction. Fig. 5.4 shows in dashed line the numerical result of the match as function of ΔA for the interpolated IIR filtering method.

We can now evaluate the total computational cost of the entire filtering-reconstruction process. For filtering, since we only have

$$\mathcal{N}_{\rm c} = (A_{\rm max} - A_{\rm min})/(2\Delta A_{\rm cb}^{\rm IIR}) = 92 \tag{5.103}$$

templates in the coarse bank [1], and the cost for each full filtering is 2.4 MFLOPS (see Table 5.2), the cost of IIR filtering is $\mathcal{C}_{\rm IIR}^{\rm bank} = 221\,{\rm MFLOPS}$. Since the number of templates in the fine bank is

$$\mathcal{N}_{\rm f} = (A_{\rm max} - A_{\rm min})/(2\Delta A_{\rm fb}^{\rm IIR}) = 2281\,, \tag{5.104}$$

while the reconstruction cost for each member is 0.10 MFLOPS, the total cost for reconstruction (for members in the fine bank but not already in the coarse bank) is 228 MFLOP. Therefore the total cost for searching for Newtonian Chirps in initial LIGO is 449 MFLOPS, or 0.5 GFLOPS.

We carry out the same procedure for Advanced LIGO and $\rm ET_B$, with frequency division information listed in Table 5.3, and interpolation factor as well as break-down of filtering and recombination costs listed in Table 5.4. As we can read from Table 5.4, the computational power required for a real-time search of Newtonian Chirps, using IIR filters and interpolation, in initial, Advanced LIGO and ET are 0.5 GFLOPS, 1.2 GFLOPS and 4.4 GFLOPS, respectively. The scaling of cost with $f_{\rm min}$ is rather mild as expected, and the cost, even for ET, seems very manageable.

In summary, it seems possible that to search for tens to hundreds of thousands of fine-bank templates for advanced LIGO or ET, we can have the entire search done with a few desktop computers and fewer if other acceleration technique such as the Graphics Processing Unit Chung et al. (2010b,a) can be adopted. While our result is based on the Newtonian chirp, this outcome should be applicable to Post-Newtonian (PN) cases. Note the low-latency pipeline LLOID with the FIR scheme in combination with downsampling and SVD technique Cannon et al. (2011c, 2010) also predicts manageable computing power for Advanced LIGO. MBTA method Buskulic et al. (2010), on the other hand, can already perform network analysis to search for inspiral signals using PN waveforms with a few CPUs for the initial LIGO. How it scales with advanced detectors while maintaining low latency remains to be investigated (see also Sec. 5.5 for a comparison of frequency vs time domain method). The integration of the time-domain IIR filtering method with the infrastructure of the LLOID pipeline is currently under way. Preliminary result for the application of the IIR filterbank method to PN waveforms can be found in Hooper et al. (2010) and Hooper et al. (2011).

5.5 Time Domain vs Frequency Domain Approach

5.5.1 General consideration

In terms of template interpolation, the ideas to divide the template into segments in the time or frequency domain are equivalent in mathematics – both trying to represent the template by the superposition of a complete basis of the continuous real-value function space on real axis. The functions in the basis are much simpler than the template, and thus easier to deal with. We can improve the computational efficiency by processing the basis functions first and then superpose them in the right way to get the result for a template. Given that the data we get from the detector is in the time domain, the advantage of working in the time domain is that we can avoid procedures required to transform the data into frequency domain (e.g., data accumulation in Fourier transformation)

---

[1] Recall that since match between template at A and signal at $A + \Delta A$ is already satisfactory, the next template needs to be placed at $A + 2\Delta A$.

	$\Delta A^{\mathrm{IIR}}_{\mathrm{fb}}$	$\mathcal{N}_{\mathrm{fb}}$	$\Delta A^{\mathrm{IIR}}_{\mathrm{cb}}$	$\mathcal{N}_{\mathrm{cb}}$	$\mathcal{C}_{\mathrm{IIR}}$	$\mathcal{C}^{\mathrm{total}}_{\mathrm{IIR}}$	$\mathcal{C}_{\mathrm{recomb}}$	$\mathcal{C}^{\mathrm{total}}_{\mathrm{recomb}}$	$\mathcal{C}_{\mathrm{total}}$	$\mathcal{C}_{\mathrm{total}}/\mathcal{C}^{\mathrm{fb}}_{\mathrm{total}}$
iLIGO	800	2281	19845	92	2.4	221	0.10	228	449	0.082
aLIGO	255	7156	10500	174	3.0	522	0.090	628	1150	0.054
ET	70	26069	2713	673	3.3	2221	0.083	2108	4329	0.050

Table 5.4 Break-down of total computational cost in MFLOPS in searching for Newtonian Chirps in initial LIGO, Advanced LIGO and ET, assuming interpolation for inspirals of 1–3 $M_{\odot}$ individual masses. Here we list numbers of templates in both the fine ($\mathcal{N}_{\mathrm{fb}}$) and coarse banks ($\mathcal{N}_{\mathrm{cb}}$), the computational cost for each full IIR chain ($\mathcal{C}_{\mathrm{IIR}}$, taken from Table 5.2), as well as the recombination cost for each template ($\mathcal{C}_{\mathrm{recomb}}$, taken from Table 5.3). We then give the total IIR filtering cost ($\mathcal{C}^{\mathrm{total}}_{\mathrm{IIR}}$), the total recombination cost ($\mathcal{C}^{\mathrm{total}}_{\mathrm{recomb}}$), and the grand total cost. We also list the ratio $\mathcal{C}_{\mathrm{total}}/\mathcal{C}^{\mathrm{fb}}_{\mathrm{total}}$, in which $\mathcal{C}^{\mathrm{fb}}_{\mathrm{total}}$ represents computational cost for the full bank without using interpolation.

and easily achieve low time latencies. On the other hand, working in frequency domain allows us to easily combine the algorithm with down sampling technique and reduce the number of templates.

The frequency-domain template interpolation technique, e.g., that used in MBTABuskulic et al. (2010), usually uses Heaviside function to cut the template. So the template can be superposed smoothly in the frequency domain while in the time domain the joint of different basis functions can be quite crude. This means that those methods with this technique could easily take advantages of working in the frequency domain, but not both in the time and frequency domain without substantial additional cost in computation.

Our algorithm, with IIR filters working in the time domain and template interpolation designed from the frequency domain, takes advantages of the benefits from both the time and frequency domain approach. Because we use a relatively smooth cut in both domains, we can both achieve low latency in the time domain and reduce the total number of templates while taking advantages of the down sampling technique.

5.5.2 Comparison of computational efficiency

When latencies of the analysis are not in concern, the frequency domain implementation of the cross correlation of data with templates (Eq. 5.11) is probably the most computationally efficient approach. This is due to the use of Fast Fourier Transform technique that has $O(N \log N)$ operation count (N is the number of data points) as compared to the $O(N^2)$ operation count for the FIR method described previously. On the other hand, the operation count of the IIR filterbank method is $O(N)$ but multiplied with a coefficient directly related to the possibly large number of filters needed to achieve a desired match to the chirp signal. Here we take latencies into consideration and compare the computational efficiency of the FFT-based method with the proposed IIR method.

To obtain low-latencies for the FFT-based matched filtering prescribed in Eq. (5.11), the most straightforward approach is to analyze data in overlapping segments. We consider the analysis of equal-length segments of duration T_{stretch} as shown in Fig 5.5 with the duration of overlap equal to that of the longest signal, and the rest termed T_{latency}, that is,

$$T_{\mathrm{stretch}} = T_{\mathrm{longest}} + T_{\mathrm{latency}}. \tag{5.105}$$

Here we assume the same strategy as in the current GW search pipeline where FFTs are performed with fixed length that accommodates the longest signal to ensure the coverage of signals of all possible duration. Note in practice, longer T_{stretch} might be needed to take into account of the windowing effect of the FFTs and issues like the sharp notch filter problems due to lines in the noise power spectrum Allen et al. (2005). For each data stretch, the output of Eq. (5.11) has also the duration T_{stretch}, but due to the wrap-around effect of FFTs, only outputs (for signals with ending time) within the last T_{latency} are valid. This means that to obtain a valid output of duration T_{latency}, a data stretch of at least $T_{\mathrm{longest}} + T_{\mathrm{latency}}$ needs to be processed.

The requirement to perform filtering in real-time implies that the entire analysis needs to be completed within T_{latency} seconds. The minimum total number of real multiplications and real

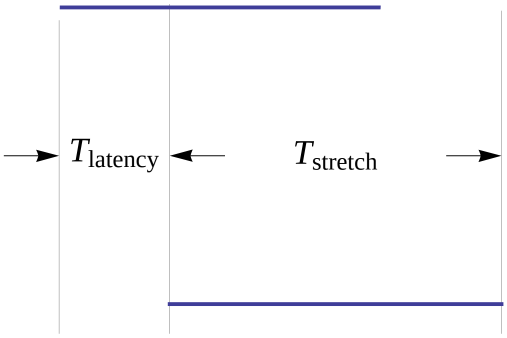

Figure 5.5 Analysis with overlapping data segments. The two horizontal lines represent two adjacent data stretches used for FFT. The lower data segment starts data accumulation with a delay of T_{latency} relative to the upper one. The duration of the overlap between the two stretches is that of the longest signal in the template bank (see text in Sec. 5.5.2).

additions for the FFT algorithm is about $4N\log_2 N$ Johnson & Frigo (2007); Lundy & van Busbirk (2007). Therefore the minimum computational cost in terms of FLOPS for each template for a real-time FFT-based matched filtering is at least,

$$\mathrm{C}_{\mathrm{FFT}} = \frac{4S \cdot T_{\text{stretch}} \log_2(S \cdot T_{\text{stretch}})}{T_{\text{latency}}}, \tag{5.106}$$

where S is the data sampling rate. Here we assume a uniform sampling rate.

In the FFT method, the actual delay T_{delay} between the end time of a GW signal and the event triggering depends on where the signal lies in the data stretch. The longest delay occurs when the ending time of a signal lies $(T_{\text{latency}} - dt)$ before the end of a data stretch where $dt \equiv 1/S$ is the sampling interval. In this case, after the signal ends, it takes the segment further $(T_{\text{latency}} - dt)$ time to finish accumulating data, and then another T_{latency} to be processed, resulting in a delay of,

$$T_{\text{delay}}^{\text{FFT,worst}} = 2T_{\text{latency}} - dt \approx 2T_{\text{latency}} \tag{5.107}$$

The shortest latency is achieved when the ending time of a signal lies just at the end of the data stretch, in which case the waiting time for the data to be analyzed is zero and the delay time of obtaining the trigger is simply the analysis time,

$$T_{\text{delay}}^{\text{FFT,best}} = T_{\text{latency}}. \tag{5.108}$$

Therefore, for the FFT method, the delay time between the end of the signal and the event triggering is about 1–2 times of T_{latency}. Although in previous LIGO inspiral search pipelines T_{latency} is usually chosen so that adjacent data stretches are overlapped by 50%, it can be chosen so that T_{latency} is much smaller, meaning data segments are analyzed with larger overlaps and higher computational cost.

In comparison, for the IIR method, every new data point will be processed immediately when it is available. The delay time between the end of the signal and the triggering time can therefore in principle be as small as the data sampling interval. For real-time processing, the analysis time of the IIR filters at each time step should also be within one sampling interval, dt. As discussed previously, for each output of an IIR filter in (5.16), a total of 12 floating point operations are needed. Hence to produce the IIR filter bank output in real time without downsampling for one template requires the floating point operation per unit time of

$$\mathrm{C}_{\mathrm{IIR}}^{*} = 12S \cdot N_{\mathrm{IIR}}, \tag{5.109}$$

and the delay

$$T^{\mathrm{IIR}}_{\mathrm{delay}} = dt. \tag{5.110}$$

Here asterisk is used to indicate the computational cost of the IIR filter method without the downsampling technique.

Fig. (5.6) shows the computational cost of one template for the FFT method as a function of T_{latency} when searching for a GW from a (1.4+1.4) $M_\odot$ NS-NS binary and its comparison to that of the IIR filter method with and without downsampling technique. It shows that the computational cost of the FFT based method increases as latencies decreases, the increase is particularly significant at latencies less than hundreds to thousands of seconds (Eq (5.106)), whereas IIR methods (Eq. (5.44), Eq. (5.109)) have an inherent latency of the sampling interval (i.e **not** a function of latency). It is clear that the IIR filter method presented in this paper has significant advantage over the FFT method in computational efficiency when low latencies are in demand. In particular, for Advanced LIGO, the IIR method can be much more efficient at latencies less than a few $\times 10^2$ seconds. For the Einstein Telescope, IIR filter method can be much more efficient at latencies less than a few $\times 10^3$ seconds.

It should be mentioned that we compare only the core computational cost for the IIR and the FFT method for one template. We purposely leave out the cost of whitening or the cost to take care of other FFT effect such as windowing effect as they are very much implementation-dependent. We also do not include template interpolation method for both methods as they are very much implementation-dependent. In practice, both methods require that the raw data be conditioned, transported, pre-whitened before they are ready to be analyzed. These are expected to cause additional latencies on the order of tens of seconds.

5.6 Conclusion

In this paper, we show that a time-domain search algorithm, with the flexibility of being able to detect a (non-precessing) compact-binary coalescence even before the final merger, is not only feasible for advanced and even future ground-based gravitational-wave detectors — but in fact can be realizable by a small number of state-of-the-art personal computers.

In addition to employing the multi-rate technique for time-domain filtering, we have developed two additional key techniques in order to bring down the computational cost into the realm of feasibility: (i) the conversion of a chirp signal into a chain of IIR filters, and (ii) an algorithm that allows the reconstruction of filtering results of a finely spaced template bank from a much coarser bank, when each template in the coarse bank is divided into sub-templates. In order to illustrate the main techniques, we have restricted ourselves to the Newtonian Chirp, but it is rather straightforward to generalize our algorithms into post-Newtonian templates.

Our main results on computational cost of the time-domain algorithm, for initial, advanced and future detectors, are summarized in Table 5.4. With a simple comparison, we also conclude that our time-domain algorithm should require less computational resources than the conventional frequency-domain approach, when a short latency of less than hundreds to thousands of seconds is required — as shown in Fig. 5.6.

Besides being computationally efficient at low (or even negative) latencies, the IIR filter bank method is also much simpler to implement than the FFT-based methods, making it ideal for parallel computing, e.g., with Graphics Processing Units Chung et al. (2010b).

Two further ingredients must be added into the search pipeline before we can set up an early-warning system for EM follow-ups of compact binary coalescence: (1) a reliable veto strategy, and (2) an efficient algorithm for sky localization. The fact that our numerical results for IIR filter groups agree so well with frequency-domain analytical estimates (Sec. 5.4.3) assuming sharp divisions in frequency indicates that the sub-IIR-groups can be well-approximated as independent contributions to the SNR. This means a χ^2-like test that compares relative SNR contributions from filter subgroups to their expectations would be a promising veto strategy (see also Cannon et al. (2011b) for other strategies that might be applicable for further efficiency improvement.)

As for localization, we could in principle adopt the existing algorithm already in place in the LIGO/VIRGO pipeline, which is based on coincidences of SNRs among multiple detectors. Alternatively, the fact that IIR filters are separated in both time and frequency may provide a possibility of developing a *coherent* search pipeline with feasible computational cost. The reason for the high number of templates in a coherent search is directly due to the multiplication of the high number of templates along the direction of mass parameters and the high number of sky locations. However, as we divide each template into frequency segments, we find that in low frequencies, although there is a large number of cycles, and hence a requirement for a finer separation in mass parameters, the sky resolution of a detector network is low and there does not need a high number of sky patches; in high frequencies, we need a fine grid in the sky, but a coarse grid in mass parameters. As a consequence, we may need a much lower number of sub-templates are required for each frequency segment. This is currently being investigated.

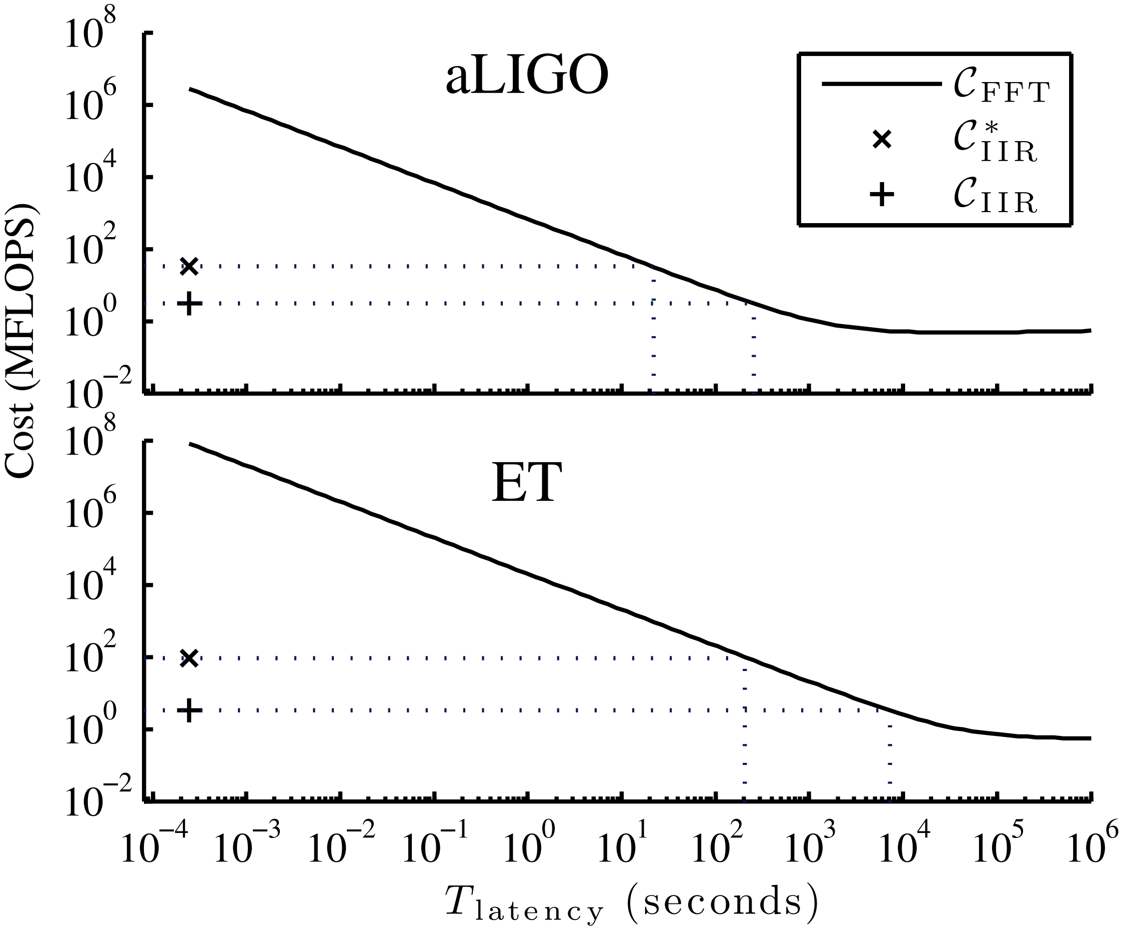

Figure 5.6 Computational cost as a function of $T_{\rm latency}$ for a straightforward FFT analysis with overlapping data segments (solid line) and for the IIR filter method with downsampling technique ("+" symbols) and without ("×" symbols) for real-time filtering with one template of a (1.4+1.4) $M_\odot$ binary. The upper panel shows the cost for aLIGO and the lower one for ET. The dotted lines illustrate the equal cost between the FFT and IIR method and the corresponding latencies. The computational cost of the FFT method is calculated from Eq. (5.106) with the longest template taken to be that of (1+1) $M_\odot$ binary and sampling rate S=4096Hz. The IIR data are from Table 5.2 (column 15) (with downsampling) and Eq. (5.109) (without downsampling).

Bibliography

Abbott, B. P., Abbott, R., Adhikari, R., et al. 2009, Reports on Progress in Physics, 72, 076901

Allan, R. R. 1969, AJ , 74, 497

Allen, B., Anderson, W. G., Brady, P. R., Brown, D. A., & Creighton, J. D. E. 2005, ArXiv General Relativity and Quantum Cosmology e-prints, arXiv:gr-qc/0509116

Althaus, L. G., Miller Bertolami, M. M., & Córsico, A. H. 2013, A&A , 557, A19

Batchelor, G. K., & O'Brien, R. W. 1977, Proceedings of the Royal Society of London. Series A, Mathematical and Physical Sciences, 355, 313

Bionta, R. M., Blewitt, G., Bratton, C. B., Casper, D., & Ciocio, A. 1987, Physical Review Letters, 58, 1494

Borderies, N., & Goldreich, P. 1984, Celestial Mechanics, 32, 127

Borderies, N., Goldreich, P., & Tremaine, S. 1984, in Planetary Rings, ed. A. Brahic, 327–329

Bottke, Jr., W. F., Vokrouhlický, D., Rubincam, D. P., & Nesvorný, D. 2006, Annual Review of Earth and Planetary Sciences, 34, 157

Buskulic, D., Virgo Collaboration, & LIGO Scientific Collaboration. 2010, Classical and Quantum Gravity, 27, 194013

Cannon, K., Chapman, A., Hanna, C., et al. 2010, PRD , 82, 044025

Cannon, K., Hanna, C., & Keppel, D. 2011a, ArXiv e-prints, arXiv:arXiv:1101.4939

Cannon, K., Hanna, C., Keppel, D., & Searle, A. C. 2011b, PRD , 83, 084053

Cannon, K., Cariou, R., Chapman, A., et al. 2011c, ArXiv e-prints, arXiv:arXiv:1107.2665

Chambers, J. E. 1999, MNRAS , 304, 793

Chandrasekhar, S. 1933, MNRAS , 93, 449

Chung, S. K., Wen, L., Blair, D., & Cannon, K. 2010a, in American Institute of Physics Conference Series, Vol. 1246, American Institute of Physics Conference Series, 207–210

Chung, S. K., Wen, L., Blair, D., Cannon, K., & Datta, A. 2010b, Classical and Quantum Gravity, 27, 135009

Colombo, G. 1966, AJ , 71, 891

Cordes, J. M., & Lazio, T. J. W. 2002, ArXiv Astrophysics e-prints, astro-ph/0207156

Croce, R. P., Demma, T., Pierro, V., et al. 2000a, PRD , 62, 121101

Croce, R. P., Demma, T., Pierro, V., Pinto, I. M., & Postiglione, F. 2000b, PRD , 62, 124020

Cutler, C., & Flanagan, É. E. 1994, PRD , 49, 2658

Delbo', M., & Tanga, P. 2009, Planet. Space Sci., 57, 259

Demircan, O., & Kahraman, G. 1991, Ap&SS, 181, 313

Dougherty, M. K., Esposito, L. W., & Krimigis, S. M. 2009, Saturn from Cassini-Huygens (Springer), doi:10.1007/978-1-4020-9217-6

Falcke, H., & Rezzolla, L. 2013, ArXiv e-prints, arXiv:1307.1409

Field, S. E., Galley, C. R., Herrmann, F., et al. 2011, Physical Review Letters, 106, 221102

Finn, L. S. 1992, PRD , 46, 5236

Ford, E. B., Kozinsky, B., & Rasio, F. A. 2000, ApJ , 535, 385

Fox, D. B., Frail, D. A., Price, P. A., et al. 2005, Nature , 437, 845

Frank, J., King, A., & Raine, D. 1992, Accretion power in astrophysics. (Cambridge University Press)

Gavrilov, S. V., & Zharkov, V. N. 1977, Icarus, 32, 443

Goldreich, P. 1965, MNRAS , 130, 159

Goldreich, P., & Sari, R. 2009, ApJ , 691, 54

Goldreich, P., & Schlichting, H. E. 2014, AJ , 147, 32

Goldreich, P., & Soter, S. 1966, Icarus, 5, 375

Goldreich, P. M., & Mitchell, J. L. 2010, Icarus, 209, 631

Greenberg, R., Barnes, R., & Jackson, B. 2008, in Bulletin of the American Astronomical Society, Vol. 40, AAS/Division for Planetary Sciences Meeting Abstracts #40, 391

Gulkis, S., Allen, M., von Allmen, P., et al. 2015, Science, 347, aaa0709

Gunn, J. E., & Ostriker, J. P. 1969, Physical Review Letters, 22, 728

Heiken, G. H., Vaniman, D. T., & French, B. M. 1991, Lunar sourcebook - A user's guide to the moon (Cambridge University Press)

Henrard, J. 1982, Celestial Mechanics, 27, 3

Hertz, H. 1882, J. reine und angewandte Mathematik, 92, 156, for English translation see *Miscellaneous Papers* by Hertz, H., Jones, Eds. and Schott, London: Macmillan, 1896.

Hobbs, P. V. 1974, Ice physics (Oxford University Press)

Hooper, S., Chung, S. K., Luan, J., et al. 2011, ArXiv e-prints, arXiv:arXiv:1108.3186

Hooper, S., Wen, L., Blair, D., et al. 2010, in American Institute of Physics Conference Series, Vol. 1246, American Institute of Physics Conference Series, 211–214

Howett, C. J. A., Spencer, J. R., Pearl, J., & Segura, M. 2010, Icarus, 206, 573

Huetter, E. S., Koemle, N. I., Kargl, G., & Kaufmann, E. 2008, Journal of Geophysical Research (Planets), 113, 12004

Iess, L., Stevenson, D. J., Parisi, M., et al. 2014, Science, 344, 78

Johnson, K. L. 1987, Contact Mechanics (Cambridge University Press)

Johnson, S. G., & Frigo, M. 2007, IEEE Transactions on Signal Processing, 55, 111

Kanner, J., Huard, T. L., Márka, S., et al. 2008, Classical and Quantum Gravity, 25, 184034

Keihm, S. J., Peters, K., Langseth, M. G., & Chute, J. L. 1973, Earth and Planetary Science Letters, 19, 337

Kovalev, Y. Y., Kellermann, K. I., Lister, M. L., et al. 2005, AJ , 130, 2473

Lainey, V., Arlot, J.-E., Karatekin, Ö., & van Hoolst, T. 2009, Nature , 459, 957

Lainey, V., Karatekin, Ö., Desmars, J., et al. 2012, ApJ , 752, 14

Langseth, M. G., Keihm, S. J., & Peters, K. 1976, in Lunar and Planetary Science Conference Proceedings, Vol. 7, Lunar and Planetary Science Conference Proceedings, ed. D. C. Kinsler, 3143–3171

LIGO Scientific Collaboration. 2009, *Advanced LIGO anticipated sensitivity curves*, LIGO Document T-0900288-v2

Lin, D. N. C., & Papaloizou, J. 1979, MNRAS , 188, 191

Linsky, J. L. 1966, Icarus, 5, 606

Loeb, A., Shvartzvald, Y., & Maoz, D. 2014, MNRAS , arXiv:1310.2419

Lorimer, D. R., Bailes, M., McLaughlin, M. A., Narkevic, D. J., & Crawford, F. 2007, Science, 318, 777

Lorimer, D. R., Karastergiou, A., McLaughlin, M. A., & Johnston, S. 2013, MNRAS , arXiv:1307.1200

Lovell, B. 1963, Nature , 198, 228

Lundy, T., & van Busbirk, J. 2007, Computing, 80, 23

Lyubarsky, Y. 2014, ArXiv e-prints, arXiv:1401.6674

Macquart, J.-P., & Koay, J. Y. 2013, ApJ , 776, 125

Malhotra, R., & Dermott, S. F. 1990, Icarus, 85, 444

Manchester, R. N., Hobbs, G. B., Teoh, A., & Hobbs, M. 2005, AJ , 129, 1993

McLaughlin, M. A., Lyne, A. G., Lorimer, D. R., et al. 2006, Nature , 439, 817

Meyer, J., & Wisdom, J. 2007, Icarus, 188, 535

—. 2008, Icarus, 193, 213

Mitra, S., Dhurandhar, S. V., & Finn, L. S. 2005, PRD , 72, 102001

Muncey, R. W. 1963, Australian Journal of Physics, 16, 24

Murray, C. D., & Dermott, S. F. 1999, Solar system dynamics (Cambridge University Press)

Nakar, E. 2007, Phys. Rep. , 442, 166

Ogilvie, G. I. 2014, ARAA , 52, 171

Ojakangas, G. W., & Stevenson, D. J. 1986, Icarus, 66, 341

Oppenheim, A. V., & Schafer, R. W. 1975, Digital signal processing, ed. Oppenheim, A. V. & Schafer, R. W.

O'Shaughnessy, R., Kalogera, V., & Belczynski, K. 2010, ApJ , 716, 615

Osten, R. A., & Bastian, T. S. 2006, ApJ , 637, 1016

—. 2008, ApJ , 674, 1078

Owen, B. J., & Sathyaprakash, B. S. 1999, Phys. Rev. D, 60, 022002

Papike, J. J., Simon, S. B., & Laul, J. C. 1982, Reviews of Geophysics and Space Physics, 20, 761

Peale, S. J. 1978, Icarus, 36, 240

—. 1999, ARA& A, 37, 533

Phinney, E. S. 1992, Royal Society of London Philosophical Transactions Series A, 341, 39

Piro, A. L. 2011, ApJL , 740, L53

Rabiner, L. R., & Gold, B. 1975, Theory and application of digital signal processing (Englewood Cliffs, N.J., Prentice-Hall, Inc., 1975)

Rafikov, R. R. 2014, ArXiv e-prints, arXiv:1403.5292

Ransom, S. M., Stairs, I. H., Archibald, A. M., et al. 2014, Nature , 505, 520

Rickett, B. J. 1990, ARAA , 28, 561

Roy, A. E., & Ovenden, M. W. 1954, MNRAS , 114, 232

Sallmen, S., Backer, D. C., Hankins, T. H., Moffett, D., & Lundgren, S. 1999, ApJ , 517, 460

Sathyaprakash, B. S., & Dhurandhar, S. V. 1991, PRD , 44, 3819

Schulson, E. M. 2001, Engineering Fracture Mechanics, 68, 1839

Seidelmann, P. K. 1992, Explanatory Supplement to the Astronomical Almanac (University Science Books)

Sinclair, A. T. 1972, MNRAS , 160, 169

Spencer, J. R., Howett, C. J., Verbiscer, A. J., et al. 2013, in AAS/Division for Planetary Sciences Meeting Abstracts, Vol. 45, AAS/Division for Planetary Sciences Meeting Abstracts, 403.03

Spitzer, L. 1978, Physical processes in the interstellar medium (John Wiley & Sons, 2008)

Spohn, T., Knollenberg, J., Ball, A. J., et al. 2015, Science, 349, 020464

Subrahmanyan, R., & Cowsik, R. 2013, ApJ , 776, 42

Tajeddine, R., Rambaux, N., Lainey, V., et al. 2014, Science, 346, 322

Tauris, T. M., Langer, N., & Kramer, M. 2012, MNRAS , 425, 1601

The ET Science Team. 2011, *Einstein gravitational wave Telescope conceptual design study*, ET-0106B-10

Thornton, D., Stappers, B., Bailes, M., et al. 2013, Science, 341, 53

Tittemore, W. C., & Wisdom, J. 1990, Icarus, 85, 394

Trott, C. M., Tingay, S. J., & Wayth, R. B. 2013, ApJL , 776, L16

Vasavada, A. R., Bandfield, J. L., Greenhagen, B. T., et al. 2012, Journal of Geophysical Research (Planets), 117, 0

Veeder, G. J., Davies, A. G., Matson, D. L., et al. 2012, Icarus, 219, 701

Ward, W. R. 1975, AJ , 80, 64

Waszczak, A., Chang, C.-K., Ofek, E. O., et al. 2015, ArXiv e-prints, arXiv:1504.04041

Watson, K. 1964, PhD thesis, California Institute of Technology, Pasadena

White, M.-A. 2012, Physical Properties of Materials, 2nd edn. (CRC Press)

Wu, Y. 2005, ApJ , 635, 688

Wu, Y., & Goldreich, P. 2002, ApJ , 564, 1024

Yoder, C. F. 1979, Celestial Mechanics, 19, 3